

REVIEW

View Article Online
View Journal | View IssueCite this: *J. Mater. Chem. A*, 2019, 7, 24059

Coordination polymer-based conductive materials: ionic conductivity vs. electronic conductivity

Hai-Ning Wang,^{ID} ^{ab} Xing Meng,^a Long-Zhang Dong,^{ID} ^b Yifa Chen,^{*b} Shun-Li Li^b and Ya-Qian Lan^{ID} ^{*b}

Coordination polymers (CPs) are emerging crystalline materials, and researchers have promoted their potential applications in various fields owing to their easily designed and tailorable structures, guest-accessible cavities and functional tunability. In this review, we mainly focused on describing the recent achievements of CPs/CP-based composites for ionic/electrical conductivity and provided their future perspectives. The designable and tailorable structures of CPs provide great opportunities to systemically tune their ionic/electrical conductivities, and various strategies have been employed to improve their conductivity. Meanwhile, the relationship between their structure and conductivity may offer some guidance for the design and synthesis of new conductive materials with high conductivity. We proposed major fundamental issues to be addressed in material design and application perspectives. By elaborating the advantages and challenges of CPs in ionic/electrical conductivity, some useful advice is provided in this review to shed some light on their development.

Received 30th July 2019

Accepted 7th September 2019

DOI: 10.1039/c9ta08253k

rsc.li/materials-a

1. Introduction

Coordination polymers (CPs) are a family of crystalline materials and have become one of the hot research fields currently.^{1,2} In general, CPs are constructed from metal ions or metal clusters and organic linkers, and their structures and

dimensionalities depend on the coordination geometries and capabilities of the two building units.³ In the past twenty years, a large number of achievements have been reported, which mainly focus on the synthesis and structural characterization of CPs. The inherent features (*e.g.*, porosity, rich compositions and structure tunability, *etc.*) of CPs can be modified by the rational selection of building units through assembly or post-synthetic methods. In recent years, an increasing number of CPs have been synthesized as nanocrystals and further prepared into composites by combining with other materials.^{4–9} Their versatility, tunability and rich crystalline structures bring diverse and tunable characteristics and provide considerable platforms for

^aSchool of Chemistry and Chemical Engineering, Shandong University of Technology, Zibo, Shandong, 255049, P. R. China

^bJiangsu Collaborative Innovation Centre of Biomedical Functional Materials, Jiangsu Key Laboratory of New Power Batteries, College of Chemistry and Materials Science, Nanjing Normal University, Nanjing 210023, P. R. China. E-mail: yqlan@njnu.edu.cn



Hai-Ning Wang received his BSc degree in Chemistry from Northeast Normal University in 2009, and in the same year, he joined Professor Zhong-Min Su to pursue his Ph.D. in Physical Chemistry at Northeast Normal University. Currently he is a Lecturer at Shandong University of Technology, and he is undertaking postdoctoral studies with Prof. Ya-Qian Lan in Inorganic Chemistry. His

research interests focus on crystalline porous materials.



Xing Meng received her BSc degree in Material Chemistry from Langfang Teachers University in 2009 and MSc in Physical Chemistry in 2012 from Northeast Normal University. Also in the same year, she joined Professor Hongjie Zhang to pursue her Ph.D. in Inorganic Chemistry at Changchun Institute of Applied Chemistry, Chinese Academy of Sciences (CAS). Currently she is

a Lecturer at Shandong University of Technology. Her research interests focus on multi-functional porous materials and relevant properties.

various properties. To date, most studies have focused on studying catalysis, energy storage, sensors, *etc.*^{10–12} In general, the vast majority of CPs are insulators and exhibit very low electronic/ionic conductivity, which is attributed to the fact that CPs are usually constructed from hard metal ions and O- or N-donor redox-inactive ligands and cannot provide efficient routes for charge transport.

To overcome this, various design principles such as post-modifying metal and organic components and loading guest molecules into pores have been developed to effectively improve their conductivity.¹³ Dramatic developments have been achieved in recent years, and extensive research on CP-based conductive materials has been reported with the help of these strategies; these materials have been successfully explored as the electrode materials for fuel cells and even electrochemical devices.¹⁴ As a new type of electrode materials for electrochemical energy storage and conversion, the superior electrochemical properties of CPs have been demonstrated and new mechanisms have been proposed using these materials, making

the design of new conductive materials and the study of their mechanisms easier. The advantages of CPs used for electrochemical energy storage and conversion are as follows: (i) the available spaces inside frameworks can hold conductive guest molecules, promoting the generation of transport pathways. (ii) The environment of ordered pores/channels can be modified to allow ions/electrons to transfer more smoothly, and transport pathways are easier to be predicted within well-defined spaces. Besides, active sites can be located on introduced guest molecules and/or functional groups on the walls between void spaces, establishing strong interactions between the host structure and guest molecules. (iii) The electrical conductivity properties can be tuned *via* the modification of various CP structures through changing the organic linkers or metal ions. Several reviews have summarized the recent progress on pristine/modified CP-based conductive materials carefully in this field,^{13,15–23} and two popular strategies for improving the conductivity have been summarized according to the structural advantages of CPs: (i) loading of guest molecules (*e.g.*, NH_4^+ ,



Long-Zhang Dong received his BSc degree in Chemistry from Nanjing Normal University in 2017, and in the same year, he joined Professor Ya-Qian Lan to pursue his MSc in Inorganic Chemistry from Nanjing Normal University. His research interests focus on crystalline porous materials and electron chemistry based on these materials.



Prof. Shun-Li Li was born in 1979 in Jilin, P. R. China. She received her BS (2002) and PhD degree (2008) from Northeast Normal University under the supervision of Prof. Jian-Fang Ma. She carried out post-doctoral studies with Prof. Zhong-Min Su in Environmental Chemistry at Northeast Normal University. Then she worked as a Japan Society for the Promotion of Science invited fellow at the National Institute of Advanced Industrial Science and Technology in 2012. She is a Professor of Chemistry at Nanjing Normal University. Her current research interest lies in the syntheses, structures and properties of organic–inorganic hybrid materials.



Yifa Chen was born in 1989 in Fujian, P. R. China. He received his B.S. degree and obtained his Ph.D. degree from the School of Chemistry and Chemical Engineering, Beijing Institute of Technology under the supervision of Prof. Bo Wang. In 2018, he joined Prof. Ya-Qian Lan's group as an Associate Professor at the College of Chemistry and Materials Science of Nanjing Normal University. His research

interests focus on the fabrication of metal–organic framework (MOF) based devices such as membranes, foams and fibers that can be applicable in energy storage and conversion, proton conductivity or photo/electric heterogeneous catalysis.

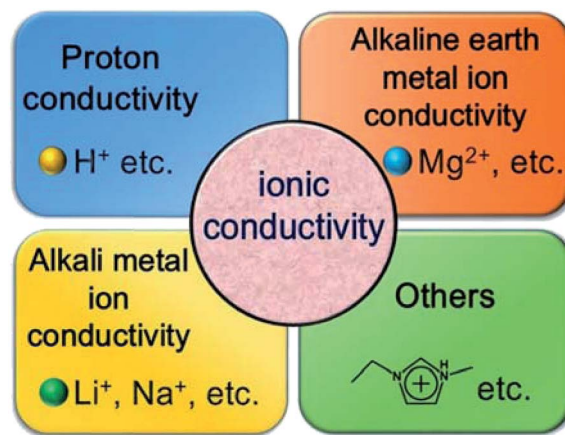


Prof. Ya-Qian Lan was born in 1978 in Jilin, P. R. China. He received his BS and PhD degree (2009) from the Faculty of Chemistry, Northeast Normal University, under the supervision of Prof. Zhong-Min Su. In 2010, he worked as a JSPS postdoctoral fellow at AIST. Since the fall of 2012, he has been a Professor of Chemistry at Nanjing Normal University. His current research interests focus on the synthesis of porous crystalline materials and catalytic research related to clean energy applications.

H₂SO₄, and polypyrrole) into their framework and (ii) post-modification of the metal or organic components/introduction of functional groups (*e.g.*, –COOH and –SO₃H) into ligands (Scheme 1). In this perspective, we mainly focus on discussing the significant achievements on the ionic and electrical conductivities of pristine/modified CPs and their composites in the past years. At the end of this review, we will provide some useful perspectives/suggestions for the development of CP-based conductive materials.

2. CPs as solid-state ionic conductors

This section summarizes the progress of CPs and their composites used for ionic conductivity. CPs often display porosity, and exhibit various structural features, such as available voids and tailorable structures. Compared with traditional nanoporous materials, the significant characteristics of CPs make them ideal candidates as ionic conductors. Besides, their well-defined structures may be beneficial for outlining the ion transport pathway clearly, and are helpful to discover new ion conduction mechanisms. Thus, we believe that CPs may become an important class of ion conductive materials. To date, various CP-based ionic conductors have been established, and four subspecies have been proposed by us according to the type of mobile ions trapped in their skeleton: (i) proton conductivity (H⁺, *etc.*), (ii) alkali metal ion conductivity (Li⁺, Na⁺, *etc.*), (iii) alkaline earth metal ion conductivity (Mg²⁺, *etc.*), and (iv) other



Scheme 2 Various types of ionic conductivities.

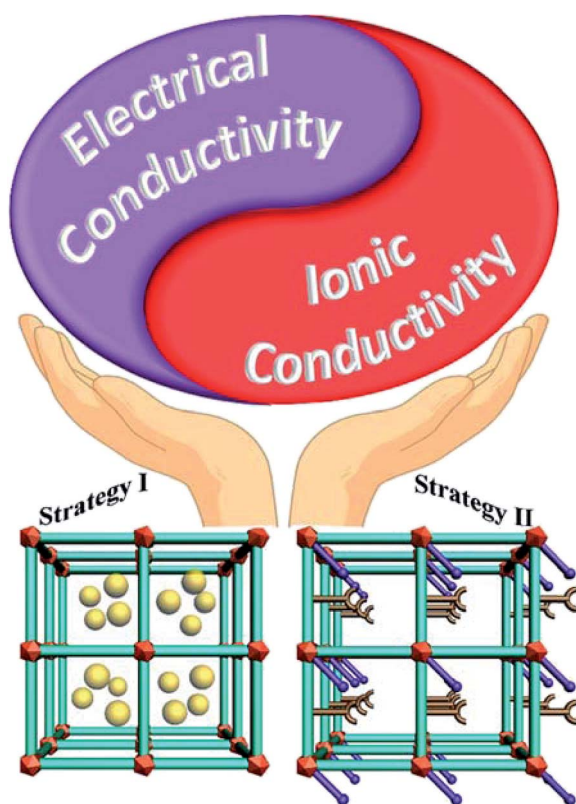
types of ion conductivity (IL, *etc.*) (Scheme 2). Next, each subspecies will be discussed.

2.1 Proton conductivity

Developments in synthetic chemistry and new progress in synthetic approaches provide more opportunities for the construction of CPs as proton conductors. According to the literature, proton conduction can be divided into two broad categories, humidity-dependent conditions and anhydrous conditions. To date, the improvement of proton conduction mainly relies on two strategies. One is the introduction of acidic functional groups (*e.g.*, –COOH and –SO₃H) into the backbone of CPs, and the other is the integration of proton carriers (*e.g.*, imidazole) into their pores. In the following section, we mainly describe the development of CPs and their composites as proton conductors in the past three years (Table 1).^{24–105}

2.1.1 Water-mediated proton conductivity. The designable and porous structures of CPs make them excellent platforms for proton conduction. Their self-assembled and tailorable porous structures allow various functional groups/proton carriers to be integrated in their internal frameworks, generating proton-conducting systems. Different approaches including tuning framework structure, guest molecules and functional groups have been applied to adjust the proton-conducting properties of CPs, and new progress has been achieved.

2.1.1.1 Framework structure. In 2018, Das's group proposed a simple template strategy to prepare proton-conducting CPs, where the templates facilitate the formation of ordered H-



Scheme 1 Two popular strategies for improving conductivity.

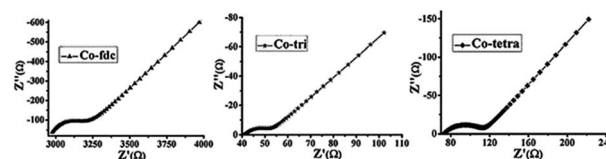


Fig. 1 Nyquist plots of Co-fdc, Co-tri, and Co-tetra at 80 °C and 98% RH. (Reprinted with permission from ref. 24, Copyright 2018, Wiley-VCH.)

Table 1 List of selected proton-conductive materials in this review

Name in the ref.	Guest molecule	Condition	Conductivity/S cm ⁻¹	Ref.
{[Co(bpy)(H ₂ O) ₄](btec) _{0.5} ·H ₂ O} _n	Btec and H ₂ O	80 °C and 98% RH	4.85 × 10 ⁻³	24
MIT-25	H ₂ O	75 °C and 40% RH	1.03 × 10 ⁻⁴	25
[La(H ₅ L)(H ₂ O) _n](H ₂ O)	H ₂ O	85 °C and 95% RH	6.0 × 10 ⁻³	26
[N ₂ H ₅][CeEu(C ₂ O ₄) ₄ (N ₂ H ₅)]·4H ₂ O	H ₂ O	25 °C and 100% RH	3.42 × 10 ⁻³	27
[Cu ₂ (Htzehp) ₂ (4,4'-bipy)]·3H ₂ O	H ₂ O	80 °C and 95% RH	1.43 × 10 ⁻³	28
TMOF-2	H ₂ O	90 °C and 98% RH	1.23 × 10 ⁻⁴	29
Na ₂ [Eu(SDB) ₂ (COO)]·0.375DMF·0.4H ₂ O	DMF and H ₂ O	90 °C and 90% RH	2.91 × 10 ⁻²	30
KAUST-7'	H ₂ O	90 °C and 95% RH	2.0 × 10 ⁻²	31
FJU-16	H ₂ O	−40 to 80 °C	1.25 × 10 ⁻³	32
FJU-17	H ₂ O	−40 to 100 °C	1.08 × 10 ⁻²	32
MOF-512	H ₂ O	25 °C and 99% RH	2.9 × 10 ⁻³	34
Im-Fe-MOF	H ₂ O	60 °C and 98% RH	1.21 × 10 ⁻²	36
Im@NENU-3	H ₂ O and Im	70 °C and 90% RH	1.82 × 10 ⁻²	37
Im@MOF-808	H ₂ O	65 °C and 99% RH	3.45 × 10 ⁻²	38
DNA@ZIF-8	H ₂ O and DNA	75 °C and 97% RH	0.17	39
Cu ^I -MOF·tz	H ₂ O and tz	80 °C and 95% RH	2.89 × 10 ⁻³	40
Cu ^I -MOF·pz·6HCl	HCl	80 °C and anhydrous	2.17 × 10 ⁻²	41
Cu ^I -MOF·pz·3H ₂ SO ₄	H ₂ SO ₄ and H ₂ O	75 °C and 95% RH	3 × 10 ⁻³	41
PCMOF-17	Dimethylammonium cations and H ₂ O	25 °C and 40% RH	1.25 × 10 ⁻³	42
{[Co ₃ (p-ClPhHIDC) ₃ (H ₂ O) ₃]·6H ₂ O} _n	NH ₃ ·H ₂ O and H ₂ O	100 °C and NH ₃ ·H ₂ O concentration of 7.4 M	4.25 × 10 ⁻²	44
[Cu(p-IPhHIDC)] _n	H ₂ O	100 °C and 98% RH	1.51 × 10 ⁻³	45
{[Na[Cd(MIDC)]] _n	H ₂ O	100 °C and 98% RH	1.04 × 10 ⁻³	46
H₂SO₄@MIL-101-SO₃H	H ₂ SO ₄ and H ₂ O	70 °C and 90% RH	1.82	47
		−40 °C	0.92 × 10 ⁻²	
TETA@3	TETA, H ₃ PW ₁₂ O ₄₀ and H ₂ O	80 °C and 100% RH	1.52 × 10 ⁻²	48
PCMOF2_{1/2}(Tz)	Tz and H ₂ O	85 °C and 90% RH	1.17 × 10 ⁻¹	49
Nd ₂ (C ₈ O ₄ H ₄) ₃ (C ₅ NOH ₅) ₂ ·(DMF) _x @EG	EG and H ₂ O	90 °C and 90% RH	1.72 × 10 ⁻³	50
HIm11 ⊂ VNU-17	Im and H ₂ O	70 °C and 85% RH	5.93 × 10 ⁻³	51
histamine@VNU-23	Histamine and H ₂ O	95 °C and 85% RH	1.79 × 10 ⁻²	52
Mg(Tp)(PyOH)	Cs ⁺ and H ₂ O	90 °C and 90% RH	1.61 × 10 ⁻²	53
BUT-8(Cr)A	H ₂ SO ₄ and H ₂ O	100% RH and 80 °C	1.27 × 10 ⁻¹	54
[Co(DCDPP)]·5H ₂ O	H ₂ O	80 °C and 97% RH	3.9 × 10 ⁻²	55
[Ni ₈ (OH) ₄ (H ₂ O) ₂ (BDPCOOH) ₆]	H ₂ O	80 °C and 97% RH	2.22 × 10 ⁻³	56
UiO-66(Zr)-(CO ₂ H) ₂	H ₂ O	90 °C and 95% RH	2.3 × 10 ⁻³	57
SA-EIMS@MIL-101	Anhydrous	150 °C	1.89 × 10 ⁻³	58
1,2,3-Triazole@Cu₂(F₂AzoBDC)₂(dabco)	Anhydrous	—	1.2 × 10 ⁻⁶	59
CS/H₂SO₄@MIL-101-8	H ₂ SO ₄ and H ₂ O	100% RH	0.095	60
PIL@MIL	Poly <i>N</i> -vinylimidazolium and H ₂ O	20 °C and ion concentration of 0.633 mmol cm ³	0.0366	61
ImPEEK/ImMIL-101(Cr)	OH ⁻ and H ₂ O	60 °C and 100% RH	0.047	62
Naf-1SZM	H ₂ O	80 °C and 35% RH	0.00296	63
UiO-66-NH₂ + UiO-66-SO₃H/Nafion-0.6	H ₂ O	90 °C and 95% RH	0.256	64
GO@UiO-66-NH₂/Nafion-0.6	H ₂ O	90 °C and 95% RH	0.303/3.403 × 10 ⁻³	65
		and anhydrous		
SPEEK/S-UiO-66@GO-10	H ₂ O	70 °C, 95% RH and 100 °C, 40% RH	0.268/0.01657	66
SPEEK/ZCN-2.5	H ₂ O	120 °C and 30% RH	0.05024	67
Nafion with 2% loading of UiO-66 crystals (200 nm average size)	H ₂ O	110 °C and 95% RH	0.207	68
MOF-801	H ₂ O	25 °C and 98% RH	1.88 × 10 ⁻³	69
MOF-801@PP-60	H ₂ O	52 °C and 98% RH	1.84 × 10 ⁻³	69
JUC-200@PVA-10	H ₂ O	50 °C in pure water	1.25 × 10 ⁻³	70
H[Ln(H ₂ O) ₄] ₂ [MnV ₁₃ O ₃₈]·9NMP·17H ₂ O (Ln = Ce and La)	H ₂ O	61 °C and 97%	4.68/3.46 × 10 ⁻³	74
H ₁₄ [Na ₆ (H ₂ O) ₁₂] ₄ [K ₄₂ Ge ₈ W ₇₂ O ₂₇₂ (H ₂ O) ₆₀]·solvent	H ₂ O	85 °C and 98% RH	6.8 × 10 ⁻²	75
K ₈ Na ₃ Li ₅ {[Na(NO ₃)(H ₂ O)] ₄ [Al ₁₆ (OH) ₂₄ (H ₂ O) ₈ (P ₈ W ₄₈ O ₁₈₄)] ₃ }}·66H ₂ O	H ₂ O	85 °C and 70% RH	4.5 × 10 ⁻²	76
HImMo ₁₃₂	Him and H ₂ O	60 °C and 98% R	4.98 × 10 ⁻²	77
HCl 1	HCl	90 °C and anhydrous	1.03 × 10 ⁻²	79
(CH ₃ NH ₃) ₂ Ag ₄ Sn ₃ S ₈	HCl	Anhydrous, N ₂ atmosphere and 67 °C, 99%	1.87 × 10 ⁻⁴ /1.14 × 10 ⁻³	80

bonded networks. Employing different polycarboxylates as templates, three one-dimensional (1D) chain structures based on common $[\text{Co}(\text{bpy})(\text{H}_2\text{O})_4]^{2+}$ chains, namely **Co-fdc** with the formula $\{[\text{Co}(\text{bpy})(\text{H}_2\text{O})_4](\text{fdc}) \cdot (\text{H}_2\text{O})_{1.5}\}_n$, **Co-tri** with the formula $\{[\text{Co}(\text{bpy})(\text{H}_2\text{O})_4](\text{Hbtc}) \cdot (\text{H}_2\text{O})_{1.5}\}_n$, and **Co-tetra** with the formula $\{[\text{Co}(\text{bpy})(\text{H}_2\text{O})_4](\text{bttec})_{0.5} \cdot \text{H}_2\text{O}\}_n$ were synthesized.²⁴ With the aid of H-bonded networks between the polycarboxylate templates and crystallized water molecules, all of them exhibited good performances. The best conductivity values of **Co-fdc**, **Co-tetra** and **Co-tri** were 4.85×10^{-3} , 4.15×10^{-2} and $1.49 \times 10^{-1} \text{ S cm}^{-1}$ at 80 °C and 98% relative humidity (RH), respectively (Fig. 1). These results imply that the template strategy may be an excellent choice to prepare excellent conductors.

In the same year, Dincă's group reported another type of porous CP (**MIT-25**, $\text{Mg}_2\text{H}_6(\text{H}_3\text{O})(\text{TTFTB})_3$) and applied it in proton conduction. **MIT-25** possessing a pore size distribution of both micropores and mesopores ($\sim 4.5 \text{ \AA}$ and $\sim 27 \text{ \AA}$ width, respectively) exhibited unique proton conducting behavior.²⁵ With an increase in humidity, its small and large pores become full of water molecules in sequence, resulting in distinct proton transport behaviours. This experimental phenomenon was supported by computational studies on the electrostatic potential and pore volume as well as water uptake at low RH and thermogravimetric analysis. The humidity- and temperature-dependent conductivities of this sample were investigated. The proton conductivity of **MIT-25** changed from $1.58 \times 10^{-5} \text{ S cm}^{-1}$ (25 °C) to $1.03 \times 10^{-4} \text{ S cm}^{-1}$ (75 °C) at 40% RH, producing an E_a of 0.36 eV. Further tests at 95% RH revealed that the proton conductivity could be tuned from $6.8 \times 10^{-5} \text{ S cm}^{-1}$ (25 °C) to $5.1 \times 10^{-4} \text{ S cm}^{-1}$ (75 °C), generating an E_a of 0.40 eV. The different E_a values at 40% and 95% RH indicate the conduction mechanisms may change with an increase in humidity (Fig. 2).

Besides, seven isostructural lanthanide CPs, $[\text{Ln}(\text{H}_5\text{L})(\text{H}_2\text{O})_n](\text{H}_2\text{O})$ (**Ln-PCMOF-5**, Ln = La, Ce, Pr, Nd, Sm, Eu and Gd) have been synthesized, and the structures of this family are extremely similar.²⁶ The lanthanide contraction was employed to tune their proton conducting pathways (Fig. 3). Two members of this isostructural family, the La and Pr frameworks,

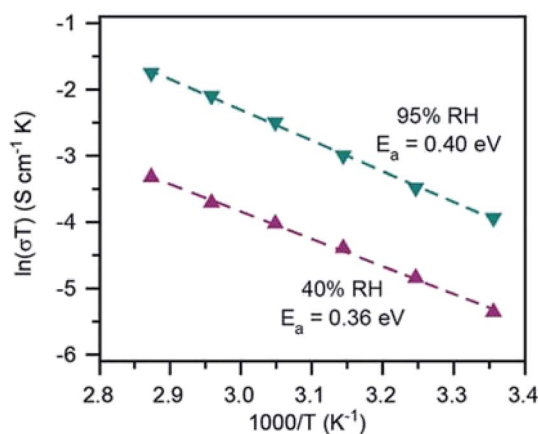


Fig. 2 Arrhenius plot of the proton conductivities of **MIT-25**. (Reprinted with permission from ref. 25, Copyright 2018, American Chemical Society.)

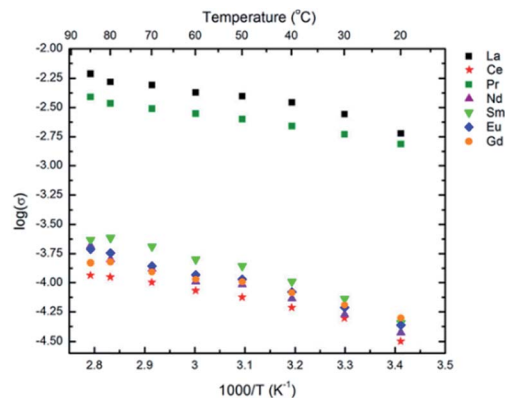


Fig. 3 Relation between conductivity and temperature for **Ln-PCMOF-5**. (Reprinted with permission from ref. 26, Copyright 2017, American Chemical Society.)

possess larger particle sizes, but showed one order of magnitude greater conductivity than the others. Thus, to exclude the effect of particle size on conductivity, conductivity tests were performed on the samples treated with ball milling for different times. The results revealed that the crystal size decreased with an increase in the milling time, which further led to lower conductivity. This experimental result exhibits that the conductivity may be related with the difference in grain boundary, not the particle size, and a low grain boundary resistance and relative ordered arrangement are preferable to maintain proton transport pathways. In the same year, a bimetallic lanthanide-oxalate compound, $(\text{N}_2\text{H}_5)[\text{CeEu}(\text{C}_2\text{O}_4)_4(\text{N}_2\text{H}_5)] \cdot 4\text{H}_2\text{O}$, was reported, which has the highest room-temperature proton conductivity ($3.42 \times 10^{-3} \text{ S cm}^{-1}$) under 100% RH among the lanthanide-based CPs.²⁷

In addition to the three-dimensional (3D) structure, materials with two-dimensional (2D) structures have also been explored. 2D CPs such as $[\text{Cu}_2(\text{Htzehp})_2(4,4'\text{-bipy})] \cdot 3\text{H}_2\text{O}$ have been reported.²⁸ It should be mentioned that single-crystal to single-crystal (SC-SC) transformation between the anhydrate and trihydrate phases takes place by changing the temperature and humidity.²⁸ Single-crystal proton conductivity tests revealed that **1·3H₂O** possesses highly anisotropic proton conductive behaviour, and the highest value along the [100] direction is $1.43 \times 10^{-3} \text{ S cm}^{-1}$, which was obtained at 80 °C and 95% RH. This result is two orders of magnitude higher than that along the [010] direction (Fig. 4), which is in accordance with the direction of the hydrogen bonded network. It is worth mentioning that the single-crystal proton conductivity could be maintained for 48 h.

Furthermore, two types of linear linkers, organosulfonate 1,4-BDMS and 4,4'-bipy, were employed to construct a highly porous 3D framework, **TMOF-2**.²⁹ It should be noted that one-fourth of the metal-ligand connectivity inside the framework disappeared, leaving unsaturated coordinated Cu^{2+} sites and free sulfonate groups, while the framework remained intact. The conductivity of **TMOF-2** increased from $8.03 \times 10^{-6} \text{ S cm}^{-1}$ at 20 °C to $1.23 \times 10^{-4} \text{ S cm}^{-1}$ at 90 °C. The authors speculated that the enhancement in the proton conductivity may be

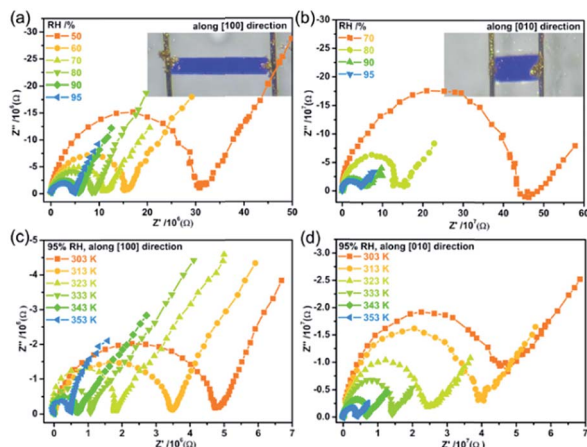


Fig. 4 Single-crystal Nyquist plots of $[\text{Cu}_2(\text{Htzehp})_2(4,4'\text{-bipy})]\cdot 3\text{H}_2\text{O}$ along the [100] and [010] directions under different RHs at 30 °C (a and b) and under different temperatures at 95% RH (c and d). (Reprinted with permission from ref. 28, copyright 2018, American Chemical Society).

ascribed to the hydrogen bonding networks formed by the free sulfonate groups, coordinated water molecules and guest water molecules. To support this hypothesis, a previously reported **TMOF-1** with a complete Cu-sulfonate connectivity was used for comparison. The conductivity of **TMOF-1** increased from $9.51 \times 10^{-8} \text{ S cm}^{-1}$ (20 °C, 98% RH) to $1.62 \times 10^{-6} \text{ S cm}^{-1}$ (90 °C, 98% RH), approximately two orders of magnitude lower than that of **TMOF-2**. The experimental results demonstrate that the absence metal–ligand connectivity may be a promising route for designing new proton-conductive materials.

The above example reveals that the combination of exposed metal ions and sulfonate groups may create an environment beneficial for proton transfer. The following work further supported this hypothesis. An anionic lanthanide-based framework, $\text{Na}_2[\text{Eu}(\text{SDB})_2(\text{COO})]\cdot 0.375\text{DMF}\cdot 0.4\text{H}_2\text{O}$, was designed and presented excellent proton conductivity ($2.91 \times 10^{-2} \text{ S cm}^{-1}$ at 90 °C and 90% RH) and an ultralow E_a of 0.10 eV.³⁰ The low E_a suggests that the proton conduction mechanism is the Grotthuss mechanism. Highly ordered Na^+ ions and oxygen atoms from the framework create an environment that is favourable for proton transport (Fig. 5). This hypothesis is demonstrated to be reasonable by the change in proton conductivity ($2.52 \times 10^{-3} \text{ S cm}^{-1}$) and E_a (0.15 eV) after Li^+ exchange.

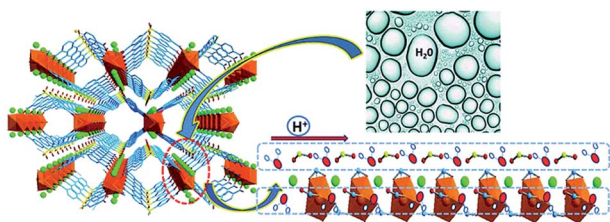


Fig. 5 Proton conductive mechanism. (Reprinted with permission from ref. 30, Copyright 2017, American Chemical Society.)

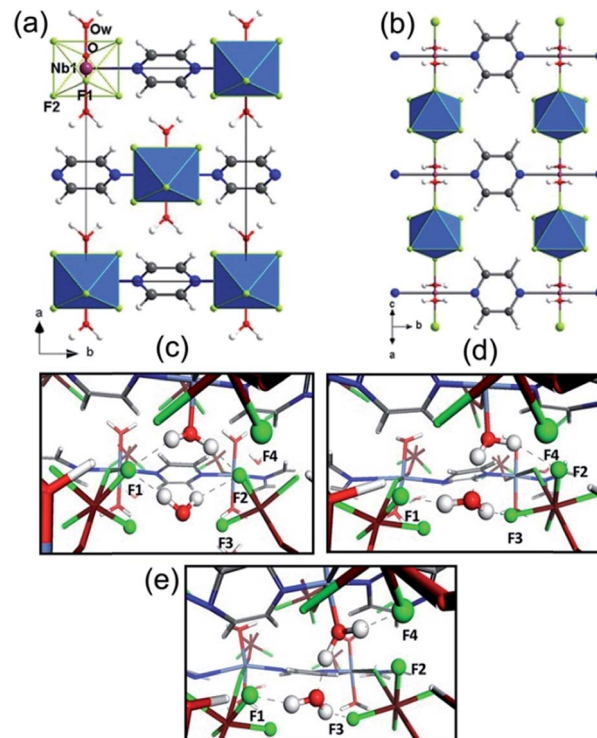


Fig. 6 Structure of **KAUST-7'** along the [001] (a) and [101] (b) directions. Immediate arrangement of the hydrogen-bond network along the [101] direction after 0.009 ps (c), 1.072 ps (d) and 1.879 ps (e) calculated by dynamics simulations (F, green; C, gray; O, red; N, blue; Ni, Nb, brown and H, white). (Reprinted with permission from ref. 31, Copyright 2018, American Chemical Society.)

Moreover, a new experimental phenomenon was observed by Mileo *et al.*³¹ After exposure to an environment similar to proton conduction, a new CP named **KAUST-7'** was generated, which was derived from **KAUST-7** (Fig. 6a and b). The derivative **KAUST-7'** showed excellent proton conductive behavior over 7 days ($2.0 \times 10^{-2} \text{ S cm}^{-1}$ at 363 K and 95% RH). To reveal the proton transport mechanism, *ab initio* molecular dynamics simulations were employed, which showed that coordinated water molecules and fluorine moieties, as well as free water molecules join together to form the H-bond network, which is favorable for proton transport (Fig. 6c–e).

Liu *et al.* reported two types of anionic CPs, $[(\text{CH}_3)_2\text{NH}_2][\text{In}(\text{L})]\cdot 2.5\text{DMF}\cdot 2\text{H}_2\text{O}$ (**FJU-16**) and $[(\text{CH}_3)_2\text{NH}_2][\text{In}(\text{L})]\cdot 4.5\text{DMF}\cdot 16\text{H}_2\text{O}$ (**FJU-17**), based on the same ligand and metal ion.³² The structures of **FJU-16** and **FJU-17** are 4-fold interpenetrated and 2-fold interpenetrated, respectively (Fig. 7). These two anionic CPs exhibited high proton conductive properties in the absence of additional humidity. Compared to **FJU-16**, the performance of **FJU-17** was better ($1.08 \times 10^{-2} \text{ S cm}^{-1}$, –40 to 100 °C vs. $1.25 \times 10^{-3} \text{ S cm}^{-1}$, –40 to 80 °C). The results show that the framework interpenetration plays an important role in the proton conduction.

The clear mechanism of proton conduction is a key factor for designing new materials with excellent conductivity. In 2016, $[\text{M}_3(\text{H}_3\text{L})_2(\text{H}_2\text{O})_9(\text{C}_2\text{H}_6\text{SO})_3]$ ($\text{M} = \text{Ni}$ and Co), denoted as **MFM-**

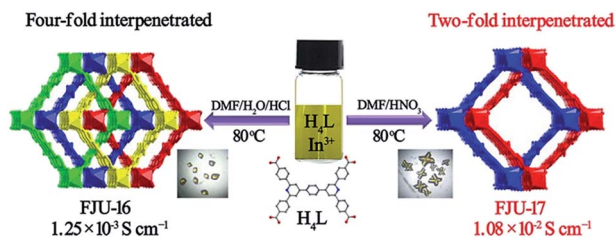


Fig. 7 Different proton conductive behaviors resulting from different framework interpenetration. (Reprinted with permission from ref. 32, Copyright 2018, American Chemical Society.)

500(Ni) and MFM-500(Co), were selected to study the mechanism.³³ Combined with single-crystal XRD, quasi-elastic neutron scattering (QENS) was employed to investigate the proton conductive mechanism of MFM-500(Ni). The data resulting from QENS under humid conditions revealed that the proton diffusion is ascribed to “free diffusion inside a sphere”. Three years later, the “free diffusion inside a sphere” mechanism further supported the proton dynamics in another work. In 2019, Schröder's group employed multi-carboxylic ligands to prepare a new barium-based MOF-512.³⁴ Due to the existence of free carboxylic groups pointing inside the channels of the framework, it exhibited a high proton conductive value of $2.9 \times 10^{-3} \text{ S cm}^{-1}$ at 99% RH and 25 °C.³⁴ QENS indicated that “free diffusion inside a sphere” is suitable for explaining the proton dynamics of MFM-512. It is worth mentioning that free carboxylic groups located inside the channels of CPs may be an effective strategy to improve their proton conductivity. Various methods such as introducing guests with protons into the framework of porous CPs have been used to improve their proton conductivity; however, there are no efficient approaches to modify the conductivity of nonporous CPs. The same group has made other attempts in this field.³⁵ They used a series of lanthanide CPs MFM-550(M) (M = La, Ce, Nd, Sm, Gd and Ho) as examples, and proposed three points: (i) employing metal ions with lower oxidation states, (ii) shortening the length of the ligand, and (iii) increasing the amount of protons located on the surface. The experimental results demonstrate that three strategies are beneficial for improving the proton conductivity of CPs.

2.1.1.2 Guest molecules. In 2017, a proton conductive model system based on Fe-MOF was established by Lan's group, and the members were Fe-MOF as the blank, imidazole@Fe-MOF (Im@Fe-MOF) with loaded free imidazole, and imidazole-Fe-MOF (Im-Fe-MOF) with coordinated imidazole.³⁶ The parent Fe-MOF, resulting from $\text{Fe}_3\text{O}(\text{CH}_3\text{CO}_2)_6$ clusters and H_3L ligands, acts as the stable platform. Loading imidazole molecules into Fe-MOF generated Im@Fe-MOF. The structure of Im-Fe-MOF is similar to that of Fe-MOF, with imidazole molecules replacing the coordinated water molecules and coordinating to the metal nodes. This model system was used to investigate the effect of imidazole on proton conduction. The proton conductivity value of Im-Fe-MOF was $1.21 \times 10^{-2} \text{ S cm}^{-1}$ at 60 °C, approximately two orders of magnitude higher than that of Im@Fe-MOF and Fe-MOF. Density functional theory (DFT) calculations suggested that the coordinated imidazole

molecules in Im-Fe-MOF play a more important role in proton transportation than the coordinated water molecules in Fe-MOF (Fig. 8a). Additionally, Im-Fe-MOF exhibited a more stable performance than Im@Fe-MOF under a water atmosphere (Fig. 8b).

In the same year, another work proposed an opposing view. The authors recognized that coordinated imidazole molecules may hinder the proton transport pathway, which may lead to a low performance. Through a one-pot method, a poly-oxometalate-based framework $[\text{Cu}_{12}(\text{BTC})_8(\text{H}_2\text{O})_{12}][\text{HPW}_{12}\text{O}_{40}]$ ·guest (NENU-3) incorporating numerous free imidazoles, namely Im@NENU-3, was designed and synthesized.³⁷ As a control, Im-Cu@NENU-3a was synthesized through a two-step approach with imidazole molecules bonded with metal nodes. Im@NENU-3 exhibited very high proton conductivity ($1.82 \times 10^{-2} \text{ S cm}^{-1}$ at 90% RH and 70 °C), which was better than that of Im-Cu@NENU-3a ($3.16 \times 10^{-4} \text{ S cm}^{-1}$). The single-crystal structure analysis revealed that in Im-Cu@NENU-3, the coordinated imidazole molecules in the framework occupy most of the spaces of the available cages (Fig. 9a and b), and then hinder the proton transport pathway, thus leading to lower conductivity (Fig. 9c and d).

Two years later, a very stable CP MOF-808 was selected by Ren's group to incorporate imidazole molecules, giving birth to Im@MOF-808.³⁸ Compared to the parent framework MOF-808, Im@MOF-808 exhibited the best performance ($3.45 \times 10^{-2} \text{ S cm}^{-1}$ at 65 °C and 99% RH) among the Im-loaded proton-conductive CPs (Fig. 10a and b), and was stable for at least 2 h under the test conditions (Fig. 10c). Moreover, Im@MOF-808 also possessed humidity-cycling proton conduction (Fig. 10d).

Besides, composite proton-conductive membranes based on biomolecule/CP have been designed and prepared.³⁹ The introduction of single-strand DNA molecules into ZIF-8 membranes generated composite DNA@ZIF-8 membranes (Fig. 11). The composite membrane exhibited excellent proton conductivities ($3.40 \times 10^{-4} \text{ S cm}^{-1}$ at 25 °C and 0.17 S cm^{-1} at 75 °C, under 97% RH). The high performance is attributed to the hydrogen-bond networks formed by the DNA molecules and the water molecules inside ZIF-8. It should be mentioned that the composite membrane possessed a low methanol

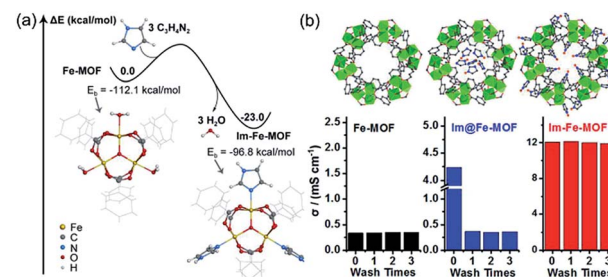


Fig. 8 (a) Reaction energy of ligand exchange (ΔE , in kcal mol⁻¹) calculated at the CPCM(water)/UB3LYP/[6-311++G(d,p)/SDD-(Fe)]//UB3LYP/[6-31G(d)/LANL2DZ(Fe)] level. (b) Proton conductivities with wash times of the samples for Fe-MOF, Im@Fe-MOF and Im-Fe-MOF at 60 °C and 98% RH. (Reprinted with permission from ref. 36, Copyright 2017, American Chemical Society.)

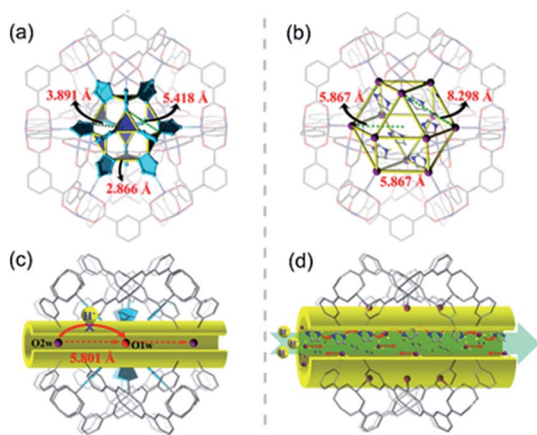


Fig. 9 (a) Cuboctahedral cage in Im-Cu@NENU-3b identical to Im-Cu@NENU-3a and (b) original NENU-3 accommodating more imidazole molecules. (c) Derived proton conductive pathway of Im-Cu@NENU-3a with the help of single crystal X-ray analysis. (d) Schematic diagram of the possible proton transport pathways in Im@NENU-3. (Reprinted with permission from ref. 37, Copyright 2017, American Chemical Society.)

permeability of $1.25 \times 10^{-8} \text{ cm}^2 \text{ s}^{-1}$ owing to its small pore entrance. Taken full advantage of this characteristic, the DNA@ZIF-8 membranes were successfully integrated into methanol fuel cells, which showed a power density of 9.87 mW cm^{-2} . This is the first example of CP-based proton conductive membrane applicable in methanol fuel cells.

Khatua and co-workers employed solvent molecules (H_2O , MeOH, DMSO, DMF and DEA) and aromatic molecules (NB, DNB, py and tz) to prepare a family of guest-exchanged CuI-MOF (1) derivatives, including $[1 \cdot (\text{DMF}) (\text{MeCN})]$, $[1 \cdot (\text{H}_2\text{O}) (\text{DMF})]$, $[1 \cdot \text{DMSO}]$, $[1 \cdot \text{DNB}]$, $[1 \cdot \text{NB}]$, $[1 \cdot \text{py}]$, $[1 \cdot \text{tz}]$, $[1 \cdot \text{dea}]$ and $[1 \cdot \text{MeOH}]$.⁴⁰ Their proton conductivity depended on the guest molecules, which was over $10^{-3} \text{ S cm}^{-1}$ under high humid

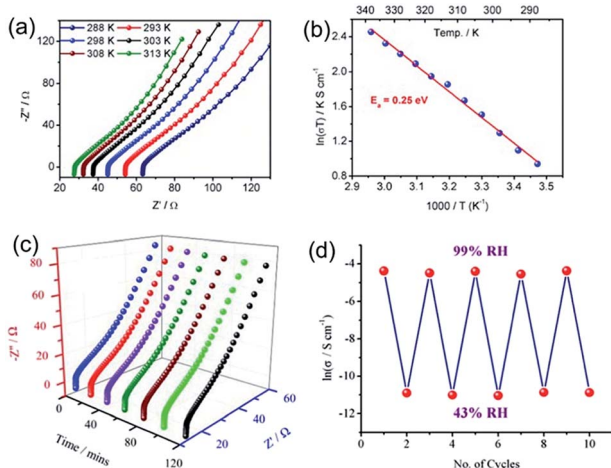


Fig. 10 (a) Nyquist curves of Im@MOF-808 under various temperatures and 99% RH. (b) Arrhenius plots of Im@MOF-808. (c) Nyquist curves of Im@MOF-808 at different times. (d) Humidity-dependent cycle of Im@MOF-808 between 43% and 99% RH at 300 K. (Reprinted with permission from ref. 38, Copyright 2019, American Chemical Society.)

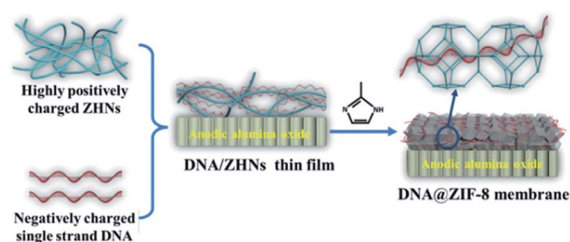


Fig. 11 Schematic diagram of the synthetic process of the DNA@ZIF-8 membrane. (Reprinted with permission from ref. 39, Copyright 2017, Wiley-VCH.)

conditions for all of them. This excellent performance may be ascribed to the effective hydrogen-bonded networks generated from the interaction of water molecules with the exchanged guest molecules, promoting the proton transfer efficiency. It should be mentioned that single-point energy computations were used to evaluate the anhydrous proton conductivity. Detailed calculations showed that the $[1 \cdot \text{DNB}]$, $[1 \cdot \text{NB}]$, $[1 \cdot \text{tz}]$, and $[1 \cdot \text{py}]$ adducts are stabilized by -0.868 , -0.427 , -0.57 , and 0.922 eV per guest incorporated compared to **1**, respectively, indicating they have no anhydrous proton conductivity. Only $[1 \cdot \text{dea}]$ exhibited low anhydrous proton conductivity. Two years later, the same group used the same parent CuI-MOF to incorporate a family of guest molecules, generating a series of derivatives, as follows: $[1 \cdot \text{pz}]$, $[\text{Cu}_4(\text{LHCl})_4(\text{I})_4(\text{pz} \cdot 2\text{HCl})]_n$ ($[1 \cdot \text{pz} \cdot 6\text{HCl}]$), $[\text{Cu}_4(4\text{L}_2\text{H}_2\text{SO}_4)_4(\text{I})_4(\text{pz} \cdot \text{H}_2\text{SO}_4)]_n$ ($[1 \cdot \text{pz} \cdot 3\text{H}_2\text{SO}_4]$), and $[\text{Cu}_{12}(12\text{L}_4\text{H}_3\text{PO}_4)(\text{I})_{12}(3\text{pz} \cdot 2\text{H}_3\text{PO}_4)]_n$ ($[1 \cdot \text{pz} \cdot 2\text{H}_3\text{PO}_4]$) (Fig. 12a).⁴¹ All of them exhibited proton conductive behaviour except $[1 \cdot (\text{DMF}) (\text{MeCN})]$ and $[1 \cdot \text{pz}]$ under anhydrous conditions. The maximum conductivity of $[1 \cdot \text{pz}]$ reached up to $2.77 \times 10^{-2} \text{ S cm}^{-1}$ at 80°C and 95% RH (Fig. 12b). $[1 \cdot \text{pz} \cdot 6\text{HCl}]$ exhibited high conductivity under both anhydrous and humid conditions at ambient temperature ($9.7 \times 10^{-6} \text{ S cm}^{-1}$ at 0°C and 0% RH; $2.48 \times 10^{-3} \text{ S cm}^{-1}$ at 25°C and 40% RH). At 80°C , under anhydrous conditions and 95% RH, these values increased to 2.17×10^{-2} and $2.94 \times 10^{-2} \text{ S cm}^{-1}$ respectively (Fig. 12c). $[1 \cdot \text{pz} \cdot 3\text{H}_2\text{SO}_4]$ showed anhydrous proton conductivity from $7.20 \times 10^{-6} \text{ S cm}^{-1}$ at 0°C to $3.83 \times 10^{-3} \text{ S cm}^{-1}$ at 80°C under 0% RH and water-dependent proton conductivity from $1.24 \times 10^{-2} \text{ S cm}^{-1}$ at 25°C to $3 \times 10^{-2} \text{ S cm}^{-1}$ at 75°C under 95% RH (Fig. 12d). The proton conductivity values of $[1 \cdot \text{pz} \cdot 2\text{H}_3\text{PO}_4]$ changed from $3.87 \times 10^{-7} \text{ S cm}^{-1}$ at 0°C and 0% RH and $1.67 \times 10^{-3} \text{ S cm}^{-1}$ at 25°C and 95% RH to $3 \times 10^{-5} \text{ S cm}^{-1}$ at 65°C and 0% RH and $1.25 \times 10^{-2} \text{ S cm}^{-1}$ at 75°C and 95% RH respectively (Fig. 12e). The results showed that various guest molecules can be incorporated into the framework to tune its proton conductivity.

A sulfonated indium framework (PCMOF-17) was reported with an anionic layered structure incorporating dimethylammonium cations and water molecules.⁴² PCMOF-17 was not stable if the RH is larger than 60%. The proton conductivity of the bulk PCMOF-17 samples was calculated to be $1.17 \times 10^{-3} \text{ S cm}^{-1}$ at 25°C and 40% RH. A large single crystal of PCMOF-17 was used to study its proton conductivity, which was compared with that obtained from the bulk sample at 25°C and 40% RH. The values

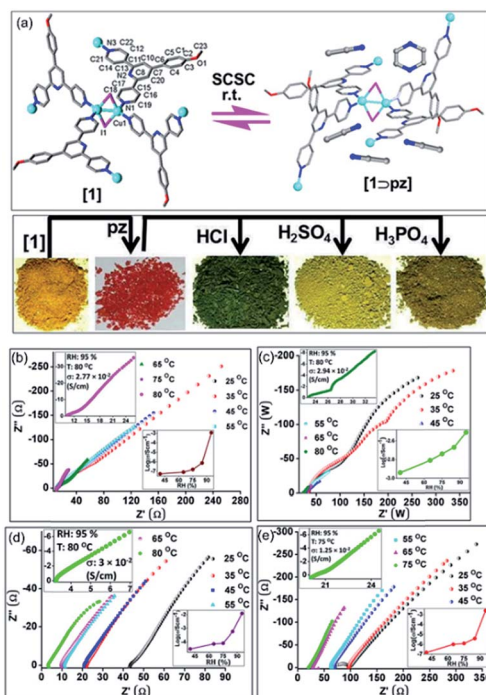


Fig. 12 (a) Structures of [1·(DMF (MeCN))] (left) and [1·pz] (right). C (gray), N (blue), O (red), I (pink), and Cu (cyan). Optical images of the bulk materials after exchange, where solvents and H atoms are omitted for clarity. Nyquist curves of (b) [1·pz], (c) [1·pz·6HCl], (d) [1·pz·3H₂SO₄], and (e) [1·pz·2H₃PO₄] under 95% RH at different temperatures. Inset: magnified Nyquist plots of the maximum proton conductivity (top left) and the humidity-dependent proton conductivity at room temperature (bottom right). (Reprinted with permission from ref. 41, Copyright 2018, Wiley-VCH.)

along the $[-110]$, $[110]$ and $[001]$ directions were 1.25×10^{-3} , 1.20×10^{-3} , and 8.66×10^{-5} S cm⁻¹, respectively (Fig. 13). The values along the $[-110]$ and $[110]$ directions compared well to that of the powder sample, which are supported by the hydrogen bonding network along two directions.

In the presence of water and NH₃ vapour, some CPs exhibit excellent proton conductive behaviour. Li group's devoted a lot of time and contributed greatly to this.^{43–46} Two types of 3D Co-based CPs, $\{[\text{Co}_3(m\text{-ClPhHIDC})_2(\text{H}_2\text{O})_6] \cdot 2\text{H}_2\text{O}\}_n$ (**1**) and $\{[\text{Co}_3(p\text{-ClPhHIDC})_3(\text{H}_2\text{O})_3] \cdot 6\text{H}_2\text{O}\}_n$ (**2**), were synthesized.⁴⁴ Subsequently, their proton conductivities under water and aqua-ammonia vapour were measured. The maximum values for the two CPs were 7.62×10^{-4} S cm⁻¹ at 100 °C under 98% RH and 2.47×10^{-4} S cm⁻¹ at 90 °C under 93% RH, respectively.

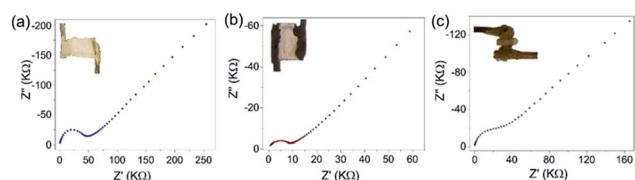


Fig. 13 Single-crystal Nyquist plots of PCMOF-17 along its (a) $[-110]$, (b) $[110]$ and (c) $[001]$ faces at 25 °C and 40% RH. (Reprinted with permission from ref. 42, Copyright 2017, American Chemical Society.)

Under water and aqua-ammonia vapour at 100 °C, the conductivity of **1** increased from 0.92×10^{-3} S cm⁻¹ (at an NH₃·H₂O concentration of 2.11 M) to 2.89×10^{-2} S cm⁻¹ (at 7.40 M). For **2**, its conductivity also increased from 3.02×10^{-3} S cm⁻¹ to 4.25×10^{-2} S cm⁻¹ under the same conditions (Fig. 14a). The experimental results showed that the values of **1** and **2** under aqua-ammonia vapour are 2 orders of magnitude higher than that under water vapour. It is interesting that both of them possess two types of mechanism depending on the temperature. The E_a for **1** at an NH₃·H₂O concentration of 4.93 M was 0.25 eV below 60 °C and 0.73 eV above 60 °C (Fig. 14b). The calculated results showed that when the temperature was lower than 60 °C, the Grothuss mechanism dominated the proton conduction, while at temperatures above 60 °C, the vehicle mechanism guides the proton conduction. For **2**, E_a is 1.58 eV (Fig. 14c), which matches well with vehicle mechanism. Another 2D CP, $[\text{Cu}(p\text{-IPhHIDC})]_n$, was considered as a proton conductive material and an ammonia sensor.⁴⁵ With the aid of numerous isolated carboxylate groups located on its layers, this CP exhibited good proton conductivity (1.51×10^{-3} S cm⁻¹ at 100 °C and 98% RH). By means of its good performance, this CP could detect NH₃ with the low detection limit of 2 ppm, and possessed ability for the highly selective detection of NH₃ over seven types of gases (N₂, H₂, O₂, CO, CO₂, benzene and MeOH) at room temperature and 68% RH. Besides, this CP was capable of sensing NH₃ reversibly. In 2019, a similar work was also reported by the same group. A 3D ionic CP, $\{[\text{Na}[\text{Cd}(\text{MIDC})]_n\}$, was successfully synthesized, which possessed 1D channels and uncoordinated carboxylate sites.⁴⁶ With the help of carboxylates, its proton conductivity reached up to 1.04×10^{-3} S cm⁻¹ (100 °C, 98% RH). At room temperature, this CP could sense ammonia and amine gases under 68%, 85%, and 98% RH, respectively, and its detection limits for ammonia, methylamine, dimethylamine, trimethylamine, and ethylamine were 0.05, 0.1, 0.5, 1 and 4 ppm, respectively.

An MIL-101 derivative (*i.e.* MIL-101-SO₃H) based on Cr and BDC-SO₃H was constructed, which possessed excellent chemical stability. To adjust its proton conductivity properties,

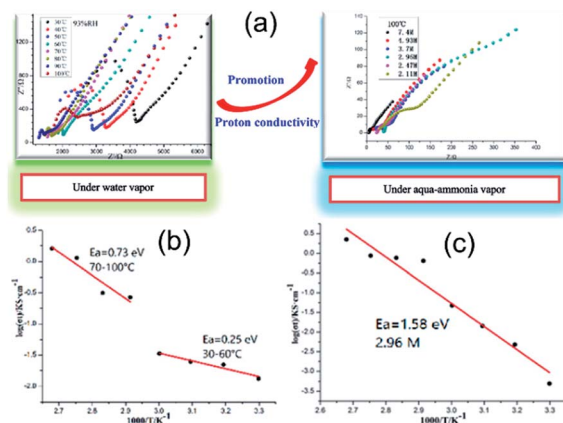


Fig. 14 Proton conductivities of **1** and **2** under aqua-ammonia vapor are greater than that under water vapor (a). Arrhenius curves of the proton conductivities for (b) **1** and (c) **2** under an NH₃·H₂O concentration of 4.9 M and 2.96 M in the range of 30–100 °C. (Reprinted with permission from ref. 44, Copyright 2017, American Chemical Society.)

different amounts of sulphuric acid was loaded into its framework, generating a series of $\text{H}_2\text{SO}_4@\text{MIL-101-SO}_3\text{H}$. Among them, the best proton conductivity value of 1.82 S cm^{-1} (70°C , 90% RH) was obtained, which could still maintain the value of $0.92 \times 10^{-2} \text{ S cm}^{-1}$ at -40°C .⁴⁷ Its superior performance surpasses that of all reported CP-based proton-conducting materials to date, especially under subzero temperature (-40°C). The hydrogen-bonded network in the pores formed by the three types of proton sources (H_2O , H_2SO_4 , and $-\text{SO}_3\text{H}$) provides an efficient proton-transfer pathway, leading to the excellent performance (Fig. 15).

Three types of Keggin-type $\text{H}_3\text{PW}_{12}\text{O}_{40}$ (HPW) with different masses incorporated in MIL-101 materials, namely **1**, **2** and **3**, were synthesized, and employed as suitable models to investigate the influence of the proton-conducting pathway on conductivity.⁴⁸ HPW with a reasonable nano-size were located inside the MIL-101 framework, and constructed two types of proton-conducting pathways, linear pathway and zigzag pathways. 38.2 wt%, 46.9 wt%, and 83.9 wt% of HPW were loaded in samples **1**, **2**, and **3**, which were consistent with the theoretical values (37.0 wt%, 44.4 wt%, and 81.4 wt%), respectively. The pore size distribution demonstrated that HPW exist in cage B of **1**, cage A of **2** and both cages of **3**. The proton conductivities of **1**–**3** followed the order of $1 < 2 < 3$ at 80°C and 100% RH, which may be due to the difference in their proton conducting pathways. The linear pathway may be a good choice for improving the proton conductivity. Thus, to further improve the proton conductivity of **3**, polyamines such as EN, DETA, TETA, and TEPA were selected to decorate it, defined as **EN@3**, **DETA@3**, **TETA@3** and **TEPA@3**, respectively, which displayed intact structures as confirmed by their PXRD patterns (Fig. 16). Among them, **TETA@3** exhibited the best performance ($1.52 \times 10^{-2} \text{ S cm}^{-1}$), which was higher than that of **TEPA@3** ($9.60 \times 10^{-3} \text{ S cm}^{-1}$) and **EN@3** ($6.02 \times 10^{-4} \text{ S cm}^{-1}$). In addition, **TETA@3** also exhibited excellent long range reversibility under the operating conditions. The experimental results suggested that the synergistic effect of polyamines, HPW and MIL-101 is very important for improving the proton conducting property.

Two types of strategies, isomorphous ligand replacement and heterocycle doping, were explored by Kim *et al.* to improve the proton conductivity of PCMOF2 (Fig. 17).⁴⁹ Four types of isostructural frameworks, PCMOF2_{1/2}(Pz), PCMOF2_{1/2}(Tz), PCMOF2 (Pz) and PCMOF2 (Tz), were synthesized *via* the

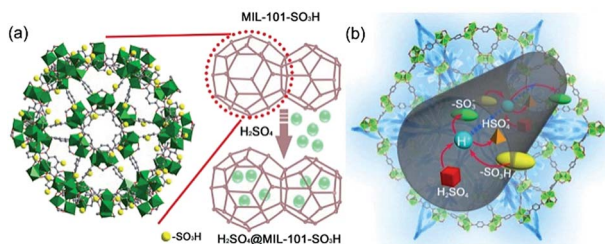


Fig. 15 (a) Sketch of $\text{H}_2\text{SO}_4@\text{MIL-101-SO}_3\text{H}$ ($-\text{SO}_3\text{H}$ groups (yellow balls)). (b) Possible proton-conductive mechanism for $\text{H}_2\text{SO}_4@\text{MIL-101-SO}_3\text{H}$. (Reprinted with permission from ref. 47, Copyright 2017, American Chemical Society.)

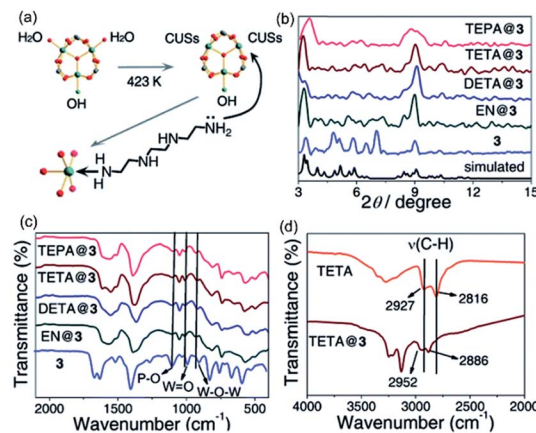


Fig. 16 (a) Schematic view of the dehydrated chromium(III) centers in **3** doped with TETA. (b) PXRD patterns of simulated MIL-101, **3**, and polyamines@**3**. (c) IR spectra of **3** and polyamines@**3**. (d) IR spectra of TETA (in the liquid phase) and TETA@**3**. (Reprinted with permission from ref. 48, Copyright 2017, Royal Society of Chemistry.)

aforementioned strategies. The generated PCMOF2_{1/2}(Pz) and PCMOF2_{1/2}(Tz) exhibited conductivity values of over $10^{-1} \text{ S cm}^{-1}$ at 85°C and 90% RH, which were 2 orders of magnitude higher than that of β -PCMOF2. Thus, to find the possible mechanism, two other frameworks, PCMOF2(Im) and PCMOF2_{1/2}(Im), were also synthesized. The improved conductivity may be ascribed to the difference in $\text{p}K_a$ among the three heterocycles. The $\text{p}K_a$ of the Pz and Tz cations is closer to that of

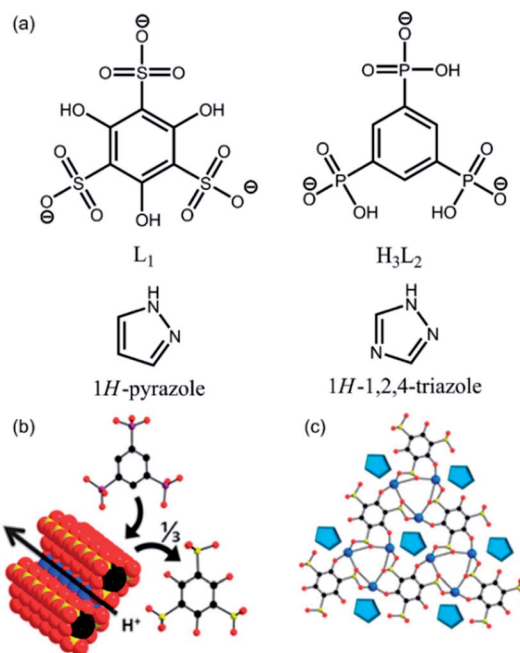


Fig. 17 (a) Structures of used organic linkers, 1H-pyrazole, and 1H-1,2,4-triazole. (b) space-filling structure of β -PCMOF2 and a schematic illustration of its isomorphous replacement. (c) Sheet of β -PCMOF2 with its pores filled with heterocycles (teal pentagons). (Reprinted with permission from ref. 49, Copyright 2017, American Chemical Society.)

hydronium cations, facilitating the generation of efficient proton transfer pathways.

Ethylene glycol (EG) can be used as isomorphous ligands to decorate the structure of CPs. Three CPs, $\text{Mg}(\text{C}_8\text{O}_4\text{H}_4)(\text{C}_5\text{NOH}_5)$ (1), $\text{Cd}(\text{C}_8\text{O}_4\text{H}_4)(\text{C}_5\text{NOH}_5)$ (2) and $\text{Nd}_2(\text{C}_8\text{O}_4\text{H}_4)_3(\text{C}_5\text{NOH}_5)_2 \cdot (\text{DMF})_x$ (3), have been obtained as the model structures.⁵⁰ Compounds 1 and 3 were exchanged with EG, giving **1@EG** and **3@EG**. The EG-loaded composites exhibited conductivity values of 1.08×10^{-3} and $1.72 \times 10^{-3} \text{ S cm}^{-1}$, respectively at 90 °C and 90% RH, which were 1000-fold times higher than that of the original samples. Loading EG into the framework constructs a modified proton transport pathway, resulting in enhanced conductivities and very low activation energy (0.11 eV).

The same strategy was applied to a new Zr(IV)-based CP, **VNU-17** [$\text{Zr}_6\text{O}_8(\text{H}_2\text{O})_8(\text{HSNDC})_4$], which was explored to enhance its proton conductivity with the help of sulfonate moieties (Fig. 18a).⁵¹ The resulting **VNU-17** framework possessed 6 Å channels, and could act as a host for the loading of imidazole molecules. Im was anchored on the internal surface within the structure (Fig. 18b). The Im-loaded samples, **Im11@VNU-17**, exhibited increased proton conductivity ($5.93 \times 10^{-3} \text{ S cm}^{-1}$) at 70 °C and 85% RH, 900 times higher than the parent **VNU-17**, and possessed a reversible cycle ability. In the same year, this group adopted the same strategy to anchor histamine to a new Zr(IV)-based CP, [$\text{Zr}_6\text{O}_8(\text{H}_2\text{O})_8(\text{H}_2\text{SNDC})_4$], named **VNU-23**, with rich sulfonic acid groups inside 6 Å channels, generating **histamine@VNU-23**.⁵² Obviously, the proton conductivity value of this material was $1.79 \times 10^{-2} \text{ S cm}^{-1}$ at 95 °C and 85% RH. Additionally, its performance could be maintained for at least 120 h.

Generally, acids or nitrogenous heterocyclic rings are introduced into CPs to improve their proton conductivity; however, the examples of metal ions applied to enhance their proton conductivity are rare. Vaidhyanathan's group discovered a CP, **Mg(Tp)(PyOH)**, where the protons of the zwitterionic pyridinol in its structure were partially substituted by Cs^+ ions, leading to a 4 order of magnitude increase in proton conductivity (10^{-6} to $10^{-2} \text{ S cm}^{-1}$).⁵³ A value of $1.61 \times 10^{-2} \text{ S cm}^{-1}$ (90 °C and 90% RH) was obtained. The hydration of Cs^+ ions gathers more water molecules, and facilitates the generation of hydrogen-bonded

transport pathways, resulting in a sharp increase in the conductivity (Fig. 19). The Cs^+ -loaded samples possessed a lower activation energy (0.19 eV) than the original samples (0.35 eV), indicating the Grotthuss mechanism manipulates proton conduction.

2.1.1.3 Functional groups. To improve the proton conductivity of CPs, organic linkers containing functional groups, for example, sulfonate groups and carboxylic groups, have been widely employed in the construction of CPs. Functional groups located on the surfaces of channels can make the channels hydrophilic and full of intermolecular H-bonding networks. Actually, under humid conditions, proton transport pathways may be easily generated by means of extended hydrogen bond networks constructed from water molecules and the adjacent functional groups in the channels, leading to excellent proton conductivities.

In 2017, Li's group reported a series of CPs with high chemical stability, which possessed excellent performances in proton conduction. A stable and flexible CP, **BUT-8(Cr)**, with rich sulfonic acids ($-\text{SO}_3\text{H}$) on its 1D channel surfaces was used for proton conduction.⁵⁴ This framework is chemically stable and the structure is flexible. Applying this framework as the host, **BUT-8(Cr)** was exchanged with H_2SO_4 to replace the $\text{NH}_2(\text{CH}_3)_2^+$ counter ions, giving **BUT-8(Cr)A**. At 100% RH and 80 °C, both of them exhibited high values of 4.63×10^{-2} and $1.27 \times 10^{-1} \text{ S cm}^{-1}$, respectively. The E_a of **BUT-8(Cr)A** and **BUT-8(Cr)** was 0.11 and 0.21 eV, respectively, indicating the Grotthuss

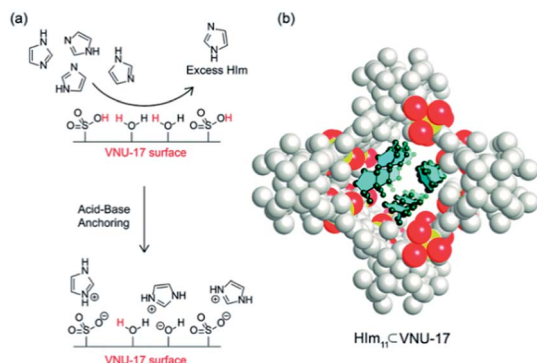


Fig. 18 Possible arrangement of anchoring imidazole on the internal surface of **VNU-17** (a) and possible positions in the crystal structure of **Im11@VNU-17** determined by the PXRD patterns (b). C (black); O (red); S (yellow); **VNU-17** backbone (white). (Reprinted with permission from ref. 51, Copyright 2017, Royal Society of Chemistry.)

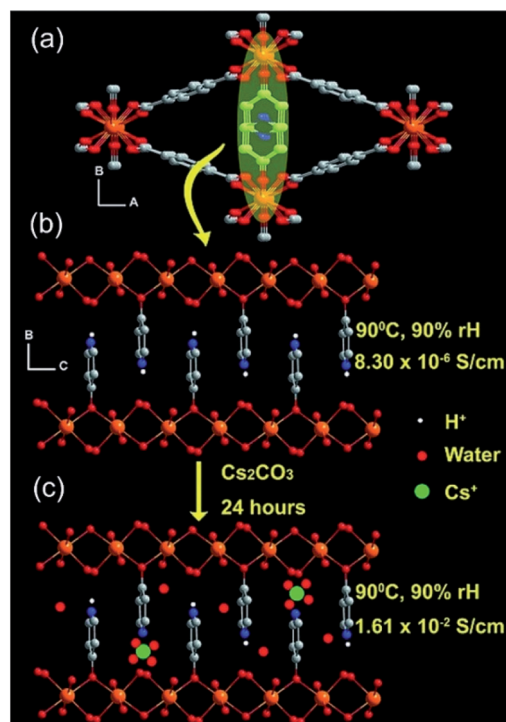


Fig. 19 (a) Rhombic-shaped channels with the protonated pyridinols. (b) Cross-sectional view of the channels along the a direction with the zigzag arrangement of the pyridinols. (c) Free doping of Cs^+ (ca. 10%) results in a 10 000-fold increase in conductivity. Mg (orange); O (red); C (gray); Cs (green); N (blue). (Reprinted with permission from ref. 53, Copyright 2016, Wiley-VCH.)

mechanism dominates the proton conduction process. The large number of SO_3H sites combined with the structural flexibility resulted in high proton conductivity. In the same year, the same research group reported a new porphyrinic CP $[\text{Co}(\text{DCDPP})]\cdot 5\text{H}_2\text{O}$ with open channels full of rich free carboxylic groups.⁵⁵ Employing the CP as a proton conductive material, high proton conductivity ($3.9 \times 10^{-2} \text{ S cm}^{-1}$) from a single crystal was obtained at 80°C and 97% RH (Fig. 20). Furthermore, this CP showed excellent conductivity durability. Three isostructural CPs, $[\text{Ni}_8(\text{OH})_4(\text{H}_2\text{O})_2(\text{BDP-X})_6]$ (**Ni-BDP-X**; $\text{X} = \text{CHO}, \text{CN}, \text{and COOH}$) were synthesized to test their proton conduction properties.⁵⁶ All these CPs were stable in boiling water and 4 M sodium hydroxide solution. The different functional groups resulted in different performances. **Ni-BDP** functionalized by COOH gave the best proton conductivity ($2.22 \times 10^{-3} \text{ S cm}^{-1}$ at 80°C and 97% RH) (Fig. 21). On the contrary, **Ni-BDP** with other functional groups gave lower proton conductivity performances. The experimental results suggest the functional groups are important in tuning the proton conduction properties of CPs.

Moreover, a Zr-based CP $\text{UiO-66}(\text{Zr})-(\text{CO}_2\text{H})_2$ with high water stability was evaluated for its proton conductive behaviours ($2.3 \times 10^{-3} \text{ S cm}^{-1}$ at 90°C and 95% RH).⁵⁷ The deduced E_a was 0.17 eV, indicating an efficient water-mediated proton transport pathway exists. To find this proton transport pathway, QENS experiments were performed. Meanwhile, aMS-EVB3 molecular dynamics simulations that could calculate the dynamics of both protons and water molecules were performed. Both of them revealed that the proton transport pathway is supported by hydrogen-bonded water networks arranged from the tetrahedral to the octahedral cages (Fig. 22). It should be mentioned that this is a rare example of proton conduction experiment and theoretical calculation being employed together to reveal the proton-conduction mechanism in a conductive CP.

2.1.2 Anhydrous proton conductivity. Commercial PEMFCs based on Nafion electrolyte can be operated well under

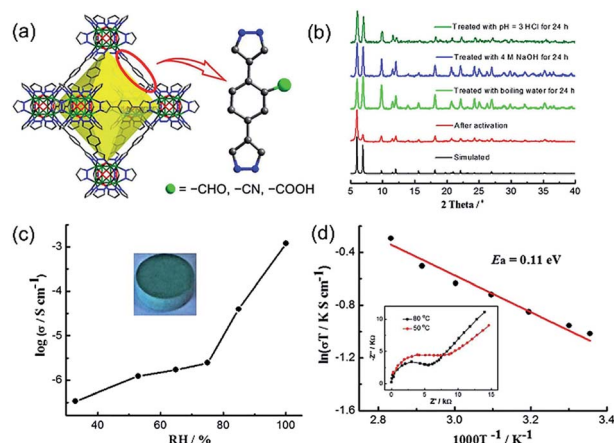


Fig. 21 (a) Structure of Ni-BDP and its derivatives Ni-BDP-X. (b) PXRD patterns of Ni-BDP-COOH before and after treatment under different conditions. (c) Humidity-dependent impedance plots of Ni-BDP-COOH at 25°C and 33–97% RH; inset: optical image of Ni-BDP-COOH pellet. (d) Arrhenius curves of Ni-BDP-COOH; inset: impedance curves of Ni-BDP-COOH at 97% RH. (Reprinted with permission from ref. 56, Copyright 2017, Wiley-VCH.)

moderate temperatures ($60\text{--}80^\circ\text{C}$) and high RH (98%). However, when the temperature is above 80°C , the loss of inner water molecules leads to poor conductivity. Perovskite-type oxide-based conductors are usually operated at temperatures above 600°C , which is too high for practical applications. CPs are promising candidates because they are crystalline inorganic–organic hybrid materials, which combine the advantages of organic polymers and inorganic oxides. Furthermore, N-rich heterocycles (e.g., imidazole) usually act as proton carriers, and have been impregnated into CPs, giving birth to composite materials. CPs can distribute proton carriers uniformly and arrange them in an orderly manner, enhancing their proton conductivity. Some successful reports will be listed here. For example, three ionic liquid-loaded CPs (*i.e.* **SA-EIMS@MIL-101**,

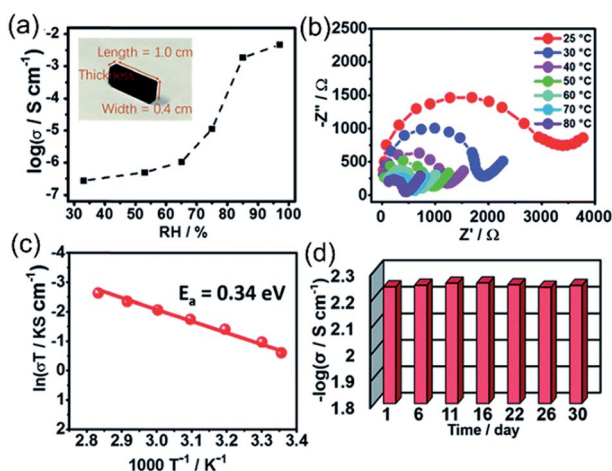


Fig. 20 (a) Conductivity of BUT-83 under different humidity at 25°C , (b) impedance at different temperatures and 97% RH, (c) Arrhenius plots; and (d) cycling test at 25°C and 97% RH. (Reprinted with permission from ref. 55, Copyright 2017, Royal Society of Chemistry.)

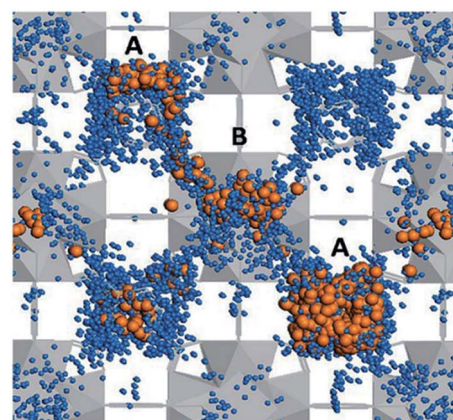


Fig. 22 Representation of the transport pathway mediated by water (blue) and the proton (orange) inside two types of cages (A) and (B) in $\text{UiO-66}(\text{Zr})-(\text{CO}_2\text{H})_2$, resulting from aMS-EVB3-MD simulations at 450 K. (Reprinted with permission from ref. 57, Copyright 2018, Wiley-VCH.)

MSA-EIMS@MIL-101 and **PTSA-EIMS@MIL-101**) with different acid counter anions were synthesized (Fig. 23).⁵⁸ This type of material displayed high anhydrous proton conductivity, and long-time stability even if at 150 °C and exposed to air. **SA-EIMS@MIL-101** is the best and could achieve a value of $1.89 \times 10^{-3} \text{ S cm}^{-1}$ because counter anion volumes may influence the proton conductivity and a smaller volume is more favourable for the proton transfer.

A pillared-layered structure with azobenzene side groups **Cu₂(F2AzoBDC)₂(dabco)** was synthesized, where *trans*-*cis* isomerization occurred when it was irradiated with light.⁵⁹ The matrix structures loaded with 1,4-butanediol or 1,2,3-triazole were defined as **butanediol@Cu₂(F2AzoBDC)₂(dabco)** and **1,2,3-triazole@Cu₂(F2AzoBDC)₂(dabco)**, respectively. **Butanediol@Cu₂(F2AzoBDC)₂(dabco)** showed a conductivity of $9.0 \times 10^{-8} \text{ S cm}^{-1}$ in the *trans* state and $6.1 \times 10^{-8} \text{ S cm}^{-1}$ in the *cis* state. The conductivity values of **1,2,3-triazole@Cu₂(F2AzoBDC)₂(dabco)** were reversible between $1.2 \times 10^{-6} \text{ S cm}^{-1}$ (*trans*) and $7.9 \times 10^{-7} \text{ S cm}^{-1}$ (*cis*) (Fig. 24). The experimental results revealed that the switch between high conductivity (*trans*) and low conductivity (*cis*) is induced by light. Quantum chemical calculations and infrared spectroscopy showed that this unique phenomenon is due to the different strengths of the hydrogen bonds formed between the conductive guest and azobenzene moieties, and the hydrogen bonds in the *cis* state are stronger than that in the *trans* state, which may hinder the mobility of the guest molecules.

2.1.3 Proton conductivity in composite membranes. Pure MIL-101 [$\text{Cr}_3\text{O}(\text{H}_2\text{O})_3(\text{bdc})_3$], S-MIL-101[$\text{Cr}_3\text{O}(\text{H}_2\text{O})_3(\text{STA})_3$] $\cdot n\text{H}_2\text{O}$, and MIL-101 doped with acids (H_2SO_4 , H_3PO_4 or $\text{CF}_3\text{SO}_3\text{H}$), namely acids@MIL-101 and chitosan (CS) were used in the construction of hybrid membranes, which were defined as **CS/MIL-101-X**, **CS/H₂SO₄@MIL-101-X**, **CS/H₃PO₄@MIL-101-X**, **CS/CF₃SO₃H@MIL-101-X** or **CS/S-MIL-101-X** ($X = 2, 4, 6, 8, 10, 12, 14$ or 16 , representing the weight percentage of the particles based on chitosan).⁶⁰ The conductivity values of **CS/H₂SO₄@MIL-101-8**, **CS/H₃PO₄@MIL-101-6**, **CS/CF₃SO₃H@MIL-101-10** and **CS/S-MIL-101-4** were 0.095, 0.083, 0.094, and 0.064 S cm^{-1} , respectively. All of them exhibited enhanced proton conductivities owing to the good interface compatibility between CP-based materials and CS (Fig. 25a-d). It should be mentioned that although the conductivity of **CS/S-MIL-101-4** is lower than those of **CS/H₂SO₄@MIL-101-8**, **CS/H₃PO₄@MIL-101-6**, **CS/**

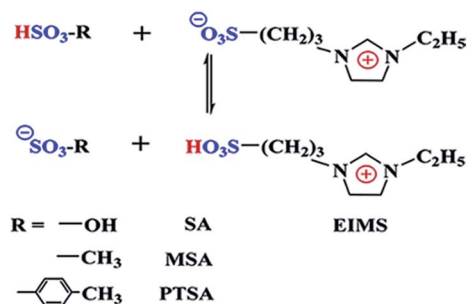


Fig. 23 Diagram of the used ionic liquids SA-EIMS, MSA-EIMS and PTSA-EIMS. (Reprinted with permission from ref. 58, Copyright 2017, ScienceDirect.)

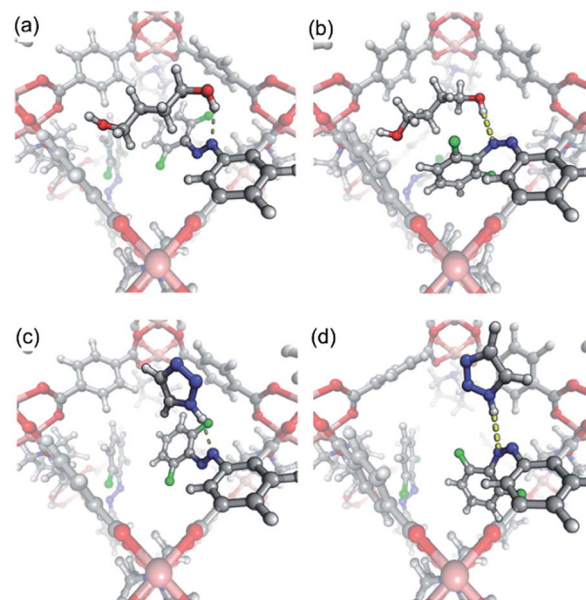


Fig. 24 Binding of butanediol (a and b) and triazole (c and d) with an azo linker in the pores of **Cu₂(F2AzoBDC)₂(dabco)** with the *trans* (a and c) and *cis* (b and d) conformations. The thickness of the dotted lines shows that the binding is stronger in the *cis* configuration than in the *trans* configuration. C (gray), N (blue), O (red), Cu (pink), F (green), or H (white). (Reprinted with permission from ref. 59, Copyright 2018, Wiley-VCH.)

CF₃SO₃H@MIL-101-10, its E_a (0.174 eV) is lowest among them. The investigation reveals that the sulfonic groups of the ligand can effectively promote the proton transport and prevent water molecules from escaping (Fig. 25e).

A new approach “ship in a bottle” was proposed to prepare a poly(ionic liquid)-incorporated CP for hydroxide conductivity. Using an *in situ* method, poly *N*-vinylimidazolium was successfully introduced into MIL-101, and then mixed with a styrene-ethylene/butylene-styrene triblock copolymer to prepare membranes *via* the hot-press method (Fig. 26).⁶¹ This CP-based membrane could obtain a high conductivity value of 36.6 mS cm^{-1} even at a low ion concentration ($0.633 \text{ mmol cm}^{-3}$ at 20 °C), which was 6 orders of magnitude larger than that of the pristine MIL-101. It should be noted that the hydroxide ion transport efficiency was 36.64% at 20 °C, 113% higher compared with the H^+ conduction property in Nafion. Using the same approach, the same group employed chloromethylated MIL-101(Cr) combined with chloromethylated PEEK to produce a PEEK/imidazolium MIL-101(Cr) (**ImPEEK/ImMIL-101(Cr)**) anion membrane.⁶² This membrane was exchanged with OH^- to replace Cl^- . Among the synthesized membranes, when 5.0 wt% **ImMIL-101(Cr)** was loaded into the membrane, the hydroxide conductivity reached the highest and then decreased with an increase in the amount of **ImMIL-101(Cr)**. At 60 °C, the highest value for the **ImMIL-101(Cr)** membrane reached up to 0.047 S cm^{-1} , which was higher than that of the pure membrane.

Moreover, a strategy has been developed to improve the long-range-order proton conductivity by means of hybrid

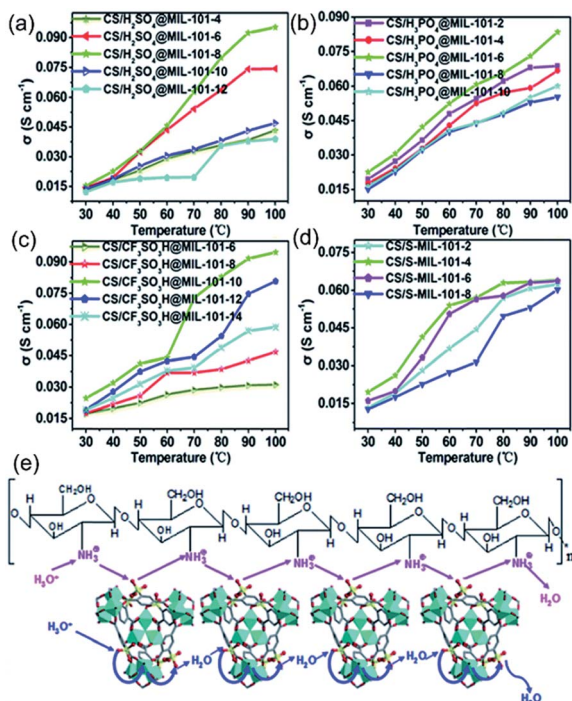


Fig. 25 (a–d) Proton conductivity of hybrid membranes at 100% RH. (e) The possible proton transport pathway in the CS/S-MIL-101-4 membrane. (Reprinted with permission from ref. 60, copyright 2017, Royal Society of Chemistry).

membranes based on sulfated CPs. Microcrystalline sulfated samples, Zr-MOF-808 ($\text{Zr}_6\text{O}_5(\text{OH})_3(\text{BTC})_2(\text{SO}_4) \cdot 2.5(\text{H}_2\text{O})_{2.5}$, denoted as **SZM**), were prepared and then dispersed in *N,N*-dimethylacetamide to combine with Nafion (Naf) solution, generating a series of hybrid membranes (**Naf-XSZM**, *X* represents the mass percentage. *X* = 1, 5, 7.5 and 10) (Fig. 27).⁶³ The electrode materials constructed from **Naf-XSZM** hybrid membranes exhibited better performances than the commercial Naf under low humidity, and among them, **Naf-1SZM** possessed the highest value of 2.96 mS cm^{-1} (35% RH, 80 °C), which may be attributed to the strong interactions formed between water molecules and the acidic moiety even at

high temperature in **SZM**, as supported by the thermogravimetric-mass spectrometry (TG-MS) study.

Wu's group devoted great effort in the construction of CP-based membranes.^{64–67} In their study, two CPs, UiO-66-SO₃H and UiO-66-NH₂, with different functional groups were constructed.⁶⁴ A family of Nafion-based proton exchange membranes (PEMs) decorated with single or two CPs was also prepared. The experimental results showed that the proton conductivity value of the PEMs decorated with the two CPs (**UiO-66-NH₂ + UiO-66-SO₃H/Nafion-0.6**) was up to 0.256 S cm^{-1} (90 °C, 95% RH), which was 1.17 times greater than that of the recast Nafion (0.118 S cm^{-1}) (Fig. 28). The excellent performance may be attributed to the synergistic effect between the two CPs and Nafion. CPs with the ionic clusters and pores can lock water molecules, and endow PEMs with high water retention capacity, leading to the generation of efficient hydration channels in the composite PEM. Additionally, the co-doped PEMs also possessed high proton conductive stability at 90 °C, 95% RH. Based on the previous work, graphene oxide (GO) with rich oxygen functional groups was introduced to modify the membranes, which possessed good proton conduction and excellent barrier effect. The new modified composite PEMs based on UiO-66-NH₂, graphene oxide (GO) and Nafion matrix presented high performances under both high humidity and anhydrous conditions.⁶⁵ The proton conductivity of the as-prepared composite membrane **GO@UiO-66-NH₂/Nafion-0.6** reached up to 0.303 S cm^{-1} at 90 °C, 95% RH, and $3.403 \times 10^{-3} \text{ S cm}^{-1}$ under anhydrous condition, which is about 1.57 and 1.88 times higher than that of the recast Nafion (0.118 S cm^{-1} and $1.182 \times 10^{-3} \text{ S cm}^{-1}$), respectively. Several influencing factors have been considered to investigate the conductivity. The acid/base pairs formed by –SO₃H of Nafion and –NH₂ of UiO-66-NH₂ provide effective proton transfer pathways, and the available cavity and small size of UiO-66-NH₂ can further enhance the water retention capacity of PEMs, resulting in the enhancement of proton conductivity (Fig. 29). In the same year, the same group employed S-UiO-66 with functional groups of –SO₃H, graphene oxide (GO) and sulfonated PEEK

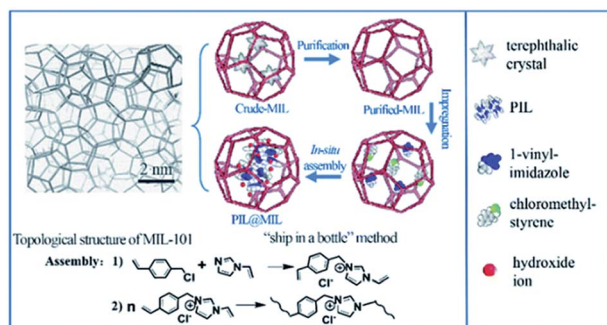


Fig. 26 Self-assembly process of PIL@MIL101(Cr) through the "ship in a bottle" approach. (Reprinted with permission from ref. 61, Copyright 2017, Royal Society of Chemistry.)

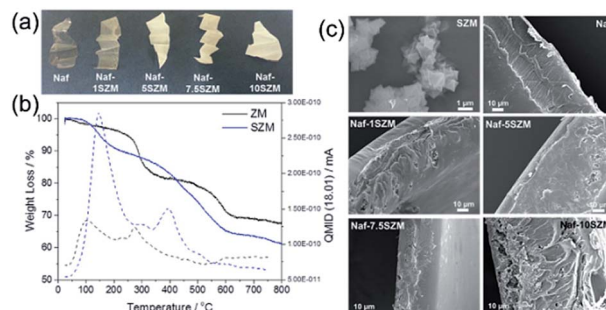


Fig. 27 (a) Optical images of Naf and Naf-XSZM hybrid membranes with different SZM loadings (1, 5, 7.5, and 10 wt%). (b) TG-MS and quasi multiple ion spectra (QMIS) of H₂O for ZM and SZM, indicating H₂O molecules bonded with Brønsted acid sites of SZM even if at high temperature and (c) the morphology of SZM and cross-sectional photographs of the Naf and Naf-XSZM membranes. (Reprinted with permission from ref. 63, Copyright 2018, American Chemical Society.)

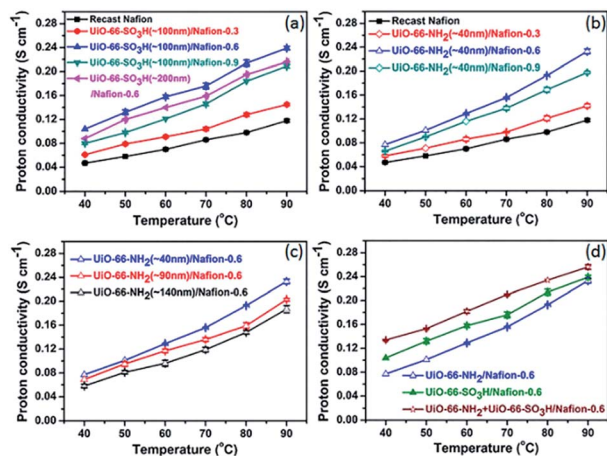


Fig. 28 Proton conductivities (95% RH) at different temperatures: (a) recast Nafion, UiO-66-SO₃H (~100 and ~200 nm)/Nafion, (b) recast Nafion, UiO-66-NH₂ (~40 nm)/Nafion, (c) UiO-66-NH₂ (~40, ~90, and ~140 nm)/Nafion-0.6; and (d) UiO-66-NH₂/Nafion-0.6, UiO-66-SO₃H/Nafion-0.6, and UiO-66-NH₂ + UiO-66-SO₃H/Nafion-0.6. (Reprinted with permission from ref. 64, Copyright 2017, American Chemical Society.)

(SPEEK) to prepare composite membranes. S-UiO-66 and GO were selected to prepare S-UiO-66@hybrid nanosheets *via* an *in situ* synthetic method. Various hybrid PEMs based on S-UiO-66@GO and SPEEK were prepared (Fig. 30a).⁶⁶ The as-synthesized SPEEK/S-UiO-66@GO indeed improved the proton conductivity significantly under various conditions. Particularly, the proton conductivity of SPEEK/S-UiO-66@GO-10 reached up to 0.268 S cm⁻¹ and 16.57 mS cm⁻¹ at 70 °C, 95% RH and 100 °C, 40% RH, better than that of recast SPEEK, respectively (Fig. 30b). This obvious improvement in proton conductivity may be attributed to the well-designed nanostructure and chemical composition of the membrane matrix. Rich -SO₃H groups and the uniform distribution of S-UiO-66 inside the membranes as well as well-connected ionic nanochannels between the surfaces of S-UiO-66@GO and the SPEEK matrix effectively facilitate the transfer of the protons (Fig. 30c). A similar work was also reported by the same group except that ZIF-8 and carbon nanotubes (CNT) were used to replace S-UiO-66 and GO.⁶⁷ Firstly, 2D ZIF-8/CNT hybrid cross-linked networks (ZCN) were synthesized, and then

a series of composite PEMs based on ZCN and SPEEK were prepared (Fig. 31). Due to the morphological and compositional features of ZCN, the proton conductivity of the SPEEK/ZCN membranes increased obviously under various conditions. In particular, the proton conductivity of the SPEEK/ZCN-2.5 membrane was the highest (50.24 mS cm⁻¹ at 120 °C, 30% RH), surpassing that of the other materials (the recast SPEEK membrane 4.50 mS cm⁻¹ and SPEEK/ZIF membrane 24.1 mS cm⁻¹). Both the well-connected cylindrical ionic nanochannels in the interfaces of ZCN and SPEEK and the holes between the neighbouring ZIF-8@CNT networks may be capable of promoting the transfer of protons.

The zirconium-based framework UiO-66 and isostructural sulfonated SO₃H-UiO-66 were also applied to fabricate mixed membrane matrices with Nafion.⁶⁸ The size of the microcrystallites, loading amount and the existence of sulfonic groups were systematically considered as influencing factors on the conductivity. The results showed that the Nafion membranes loaded with large UiO-66 crystals (200 nm average size) and low amounts (around 2%) possessed the highest proton conductivity values (0.207 S cm⁻¹, at 95% RH, 110 °C), 30% higher than that of pure Nafion. While, the Nafion membranes doped with UiO-66 with a small size (20 nm average size) showed no effect on proton conductivity. Furthermore, the sulfonated SO₃H-UiO-66 could not improve the conductivity of the Nafion membranes significantly at a low loading amount, and the conductivity decreased slightly with high loading values.

Another Zr-based CP, MOF-801, was selected by Ren and co-workers to prepare conductive membranes. They firstly studied the proton conductivity of the selected MOF-801, which showed a remarkable proton conductivity value of 1.88×10^{-3} S cm⁻¹ at 298 K and 98% RH. Then, they employed poly(vinylidene fluoride) and poly(vinylpyrrolidone) as the matrixes, and combine

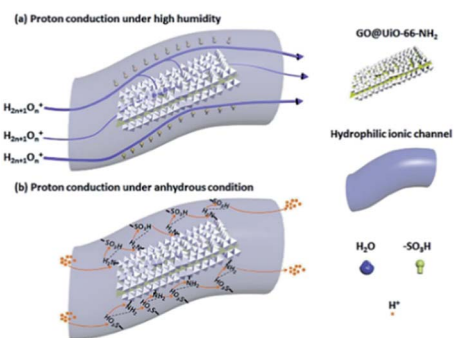


Fig. 29 Schematic diagram of proton conductivity enhancements ((a) under high humidity and (b) under anhydrous conditions). (Reprinted with permission from ref. 65, Copyright 2017, ScienceDirect.)

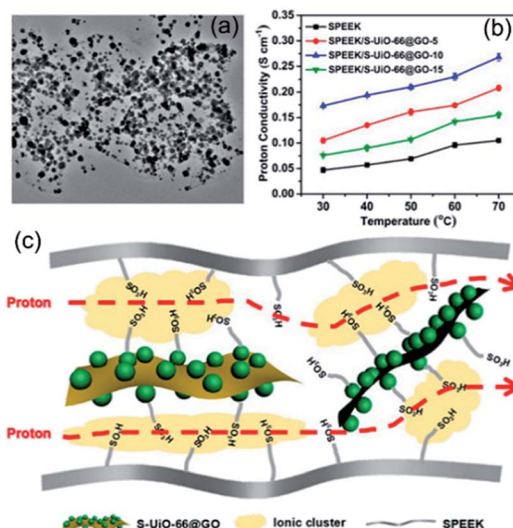


Fig. 30 TEM images of S-UiO-66@GO hybrid nanosheets with a uniform distribution. (b) Temperature-dependent proton conductivities under 95% RH (a). (c) Possible proton transport pathway of the SPEEK/S-UiO-66@GO membranes. (Reprinted with permission from ref. 66, Copyright 2017, American Chemical Society.)

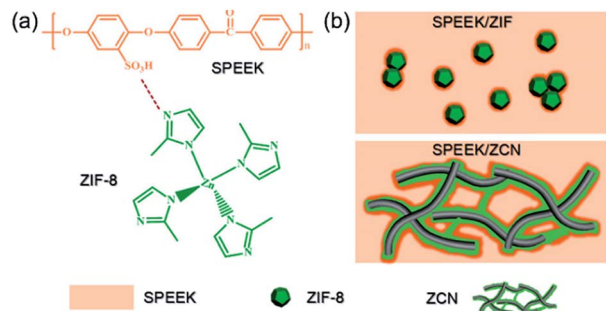


Fig. 31 (a) Strong interactions between SPEEK and ZIF-8, and (b) the simulated interface of SPEEK/ZIF or SPEEK/ZCN hybrid membranes. (Reprinted with permission from ref. 67, Copyright 2017, American Chemical Society.)

them with MOF-801 to fabricate composite membranes, named **MOF-801@PP-X**, where *X* represents the mass percentage of MOF-801.⁶⁹ Among the PEMs, **MOF-801@PP-60** exhibited the highest value of $1.84 \times 10^{-3} \text{ S cm}^{-1}$ at 52 °C and 98% RH. The composite membrane was successfully assembled into an H₂/O₂ fuel cell, implying that these membranes have potential to be used as PEMs.

A new hexaphosphate ester-based CP, **JUC-200**, was synthesized and showed a proton conductivity of $1.62 \times 10^{-3} \text{ S cm}^{-1}$ at 80 °C in pure water.⁷⁰ Based on its high proton conductivity, PVA and **JUC-200** were combined to prepare a series of composite membranes with different mass loadings of **JUC-200**, denoted as **JUC-200@PVA-X** (*X* shows the mass percentage). **JUC-200@PVA-10** exhibited excellent proton conductivity ($1.25 \times 10^{-3} \text{ S cm}^{-1}$ at 50 °C in pure water).

2.1.4 Proton conductivity in other materials. Recently, proton conductivity studies have been expanded to other crystalline materials (for example, POM-based hybrids and chalcogenide).^{73–78} These frameworks often possess rich hydrogen bond networks and ordered supramolecular structures or exhibit porous anionic architectures full of charge carriers. Probably, they may provide further insight for proton conductivity through their investigation.

Two inorganic porous frameworks based on [MnV₁₃O₃₈]^{7–} clusters and lanthanide ions (H[Ln(H₂O)₄]₂[MnV₁₃O₃₈])·9NMP·17H₂O (Ln = Ce and La) were synthesized by Zang's group, and their conductivities studied.⁷⁴ They showed proton conductivities of $4.68 \times 10^{-3} \text{ S cm}^{-1}$ and $3.46 \times 10^{-3} \text{ S cm}^{-1}$ at 61 °C and 97% RH for the Ce- and La-based structures, respectively. In addition, the D₂O-exchange test demonstrated the role of water molecules, and the Hebb–Wagner polarization technique confirmed that these materials are proton conductors.

Zheng's group and Khashab's group synthesized three inorganic hybrid POMs based on tungstate. H₁₄[Na₆(H₂O)₁₂]₄[K₄₂-Ge₈W₇₂O₂₇₂(H₂O)₆₀]·solvent reported by Zheng exhibited the highest value of $6.8 \times 10^{-2} \text{ S cm}^{-1}$ at 98% RH and 85 °C.⁷⁵ Meanwhile, K₈Na₃Li₅{[Na(NO₃)(H₂O)]₄[Al₁₆(OH)₂₄(H₂O)₈(P₈W₄₈-O₁₈₄)]}·66H₂O discovered by Khashab's group showed an excellent proton conductivity value of $4.5 \times 10^{-2} \text{ S cm}^{-1}$ (85 °C, 70% RH).⁷⁶

Lan's group made some achievements in crystalline POM-based conductive materials.^{77,78} Recently, an interesting work

was reported by them. Mo₁₃₂ is an anionic hollow spherical structure, and can hold a lot of guest molecules. By virtue of this feature, they employed Mo₁₃₂ as the matrix, and encapsulated it with a series of organic molecules (Im, MeIm, IL and TBA), generating HImMo₁₃₂, HMeImMo₁₃₂, ILMo₁₃₂ and TBAMo₁₃₂, respectively.⁷⁷ Among them, HImMo₁₃₂ exhibited a high proton conductivity of $4.98 \times 10^{-2} \text{ S cm}^{-1}$, which was 3 orders of magnitude larger than that of TBAMo₁₃₂. This example demonstrates the hollow spherical structure can offer more proton transfer ways than solid spheres due to the inner cavities and windows within the structure.

Chalcogenides are members of crystalline porous material family, which possess a zeolite-like anionic architecture and charge carriers in their pores. Combined with their excellent stability, chalcogenides have been explored as proton conductors. Ren's group developed this type of material as proton conductors.^{79,80} The experimental results displayed that chalcogenides exhibit proton conductive behaviours under humid and anhydrous conditions.

Moreover, a chalcogenide open-framework, (C₂N₂H₁₀) (C₂N₂-H₉)₂Cu₈Sn₃S₁₂ (**1**), was applied to study the proton conductivity after immersing it in HCl, giving **HCl·1**.⁷⁹ Its anhydrous proton conductivity was also good within a wide temperature range. A number of σ values were obtained, including 2.35×10^{-7} at –50 °C, 1.14×10^{-5} at 25 °C, 7.08×10^{-4} at 123 °C, 3.62×10^{-2} at 169 °C, and $1.03 \times 10^{-2} \text{ S cm}^{-1}$ at 190 °C. The low *E*_a of **HCl·1** indicates the Grotthuss mechanism mainly dominates the proton transfer. This high performance may make this material useful in the fuel-cell area. Two years later, another open-framework chalcogenide, (CH₃NH₃)₂Ag₄Sn₃S₈, and its derivative doped by hydrochloric acid were also explored for their conductivities. The doped composite displayed proton conductive behaviours in anhydrous and humid environments ($1.87 \times 10^{-4} \text{ S cm}^{-1}$ at 190 °C under an N₂ atmosphere and $1.14 \times 10^{-3} \text{ S cm}^{-1}$ at 67 °C and 99% RH), and also possessed cycling stability of proton conduction.⁸⁰

2.2 Alkali metal ion conductivity

In commercially available lithium batteries, organic solutions of lithium salt have been widely explored. However, due to their volatility and flammability (especially at high temperatures), there exist serious security risks. Thus, it is urgent to explore novel solid electrolyte materials to replace liquid systems. In particular, metal ion conduction for solid electrolytes still has plenty of room for improvement. To date, only a limited number of materials have been employed, for example polymer electrolytes. Recently, CPs have attracted increasing attention due to their following advantages: (1) the variety and tunability of their structures create diverse platforms, and provide an opportunity for rational design and mechanism investigation; (2) by means of post-synthetic modification method, various metal cations can be introduced into the their host framework to improve ion conductivity; and (3) the migration paths of metal cations can be accurately predicted with the help of crystalline structures. Recently, a small number of examples have been reported, mainly focusing on Li⁺ ions and Na⁺ ions (Table 2).^{106–128}

Table 2 Lists of selected ionic-conductive CPs in this review

Name in the ref.	Guest molecule	Condition	Conductivity/S cm ⁻¹	Ref.
Mg ₂ (dobdc)·0.35Li ⁺ OPr·0.25LiBF ₄ ·EC·DEC	Li ⁺ OPr/LiBF ₄	300 K	3.1 × 10 ⁻⁴	108
Dehydrated UiO-66	lithium <i>tert</i> -butoxide	298 K	1.8 × 10 ⁻⁵	109
(EMI _{0.8} Li _{0.2})TFSA@ZIF-8	(EMI _{0.8} Li _{0.2})TFSA	343 K	~10 ⁻⁴	110
Li-IL@MOF(UiO-67)	Li ⁺ ion ionic liquid solution	303 K	8.7 × 10 ⁻⁴	111
LPC@HKUST-1	LiClO ₄	298 K	0.38 × 10 ⁻³	112
EHU1(Sc,Li)	LiBF ₄	298 K	4.2 × 10 ⁻⁴	113
EHU1(Sc,Na)	NaPF ₆	298 K	9.2 × 10 ⁻⁵	113
[LiCo(PDC) ₂]	Li ⁺	298 K	Pellet 0.038 × 10 ⁻⁶	114
[LiCo(PDC) ₂]	Li ⁺	298 K	Single crystal 6.67 × 10 ⁻⁶	114
COF-5	LiClO ₄	298 K	0.26 × 10 ⁻³	119
Li-CON-TFSI	LiTFSI	343 K	2.09 × 10 ⁻⁴	120
Li@TPB-DMTP-COF	LiClO ₄	353 K	5.37 × 10 ⁻⁶	121
Li@TPB-BMTP-COF	LiClO ₄	363 K	5.49 × 10 ⁻⁴	121
Mg(OPhCF ₃) ₂ ·Mg(TFSI) ₂ ⊂Mg ₂ (dobpdc)	Mg(OPhCF ₃) ₂ and Mg(TFSI) ₂	298 K	0.25 × 10 ⁻³	126
MIT-20-Li	Li ⁺	343 K	4.4 × 10 ⁻⁵	127
MIT-20-Na	Na ⁺	343 K	1.8 × 10 ⁻⁵	127
MIT-20-Mg	Mg ²⁺	343 K	8.8 × 10 ⁻⁷	127
MOF-LiI	LiI	298 K	1.1 × 10 ⁻⁴	128
MOF-MgBr ₂	MgBr ₂	298 K	1.3 × 10 ⁻⁴	128

The immobilization of lithium ions into porous zeolites has been explored in solid electrolytes.^{106,107} Inspired by this, Long *et al.* creatively incorporated various lithium alkoxides into the Mg₂(dobdc) framework *via* post-synthetic modification method.¹⁰⁸ After removing the coordinated molecules of magnesium clusters, various alkyl groups were used to modify Mg₂(dobdc) (Fig. 32), and the performances of these modified frameworks were preliminarily investigated. The experimental results indicate that decoration with Li⁺OPr resulted in a better performance than the decoration with LiOMe, LiBF₄ or LiOEt. Finally, the ionic conductivity value of the pressed pellet sample modified by Li⁺OPr and LiBF₄ Mg₂(dobdc)·0.35Li⁺OPr·0.25LiBF₄·EC·DEC was 3.1 × 10⁻⁴ S cm⁻¹ at 27 °C. To study the role of LiBF₄, another sample, Mg₂(dobdc)₃·0.06LiO₃Pr₃·xEC/DC, was prepared, showing a reduced conductivity of 1.2 × 10⁻⁵ S cm⁻¹. Thus, the authors speculated that good interparticle conductivity may exist in the presence of LiBF₄, which was not demonstrated by the impedance plots of the pressed pellet samples. Fortunately, the crystallite features of Mg₂(dobdc) provided a good choice to verify this hypothesis. After soaking treatment, a single crystal was evaluated for its conductive behaviour, and a conductivity value of 5.5 × 10⁻⁵ S cm⁻¹ was obtained, implying it is true that intraparticle processes drive the conduction. This example is the first Li⁺ solid electrolyte based on CPs. Two years later, the same group took advantage of dehydrated and rehydrated UiO-66 frameworks to prepare a second metal ion conductive CP decorated by lithium *tert*-butoxide, where *tert*-butoxide anion groups were grafted in the open metal sites in the dehydrated framework.¹⁰⁹ The *tert*-butoxide anion groups deprotonated the μ₃-O atoms of the Zr₆ clusters and Li⁺ ions located around the accessible negative charge. The ionic conductivity of the dehydrated UiO-66 sample was calculated to be 1.8 × 10⁻⁵ S cm⁻¹ at room temperature, which was higher than that of the rehydrated samples (3.3 × 10⁻⁶ S cm⁻¹). Because Li⁺ ions locate near the deprotonated μ₃-O atoms with the negative charge, this slowed down their movement in the rehydrated samples. The experimental phenomenon implies that the bulky

aliphatic group can effectively decrease the interactions between Li⁺ ions and negative charges, and increase the mobility of Li⁺ ions.

ILs as guest species can also be used to mediate the ionic conductive behaviours of CPs. The blend of EMI-TFSA and LiTFSI generated a lithium ion-doped IL. Then incorporating this type of lithium IL into ZIF-8 produced (EMI_{0.8}Li_{0.2})TFSA@ZIF-8 (ELT@Z₁₀₀) for the first time, and its ionic conductivity induced by phase transition was studied.¹¹⁰ The authors systematically studied the dynamics of lithium ions and TFSA⁻ anions in the micropores of ZIF-8. Compared with TFSA⁻ anions, Li⁺ cations move slightly slower. Disappointingly, the ionic conductivity of ELT@Z₁₀₀ was lower than that of the bulk (EMI_{0.8}Li_{0.2})TFSA (ELT-bulk). However, the activation energy of ELT@Z₁₀₀ was almost equivalent with the bulk ELT-bulk because Li⁺ diffused through the channels by means of the substitution of the solvating TFSA⁻.

Adopting the same strategy, Wang and co-workers reported a host-guest composite ionic conductor (Li-IL@MOF, named LIM) which resulted from UiO-67 and the Li⁺ ion ionic liquid solution (Li-IL).¹¹¹ Loading different amounts of Li-IL guest molecules into UiO-67 host generated a family of LIM. As the amount of Li-IL guest increased, the ionic conductivity of LIM increased. When 2.0 mL Li-IL guest was used, the highest value (8.71 × 10⁻⁴ S cm⁻¹) was obtained as well as a wide chemical window (5.2 V) appeared. When LIM was hybridized with LiCoO₄ and LiFePO₄, acceptable rate capability and cycle stability were achieved. The results showed that increasing the ion transfer paths inside the UiO-67 host plays a key role in the improvement of ionic conductivity.

Ionic channels of biological systems inspired Shen and co-workers to employ HKUST-1 as the main matrix to generate ion electrolytes with negative channels.¹¹² As illustrated in Fig. 33b, HKUST-1 exhibits 3D channels, where coordinated molecules (for example, water) exist. Porous HKUST-1 with open metal sites can be generated by the departure of coordinated molecules. Then LiClO₄ is introduced into the framework, and

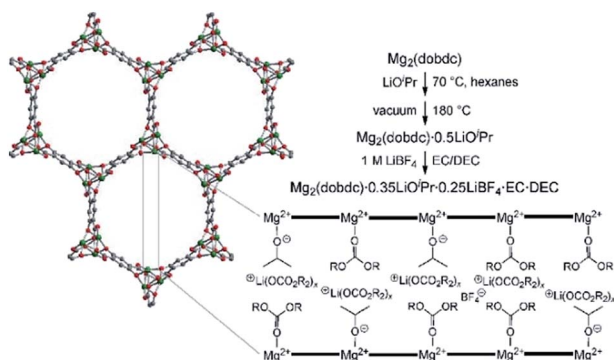


Fig. 32 Structure of $\text{Mg}_2(\text{dobdc})$ and schematic diagram of the synthetic routes for the solid electrolyte. The possible arrangements of alkyl groups within the solid electrolyte (lower right) ($\text{R} = \text{EC}$ or DEC). (Reprinted with permission from ref. 108, Copyright 2011, American Chemical Society.)

ClO_4^- ions could coordinate to the open metal sites, forming an anionic framework (**LPC@HKUST-1**). This negatively charged framework was able to transfer Li^+ ions (Fig. 33c), which presented an ion conductivity of 0.38 mS cm^{-1} and low activation energies ($< 0.21 \text{ eV}$). This example demonstrates that open metal sites play an irreplaceable role in ion conductivity.

Two types of heterometallic frameworks, named $\{[\text{ScM}(\mu_4\text{-pmdc})_2(\text{H}_2\text{O})_2] \cdot \text{solv}\}_n$ [**EHU1(Sc,Li)**] and [**EHU1(Sc,Na)**] were successfully synthesized.¹¹³ Both of them showed high resistivity. Two approaches were employed to improve their ionic conductivity. One approach was to replace part of Sc^{III} in the framework with valence transition metal ions (e.g., Cd^{II} and Mn^{II}), leading to additional interstitial Li^+ and Na^+ aquo complexes. The conductivity increased slightly. The other was to immerse these CPs into alkaline salts solutions (Fig. 34a). After soaking two samples in Li/Na solutions, the ionic conductivity at room temperature remarkably improved, where the value of **EHU1(Sc,Li)·(LiBF₄)** was $4.2 \times 10^{-4} \text{ S cm}^{-1}$, and that of **EHU1(Sc,Na)·(NaPF₆)** was $9.2 \times 10^{-5} \text{ S cm}^{-1}$ (Fig. 34b and c, respectively). It should be noted that the CPs remained intact after the soaking process. **EHU1(Sc,Na)** represents the first sodium ion conductive CP.

In 2017, Kim *et al.* synthesized a novel lithium cobalt CP, and successfully measured the ion conductivity performance of both the pellet and single crystal of $[\text{LiCo}(\text{PDC})_2]$.¹¹⁴ The conductive value for the pellet was $0.038 \mu\text{S cm}^{-1}$, and that for the single crystal was $6.67 \mu\text{S cm}^{-1}$ along the $[010]$ direction, which was larger than that of the pellet. It should be mentioned that the single crystal of $\text{LiCo}(\text{PDC})_2$ exhibited interesting anisotropic ion conduction, and no conductivity was observed in the other directions except the $[010]$ direction. This is the first example in which the ionic conductivity phenomenon is observed in a single crystal, which is an important breakthrough.

As materials similar to CPs, COFs contain ordered organic skeletons and channels, and possess the characteristics of porosity, diverse structures, and ease of modification, and may be good candidates for ion conductivity.^{115–121}

A 2D COF, **COF-5**, as well as hexagonal **COF-1** (boroxine),¹¹⁵ **TpPa-1** COF (β -ketoenamine),¹¹⁶ **CTF-1** (triazine),¹¹⁷ and tetragonal

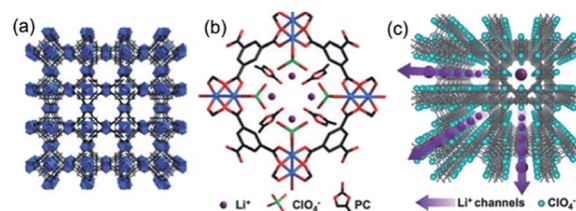


Fig. 33 (a) 3D structure of HKUST-1: copper nodes (blue) and BTC ligands (black). (b) Sketch of biomimetic ionic channels, where ClO_4^- anions coordinate to the OMSs and solvated Li^+ ions inside the channels (copper: blue; carbon: black; and oxygen: red). (c) Biomimetic ionic channels in HKUST-1 (dark gray) with ClO_4^- ions (cyan dots) and solvated Li^+ ions (purple dots). (Reprinted with permission from ref. 112, Copyright 2018, Wiley-VCH.)

ZnPC-BBA COF (boronate)¹¹⁸ were selected to investigate the relationship between their crystallographic anisotropies and ionic transport properties before and after they were mechanically pressed into pellets.¹¹⁹ The results demonstrated that all the selected samples exhibited similar crystallographic behaviours with a preferred orientation between the $hk0$ and $00l$ planes under mechanical pressure. However, only **COF-5** and **TpPa-1** exhibited ion conductive behaviours and **COF-5** was chosen to study the effect of mechanical treatment on Li^+ conduction. Putting a **COF-5** pellet into 1 M $\text{LiClO}_4/\text{THF}$ directly led to no Li^+ conduction, while loading the **COF-5** powder with LiClO_4 before mechanical processing (pressed at 4 MPa) resulted in significant Li^+ ion conductivity (0.26 mS cm^{-1} at room temperature).

Chen and co-workers designed and synthesized a COF framework (**CON-Cl**) based on cationic moieties. The ion-exchanged process between **CON-Cl** and **LiTFSI** generated **Li-CON-TFSI**, which exhibited a conductivity of $2.09 \times 10^{-4} \text{ S cm}^{-1}$ at 70°C .¹²⁰ Raman spectra and ^7Li solid-state NMR revealed that its excellent ionic conductivity may result from complicated

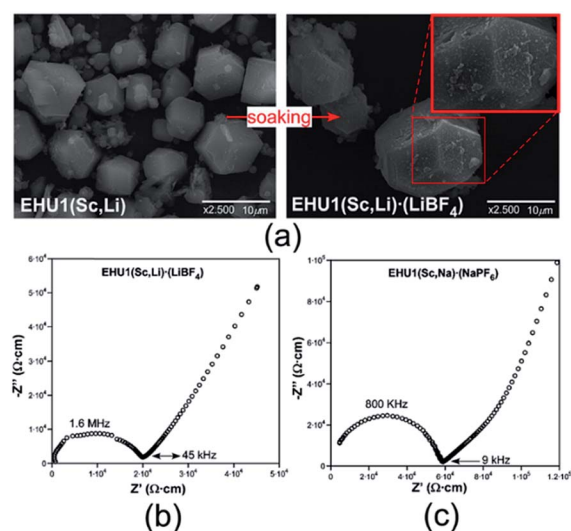


Fig. 34 (a) SEM images of **EHU1(Sc,Li)** before and after being immersed in LiBF_4 . (b and c) Nyquist plots of the ac impedance data for soaked **EHU1(Sc,M)** compounds. (Reprinted with permission from ref. 113, Copyright 2016, American Chemical Society.)

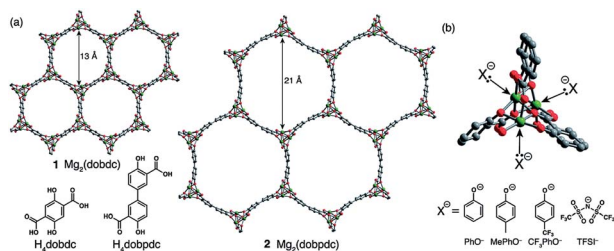


Fig. 35 (a) Structures of $\text{Mg}_2(\text{dobdc})$ and $\text{Mg}_2(\text{dobpdc})$ along the c direction, where 1D channels are constructed from magnesium-based chains and the respective ligands (bottom left). (b) Open coordination sites interacting with nucleophilic guest molecules: PhO^- , MePhO^- , CF_3PhO^- , and TFSI^- . (Reprinted with permission from ref. 126, Copyright 2014, Royal Society of Chemistry.)

coulombic interactions between the cationic skeleton and the ion (free Li^+ , free TFSI^- and the ion pairs $\text{Li}^+\text{-TFSI}^-$).

Jiang and co-workers designed and synthesized two types of COFs, **TPB-DMTP-COF** and **TPB-BMTP-COF**. Compared to **TPB-DMTP-COF**, **TPB-BMTP-COF** possessed oligo(ethylene oxide) chains extending along the direction of the channel.¹²¹ After immersing them in LiClO_4 solution, **Li@TPB-DMTP-COF** and **Li@TPB-BMTP-COF** were generated, and their ion conductivities were measured. The ion conductivities of **Li@TPB-DMTP-COF** were 1.36×10^{-7} , 6.74×10^{-7} , and $5.37 \times 10^{-6} \text{ S cm}^{-1}$ at 40 °C, 60 °C, and 80 °C, and the corresponding ion conductivities of **Li@TPB-BMTP-COF** were calculated to be 6.04×10^{-6} , 2.85×10^{-5} and $1.66 \times 10^{-4} \text{ S cm}^{-1}$, respectively, which were larger than that of **Li@TPB-DMTP-COF**. The highest ion conductivity was up to $5.49 \times 10^{-4} \text{ S cm}^{-1}$ at 90 °C. Compared to **Li@TPB-DMTP-COF**, the enhanced ion conductivity of **Li@TPB-BMTP-COF** may be attributed to the polyelectrolyte interface formed by dense oligo(ethylene oxide) chains and lithium ions, which created a transfer path for lithium ion movement.

2.3 Alkaline earth metal ion conductivity

To date, research about ionically conductive CPs has mainly focused on the transport of Li^+ cations, and naturally, a number of conducting CPs based on Li^+ ions have been discovered, as shown in the above section. Alkaline earth metal ions, for example, Mg^{2+} , have larger sizes and higher charge densities, making them difficult to move in the channels. Thus, it is very difficult to obtain materials with good conductivity. Some tentative work has been reported, but the performances are not very good.^{122–125}

Taking into account enough large channels and rich open metal sites, two analogues $\text{Mg}_2(\text{dobdc})$ and $\text{Mg}_2(\text{dobpdc})$ were used as platforms to construct a series of magnesium electrolytes.¹²⁶ By adjusting the type of magnesium phenolate ($\text{Mg}(\text{OPhMe})_2$, $\text{Mg}(\text{OPh})_2$ and $\text{Mg}(\text{OPhCF}_3)_2$ as well as $\text{Mg}(\text{TFSI})_2$, several corresponding composite materials were generated, defined as $\text{X}@\text{Mg}_2(\text{dobdc})$ or $\text{X}@\text{Mg}_2(\text{dobpdc})$ (X is single/two magnesium phenolates inside the framework) (Fig. 35). Among them, the ionic conductivities of the electrolytes doped with $\text{Mg}(\text{TFSI})_2$ and other magnesium phenolates displayed better performances than that of the composites doped with one type of magnesium salt alone.

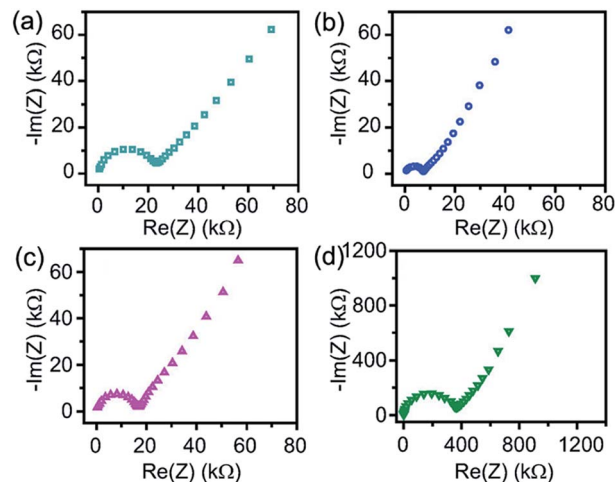


Fig. 36 Nyquist plots for (a) **MIT-20-LiCl**, (b) **MIT-20-LiBr**, (c) **MIT-20-Na**, and (d) **MIT-20-Mg**. (Reprinted with permission from ref. 127, Copyright 2017, American Chemical Society.)

Perhaps the existence of $\text{Mg}(\text{TFSI})_2$ in the electrolytes doped with mixed salts plays a major role in enhancing the ionic conductivity (greater than 0.1 mS cm^{-1}). The best proton conductivity of $\text{Mg}(\text{OPhCF}_3)_2 \cdot \text{Mg}(\text{TFSI})_2 @ \text{Mg}_2(\text{dobpdc})$ was up to 0.25 mS cm^{-1} at room temperature. Notably, the performance of the resulting materials was better than other magnesium electrolytes, which may act as electrolytes for practical applications in magnesium batteries.

A similar strategy was used to obtain new CP-based solid electrolytes. Solvothermal reaction gave birth to **MIT-20** by Dincă *et al.*, with the formula of $((\text{CH}_3)_2\text{NH}_2)[\text{Cu}_2\text{Cl}_3\text{BTDD}] \cdot (\text{DMF})_4(\text{H}_2\text{O})_{4.5}$.¹²⁷ By means of reversible single crystal to single crystal transition induced by halide or pseudohalide salts, a process of phase transformation occurred, where the phase of this framework changed from neutral to anionic. Then the framework could load a certain amount of Li^+ , Na^+ , and Mg^{2+} ions for charge-balancing (defined as **MIT-20-X**), which could move freely in its channels. After loading these metal ions, high ionic conductivity values of $4.4 \times 10^{-5} \text{ S cm}^{-1}$ for Li^+ , $1.8 \times 10^{-5} \text{ S cm}^{-1}$ for Na^+ , and $8.8 \times 10^{-7} \text{ S cm}^{-1}$ for Mg^{2+} were achieved (Fig. 36). Recently, the same group employed a Cu-azolate CP as the parent framework, where abundant open metal sites were occupied by halides, leading to an anionic framework (Fig. 37).¹²⁸ Considering the charge balance, Li^+ and Mg^{2+} diffused into the framework, defined as **MOF-MX_n** ($\text{M} = \text{Li}^+$ or Mg^{2+} , $\text{X} = \text{Cl}^-$, Br^- or I^- , and $n = 1$ or 2). Among them, **MOF-**

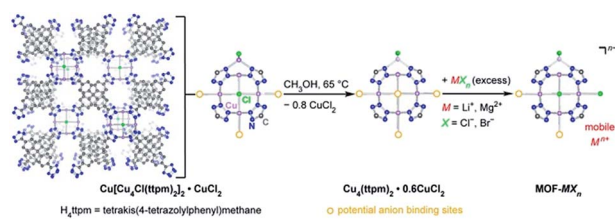


Fig. 37 Synthesis of Cu-azolate CP and the title **MOF-MX_n**. (Reprinted with permission from ref. 128, Copyright 2019, American Chemical Society.)

LiI showed the highest value ($1.1 \times 10^{-4} \text{ S cm}^{-1}$) at room temperature. Meanwhile, **MOF-MgBr₂** possessed a conductive value of $1.3 \times 10^{-4} \text{ S cm}^{-1}$, which to date, is in the upper level.

2.4. Other types of ion conductivity

Recently, ionic conducting materials have attracted increasing attention owing to their applications in electrochemical devices, for example, fuel cells and secondary batteries. To make better use of these devices in extreme environments (low temperature, *etc.*) and operate them more safely, ILs are employed to prepare conducting composite materials combined with CPs, and several achievements have been obtained.^{110,129–133}

Fujie's group made some contributions in this area.^{131,132} They incorporated [EMIM][TFSA] into the available space of ZIF-8, giving birth to [EMIM][TFSA]/ZIF-8, and investigated its ionic conductivity. The experimental results showed that [EMIM][TFSA]/ZIF-8 possessed higher ionic conductivity than the bulk [EMIM][TFSA] at low temperature because freezing of [EMIM][TFSA] was efficiently blocked after loading it into ZIF-8. An extensive work was subsequently directed by the same idea. A, Li⁺ ion-doped IL [EMIM]_{0.8}-Li_{0.2}[TFSA] was firstly prepared and introduced into ZIF-8, generating ELT@Z₁₀₀.¹¹⁰ However, its conductivity was lower than that of [EMIM][TFSA]/ZIF-8 at all loadings, revealing that Li⁺ ions hindered the ionic conductivity. This difference in ionic conductivity displays that the reasonable combination of CPs and ILs is very important to achieve good ionic conduction. In summary, IL-incorporated CPs may be promising solid electrolytes for electrochemical devices used at low temperatures.

3. CPs as electronic conductors

Electronic conductivity is important for designing and synthesizing new materials for electrochemical energy storage and conversion, and its research has become a hot research Frontier. Naturally, various electronic conductors have been prepared. The diversification of metal ions and organic linkers employed in the construction of CPs holds promise for applications in this field. However, the poor electrical conductivity of CPs limits their further applications in electrochemical energy storage and conversion. To date, various approaches have taken advantage of improving bulk electrical conductivity, involving (i) changing the metal-ion, for example, replacing Mn²⁺ with Fe²⁺; and (ii) employing redox ligands; (iii) doping with inorganic species (I₂) and/or organic species (TCNQ *etc.*). Among the conductive frameworks, 2D planar CPs resulting from multi-topic dithiolene and *o*-semiquinone aromatic organic linkers and transition metal ions can combine the advantages of both 2D inorganic (for example, layered metal chalcogenides) and organic materials (COFs *etc.*) have attracted considerable attention and are well-known. These 2D CPs possess narrow band gaps and desirable electrical conductivities. Obviously, the preparation and characterization of new 2D CPs can give birth to novel functional electronic materials. Several reviews have summarized the aspects of this type of CP in electrochemical energy storage and conversion.^{13,15–17,22,23} In this section, we mainly focus on the development of redox-active CPs or CPs incorporated with redox guest molecules in electronic conductivity in the past years (Table 3).^{129–166}

Table 3 List of selected electrically conductive CPs in this review

Name in the ref.	Guest molecule	Condition	Conductivity/S cm ⁻¹	Ref.
Ni _{0.6} Pt _{1.4} (EtCS ₂) ₄ I	—	400 K	1×10^{-4}	134
[Cu(HIN)I] _n	—	298 K	3×10^{-3}	135
Fe-BTC-Cr (1 : 1)	—	298 K	$\sim 10^{-3}$	136
Fe(tri) ₂ (BF ₄) _{0.33}	BF ₄ ⁻	298 K	0.3(1)	140
Cu-BHT	—	298 K	1580	141
Ag-BHT	—	300 K	250	142
Cu ₃ (HITP) ₂	—	298 K	0.2	143
Cu-CuPc	NH ₄ ⁺	353 K	1.6×10^{-6}	144
Cd ₂ (TFTB)	—	310 K	1.36×10^{-4}	145
[Pt ₂ (dta) ₄ I] _n	—	—	10 ⁴	147
[Cd(adc)(4-nvp) ₂ (H ₂ O)] _n	H ₂ O	—	3.91×10^{-3}	149
2,6-Naph(COOLi) ₂	—	333 K	10 ⁻⁵	151
Ni ₃ (HITP) ₂	—	298 K	40	152
Co ₃ (THT) ₂	—	300 K	3.2×10^{-2}	153
(NBu ₄) ₂ Fe ₂ ^{III} (dhbq) ₃	NBu ₄ ⁺	298 K	0.16 ± 0.01	157
1-Ti	H ₂ NMe ₂ ⁺	298 K and Ar atmosphere	$2.7(2) \times 10^{-3}$	158
2-V	H ₂ NMe ₂ ⁺	298 K and Ar atmosphere	0.45(3)	158
3-Cr	H ₂ NMe ₂ ⁺	298 K and Ar atmosphere	$1.2(1) \times 10^{-4}$	158
Fe ₂ (DSBDC)	DMF	297 K	3.9×10^{-6}	159
NiCuDTA	—	298 K	3.8×10^{-5}	160
[Cd(NDC) _{0.5} (PCA)]G _x > PPy	PPy	—	$\sim 10^{-1}$	161
Cu(TPyP)Cu ₂ (O ₂ CCH ₃) ₄	TCNQ	298 K	1.4×10^{-6}	162
Cu(TCNQ) film	—	298 K	$\sim 10^{-1}$	163
[Co _{1.5} (bdc) _{1.5} (H ₂ bpz)] · 0.5I ₂ · DMF	I ₂	298 K	1.56×10^{-6}	164
NU-100 doped with epoxy	Epoly	—	1.3×10^{-7}	166
NU-901 doped with fullerene	Fullerene	—	10 ⁻³	167
MIL-100(Cr)@PEDOT	PEDOT	—	1.1×10^{-3}	168

3.1 CPs with redox metal nodes

CPs with 1D chains are very common, but few of them are capable of possessing good electrical responses. Givaja and co-workers employed $[\text{Ni}_2(\text{EtCS}_2)_4]$ as the starting material to prepare three new heterobimetallic compounds, $[\text{Ni}_{0.6}\text{Pd}_{1.4}(\text{EtCS}_2)_4]$ (1), $[\text{NiPt}(\text{EtCS}_2)_4]$ (2), and $[\text{Pd}_{0.4}\text{Pt}_{1.6}(\text{EtCS}_2)_4]$ (3), through a transmetallation reaction process.¹³⁴ By means of iodine-directed partial oxidation, compound 2 gave birth to $[\text{Ni}_{0.6}\text{Pt}_{1.4}(\text{EtCS}_2)_4\text{I}]$ (4). The electrical conductivities of compounds 1–4 were measured, and their performance followed the order of $1 < 2 < 3 < 4$. Compound 4 displayed the best performance and its conductivity value could reach up to $1 \times 10^{-4} \text{ S cm}^{-1}$ at 400 K. This may be attributed to the fact that iodine atoms could bridge the heterodimetallic units and promote the delocalisation of the inter-dimer electrons to improve the conductivity. Cupric iodide cluster-based CPs with redox properties possesses inherent advantages in electronic conduction, as reported by Conesa-Egea *et al.* Two 1D CPs, $[\text{Cu}(\text{HIN})\text{I}]_n$ and $[\text{Cu}(\text{Cl-HIN})\text{I}]_n$, based on Cu(I)–I chains were synthesized.¹³⁵ These polymers are semiconductors. $[\text{Cu}(\text{HIN})\text{I}]_n$ is a copper(I) halide CP with the best electrical conductivity ($3 \times 10^{-3} \text{ S cm}^{-1}$) at room temperature. While, the presence of chlorine in $[\text{Cu}(\text{Cl-HIN})\text{I}]_n$ had a slight impact on the Cu–I chains, leading to a decrease in its electrical conductivity. In summary, the Cu–I skeletons are mainly responsible for the difference in their electrical conductivities, which was also demonstrated by theoretical calculations (Fig. 38a and b). The DFT calculations revealed that the density of states of $[\text{Cu}(\text{HIN})\text{I}]_n$ can promote electrical conduction process more effectively, and its electron valence band (VB) mainly distributes along the Cu–I skeleton, consistent with the experimental results (Fig. 38c).

Through a bimetallic design strategy, Dhara and co-workers developed mixed metal CPs to enhance the carrier mobility and electrical conductivity.¹³⁶ The bimetallic Fe-BTC-Cr system was used to evaluate the principle. Fe-BTC-Cr systems with different mole ratios (Fe/Cr = 2 : 1, 1 : 2 and 1 : 1) were developed. Among them, the Fe/Cr (1 : 1) bimetallic system showed the best performance, and an electrical conductivity value was obtained ($\sim 10^{-3} \text{ S cm}^{-1}$ at room temperature) (Fig. 39a) that was 10^2 and 10^4 times higher than that of Fe-BTC and Cr-BTC, respectively. The enhancement of electrical conductivity may be attributed to the narrow band gap between the VB and the conduction band (CB) in the presence of the p–n-type hybrid formed in the bimetallic CPs (Fig. 39b).

Dincă's group made important contributions in conductive CPs.^{132–134} Four types of CP families (twenty CPs based on eight different metal ions Mg^{2+} , Fe^{2+} , Mn^{2+} , Co^{2+} , Ni^{2+} , Cu^{2+} , Zn^{2+} and Cd^{2+} ions) were selected to measure their electrical conductivities (Fig. 40a).¹³⁷ Systematic measurements revealed that the iron-based CPs possessed the best electrical conductivities among the CP families, indicating iron could promote their electrical conductivity. The electronic structure and thermodynamic analysis revealed the following features of Fe^{2+} play a main role in the improvement of electrical conductivity: (i) the smallest ionization energy of Fe^{2+} ; (ii) the smaller standard

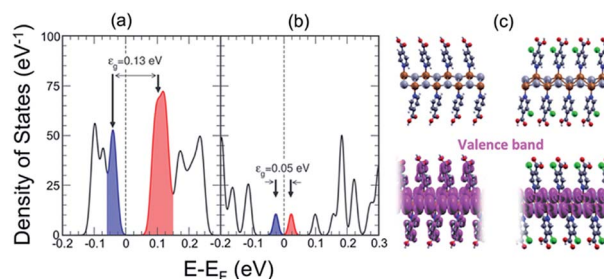


Fig. 38 Electronic state total densities (in eV^{-1}) of $[\text{Cu}(\text{HIN})\text{I}]_n$ (a) and $[\text{Cu}(\text{Cl-HIN})\text{I}]_n$ (b) with energies (in eV) relative to the Fermi level, which are broadened by the Lorentzian profile with a line width of 0.01 eV. The VB and CB of both compounds are marked in blue and red, respectively. (c) Computed 3D orbital of the VBs for $[\text{Cu}(\text{HIN})\text{I}]_n$ (left) and $[\text{Cu}(\text{Cl-HIN})\text{I}]_n$ (right). (Reprinted with permission from ref. 135, Copyright 2018, American Chemical Society.)

reduction potential (298 K) of the $\text{Fe}^{3+/2+}$ couple than that of the $\text{Mn}^{3+/2+}$, $\text{Co}^{3+/2+}$, and $\text{Cu}^{3+/2+}$ couples; (iii) the smallest Coulombic attraction of high-spin Fe^{2+} between its nucleus and valence and (iv) the synergistic role between mixed-valence $\text{Fe}^{3+/2+}$ system. This work deduced a general law that mixed-valence metal ions are beneficial for the electrical conductivity of CPs. This rule was demonstrated to be reasonable by Long's group again. They employed the poorly conductive iron(II) framework $\text{Fe}(\text{tri})_2$ as the reaction substrate, and a series of mixed-valence

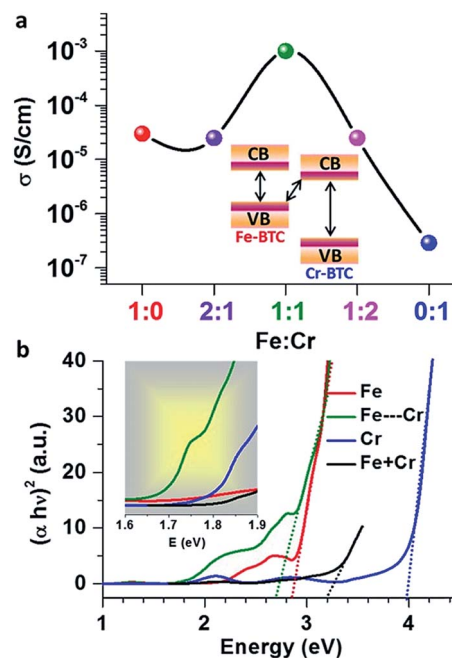


Fig. 39 (a) Conductive values from Fe-BTC (red), 2 : 1 Fe/Cr (violet), 1 : 1 Fe/Cr (green), 1 : 2 Fe/Cr (pink), and Cr-BTC (blue) at room temperature. Inset: possible mechanism of the narrow band gap in the bimetallic system. (b) UV-vis absorption spectra of Fe-BTC (red), Cr-BTC (blue), 1 : 1 Fe-BTC-Cr (green), and mixture (Fe-BTC + Cr-BTC) (black) at room temperature. Inset: new band at $\sim 1.75 \text{ eV}$ of the bimetallic system. (Reprinted with permission from ref. 136, Copyright 2017, American Chemical Society.)

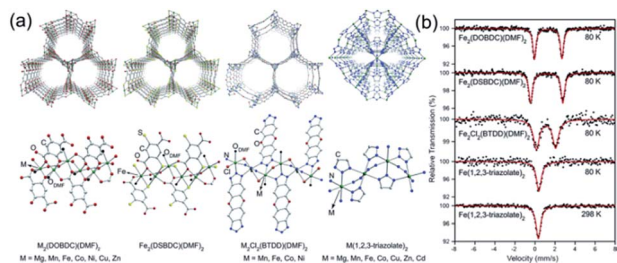


Fig. 40 (a) Channel and coordination geometry (top) and (bottom) of metal ions in four families of CPs. (b) Mössbauer spectra of $\text{Fe}_2(-\text{DOBDC})(\text{DMF})_2$, $\text{Fe}_2(\text{DSBDC})(\text{DMF})_2$, $\text{Fe}_2\text{Cl}_2(\text{BTDD})(\text{DMF})_2$ at 80 K, and $\text{Fe}(\text{1,2,3-triazolate})_2$ at 80 and 298 K under an N_2 atmosphere. Experimental data and Lorentzian fitting curves are marked by black dots and red curves, respectively. (Reprinted with permission from ref. 137, Copyright 2017, Royal Society of Chemistry and ref. 140, Copyright 2018, American Chemical Society.)

framework $\text{Fe}(\text{tri})_2(\text{BF}_4)_x$ ($x = 0.09, 0.22$ and 0.33) was obtained with the aid of the oxidation of thianthrenium tetrafluoroborate. $\text{Fe}(\text{tri})_2(\text{BF}_4)_{0.33}$ exhibited the highest value of (0.3 S cm^{-1}), which was 8 orders of magnitude higher than that of the parent material, and is one of the highest values among 3D CPs.¹⁴⁰ The results showed that with an increase in the iron oxidation level, the conductivity increased. Mössbauer spectroscopy indicated the existence of iron with a mixed valence state at 290 K (Fig. 40b), and various characterization methods revealed that intervalence charge transfer between mixed-valence iron centres can lead to high conductivity.

3.2 CPs with redox ligands

In conductive CPs, both metal nodes and organic linkers can act as charge carriers. More importantly, organic linkers possessing either stable radicals or redox active moieties have been used to maintain high charge delocalization through continuous conjugation with metal nodes. The electronic structure of conductive CPs can be modified by the selection of organic linkers. One method, involving organic ligands, electron donating or electron-withdrawing moieties can be employed to modulate the density and distribution of the charge. For example, amines bonded on organic linkers can increase the electron density. Another method is the employment of redox-active organic linkers with many accessible redox states, for example, HHTP or HITP.

Functional CPs as electronic conductors are rare because of the lack of CPs with high electrical conductivity. 2D CPs have drawn increasing attention, where the metal ions adopt a square-planar geometry, and multidentate ligands (for example, *o*-semiquinone and dithiolene) used in the synthetic process usually possess bidentate moieties and rich π - π interactions. Many examples have been reported.^{141–151}

In 2015, a crystalline film was prepared by Zhu *et al.* with the help of liquid interface reaction. A 2D CP was successfully synthesized, named **Cu-BHT** ($[\text{Cu}_3(\text{C}_6\text{S}_6)]_n$).¹⁴¹ Its structure was determined *via* PXRD and GIXRD analyses, and then quantum simulation confirmed this structure. The four-probe method

displayed that the electrical conductivity value is 1580 S cm^{-1} at room temperature, which is a high value among the reported CPs (Fig. 41). Subsequently, as a continuation of the previous work, this group made use of Ag and BHT to construct a crystalline film, namely **Ag-BHT**.¹⁴² Its formula was $[\text{Ag}_5(\text{C}_6\text{S}_6)]_n$, which was resolved through rotation electron diffraction and PXRD. It is a layered structure formed by the alternate stacking of 2D Ag-S networks. The **Ag-BHT** film exhibited high electrical conductivity (250 S cm^{-1} at 300 K).

Inspired by the excellent performance of the isostructural 2D CP $\text{Ni}_3(\text{HITP})_2$, and to systematically investigate the effect of the metal centre on the electronic properties in a family of isostructural CPs, a conductive 2D CP, $\text{Cu}_3(\text{HITP})_2$, was synthesized, which displayed an electrical conductivity of 0.2 S cm^{-1} .¹⁴³ Additionally, $\text{Cu}_3(\text{HITP})_2$ was employed to prepare a device. The electronic device based on $\text{Cu}_3(\text{HITP})_2$ was employed as a reversible sensor to detect ammonia vapour. This device was capable of detecting 5 ppm ammonia vapour under air with 60% RH (Fig. 42). In contrast, the device based on $\text{Ni}_3(\text{HITP})_2$ showed no obvious response to ammonia vapour under the same experimental conditions. The different experimental phenomenon may result from the change in the energies of the Fermi level influenced by metal ions.

A similar framework was discovered by Yanai and co-workers. They synthesized a 2D phthalocyanine-based CP $\text{Cu}_2(\text{CuPcOH})(\text{NH}_4)_{3.2}$ (**Cu-CuPc**) constructed from CuPcOH and copper(II) ions.¹⁴⁴ This 2D CP only showed an electrical

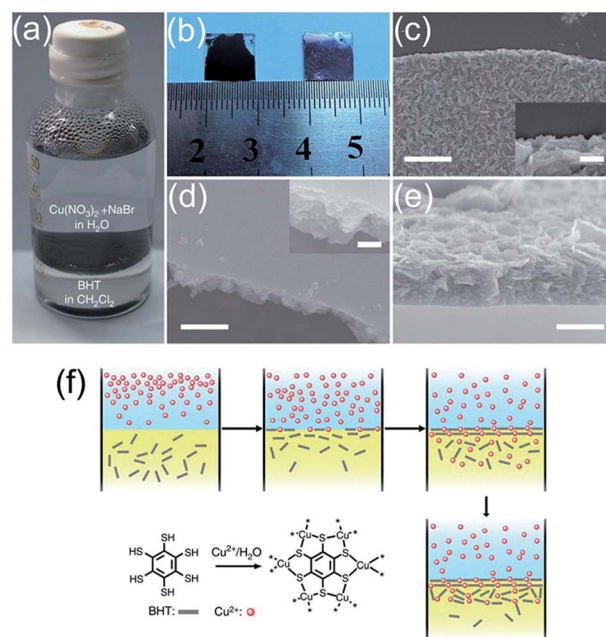


Fig. 41 (a) Images of the generated **Cu-BHT** film at the interface between CH_2Cl_2 and aqueous solution. (b) Images of the upside-up (right) and upside-down (left) films placed on glass substrates. SEM images of the upper surface (c), lower surface (d) and (e) cross-section of the film, and the inset image shows enlarged film edges. Scare bar, 200 nm (c), 400 nm (d and e) and 100 nm (inset). (f) Synthetic route for the **Cu-BHT** film. (Reprinted with permission from ref. 141, Copyright 2015, Nature.)

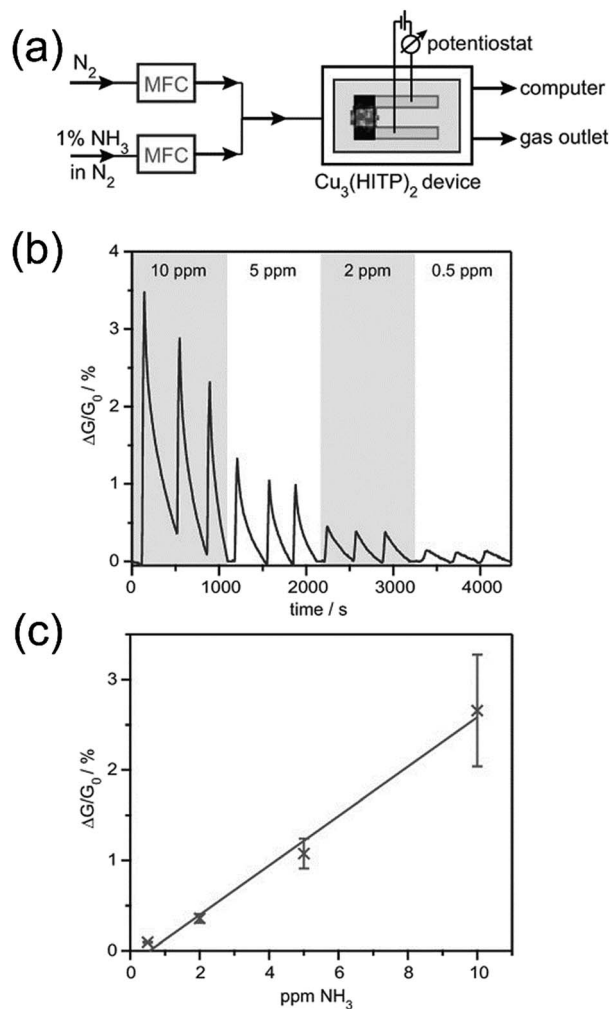


Fig. 42 (a) Schematic diagram of the experimental device; MFC = mass flow controller. (b) Signal responses of the Cu₃(HITP)₂ device corresponding to 0.5, 2, 5, and 10 ppm ammonia using nitrogen as a carrier. (c) Signal response as a function of ammonia concentration (R_2 value for linear fit: 0.99). (Reprinted with permission from ref. 143, Copyright 2015, Wiley-VCH.)

conductivity of $1.6 \times 10^{-6} \text{ S cm}^{-1}$ at 80 °C. It is possible that the anionic framework is unfavourable for the electron transfer. Besides, Cu-CuPc could act as a cathode in a lithium ion battery (LIB), and possessed large charge/discharge capacities of 151/128 mA h g⁻¹ and good cycle stability.

Employing the anisotropic CP Cd₂(TTFTB) as a representative example, several available methods were used to measure its electrical conductivity (Fig. 43).^{145,146} Evidently, factors such as atmosphere, temperature, metal source and illumination conditions have an impact on the data resulting from these techniques. Furthermore, the morphology of the samples, for example, single crystal (anisotropy) or pressed pellet, and the metal source also affect the observed conductivity. If these factors and the morphology and anisotropy of a single crystal are considered, consistent results can be obtained using different methods. Additionally, it should be mentioned that single-crystal measurements provided more reliable results,

and the best value was $1.36 \times 10^{-4} \text{ S cm}^{-1}$ at the temperature of 310 K in air and RH of 36–43%.

Among all the CPs, 1D CPs as an important component play a vital role in the emerging area of transparent and flexible electronics because of their specific electron migration direction. 1D platinum-based MMX CP [Pt₂(dta)₄I]_n with highly ordered structures and low defect content (0.4–1%) was studied, which exhibited a very high conductivity value (10^4 S m^{-1}) (Fig. 44a), which is generally higher than that of macroscopic crystals.¹⁴⁷ The experimental results revealed that the high anisotropy and very few defects exerted influence on the effective electrical conductivity (Fig. 44b). By taking advantage of the highly ordered structures, the prediction of gapless band structure of this material was demonstrated by experimental evidence first. In 2018, the same group found that the electrical conductivities measured in the experiments should be higher than that resulting from theoretical calculations.¹⁴⁸ Therefore, they developed a simple and convenient method “drop-casting”, and used it to isolate single MMX chains. Here, combined with their length, the experimental electrical resistances of several MMX chains disagreed with the predictions calculated from theoretical calculations. Theoretical modelling revealed that the differences originate from the structural defects, mainly focusing on the vacancies of iodine atoms, which hinder the flow of the current.

In 2017, a very ingenious approach was used to tune the electronic conductivity. An SC-SC transformation induced by UV irradiation was employed to improve the conductivity of the 1D double chain ladder CP [Cd(adc)(4-nvp)₂(H₂O)]_n.¹⁴⁹ Under UV irradiation, the SC-SC transformation occurred through a photochemical [2 + 2] cycloaddition reaction, and the 1D chain transformed into a 2D layered structure. This structural change resulted in a decrease in the distances between adjacent chains and enhanced $\pi \cdots \pi$ interactions, which resulted in an improvement in conductivity from $1.83 \times 10^{-3} \text{ S m}^{-1}$ to $3.91 \times 10^{-3} \text{ S m}^{-1}$.

The coordination geometry of the metal centres has an important influence on the performance of electrical conductivity. Musumeci *et al.* investigated how different coordination configurations affect conductive behaviors.¹⁵⁰ With the help of the self-assembly method, a terpyridine–anthracene–pyridine-based tecton (TAP), combined with Co(II) or Pd(II) cations was used to construct CPs (CoTAP)_n and (PdTAP)_n, respectively, which were successively deposited on the surface of SiO₂. Due to the different coordination geometries of the metal centres, thin films with different morphologies were generated. The planarity of square Pd(II) induced the generation of π – π stacked fibrillar structures, where the Pd–Pd and anthracene–anthracene wavefunction overlap could facilitate large electronic couplings between neighbouring chains. While the octahedral Co(II) led to insulating films, where the π – π stacking was obstructed, resulting in different electrical behaviours. Hence, the theoretical calculations revealed disappearing small hole and electron couplings lining the chains of (PdTAP)_n owing to the spatial localization of the Frontier crystal orbitals located in the Pd- or anthracene units. However, the inter-chain couplings were larger, which were mediated by Pd–Pd and anthracene–

anthracene couplings. The charge transport properties of (PdTAP)_n were promising in both the macroscopic and nano-scale state. A principle for designing conductive CPs was proposed by this research finding.

Furthermore, a layered structure, 2,6-naphthalene dicarboxylate dilithium 2,6-Naph(COOLi)₂, exhibited high electronic conductivity (10⁻⁵ S cm⁻¹ at 333 K) when intercalated by Li ions.¹⁵¹ However, this parent CP is an insulator in the pristine state. Theoretical calculation exhibited that when the band gap is 0.99 eV, an anisotropic electron hopping conduction pathway can be generated by Li intercalation induced electron transfer between the 2D π -stacking naphthalene layers. The electronic conductivity of the structure could be maintained up to 473 K, and then the intercalated CP turns into an insulator in the presence of the well-preserved structure at 673 K.

3.3 CPs with redox metal nodes and ligands

The electrical conductivity of CPs is determined by two components (metal centre and organic linkers), and can be designed by choosing specific components. Besides organic linkers, metal centres play an important role in their electrical conductivity. Systematic selection of the metal centre can tune the overall electronic structure, leading to excellent properties. Many examples have demonstrated that the selection of metal ions has a significant effect on the electrical conductivity response.

A new 2D CP, Ni₃(HITP)₂, was obtained. DFT data and PXRD and X-ray absorption fine structure (EXAFS) analysis were combined to define its final structure.¹⁵² The conductivity values of the bulk samples and films were determined to be 2 and 40 S cm⁻¹ *via* two-probe and van der Pauw electrical measurements at room temperature, respectively. It should be noted that the conductivity of the films exhibited a linear increase as the temperature increased from 77 to 450 K, which was reversible upon cooling, as shown in Fig. 45.

A very rare experimental phenomenon was observed by Clough *et al.* A 2D CP Co₃(THT)₂ based on THT with a temperature-dependent transition property was synthesized.¹⁵³ The temperature-dependent resistivity of both its pellet and films was systematically investigated (Fig. 46). For the pellet, the resistivity showed that the semiconducting phase (between 300 K and 173 K) turns into a metallic phase (below 130 K) upon a decrease in temperature. For the films, an analogous transition was found, and the transition was relative with the film thickness and the number of solvent molecules existing in the channels. DFT calculations supported the transition from a semiconducting phase to metallic phase, and predicted the highest mobility pathways existing between the sheets.

Depending on their good electrical conductivities, conductive 2D CPs have been employed as chemical sensors.^{153–156} Specially, Dincă *et al.* not only studied the electronic conductivity of CPs, but also prepared devices based on conductive CPs to sense volatile organic compounds (VOCs). A class of 2D CPs with analogous structures, Cu₃(HHTP)₂, Cu₃(HITP)₂, and Ni₃(HITP)₂, was selected and used to detect VOCs.¹⁵³ These CPs were employed as a cross-reactive sensor, which could precisely

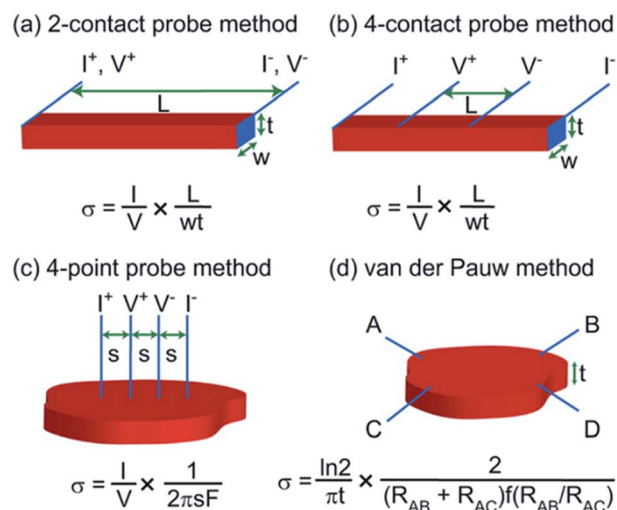


Fig. 43 Four kinds of approaches (a–d) red and blue fields represent samples and electrodes, respectively. *I*, current; *V*, voltage; *L*, sample length; *w*, sample width; *t*, sample thickness; *s*, distance between adjacent probes; σ , electrical conductivity; *F* and $f(R_{AB}/R_{AC})$, correction factors; +, input; –, output. (Reprinted with permission from ref. 145, Copyright 2016, American Chemical Society.)

identify different types of VOCs, indicating that this type of material may have unique applications in sensing. Through similar strategies, two other groups explored 2D conductive CPs to prepare chemiresistive sensors for the detection of gaseous analytes. One year later, two CPs (Cu₃HHTP₂ and Ni₃HHTP₂) were utilized to prepare chemiresistive sensors with polymeric films and graphitic electrodes.¹⁵⁵ The sensors could accurately analyse NH₃, NO, and H₂S at ppm concentrations. In 2017,

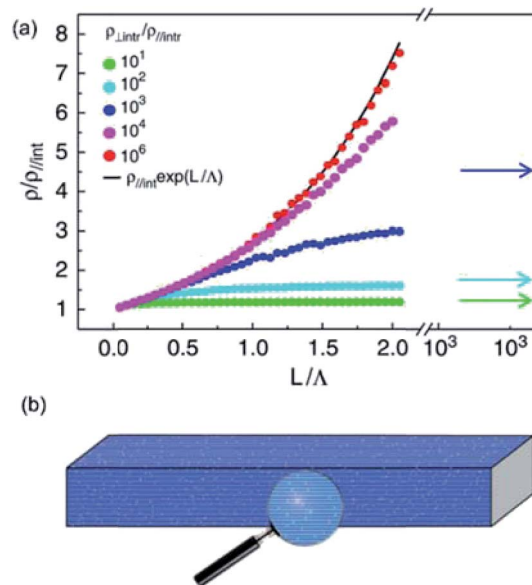


Fig. 44 (a) Standardized resistivity versus the sample length (in units of *L*) for different anisotropic values calculated using a 3D resistance model. (b) Random distributions of defects within the polymeric chains in an MMX crystal (lighter regions). (Reprinted with permission from ref. 147, Copyright 2013, Nature.)

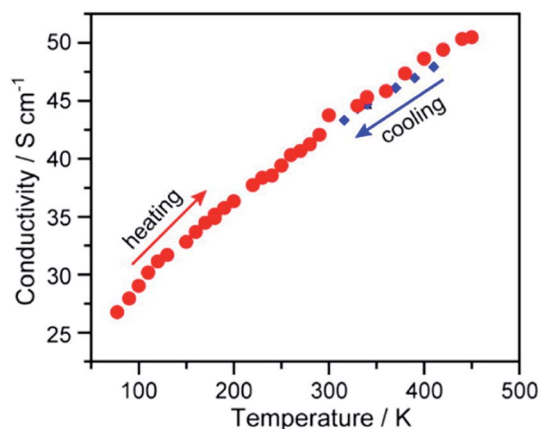


Fig. 45 van der Pauw conductivity values at different temperatures on a film with ~ 500 nm thickness on quartz. (Reprinted with permission from ref. 152, Copyright 2014, American Chemical Society.)

Mirica *et al.* integrated Ni_3HHTP_2 or Ni_3HITP_2 into electronic textiles to construct a chemiresistive sensor *via* the direct solution-phase self-assembly method.¹⁵⁶ The sensors could differentiate gaseous analytes, such as NO, H_2S , and H_2O at ppm levels, and maintain their sensing function in a humid

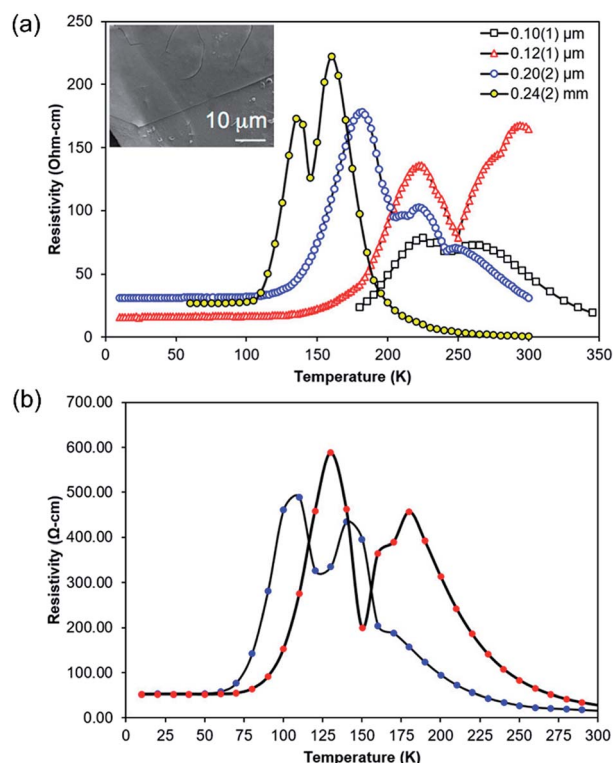


Fig. 46 (a) Resistivity data for the sample in the pellet state with 0.24(2) mm thickness (yellow, scaled down $10^5\times$) and films with 0.10(1) (black), 0.12(1) (red) and 0.20(2) (blue) μm thicknesses deposited on glass at various temperatures. Inset: SEM image of the film. (b) Resistivity data of the films with thicknesses of 0.5(1) μm before (blue) and after (red) 2 h under vacuum at 90 $^\circ\text{C}$. (Reprinted with permission from ref. 153, Copyright 2017, American Chemical Society.)

environment (5000 ppm, 18% RH). The theoretical limits of detection for NO and H_2S were 0.16 ppm and 0.23 ppm, respectively. Moreover, these sensors could capture and filter gaseous analytes.

Dhbq and its derivatives are well-known redox organic moieties and possess several valence states (Fig. 47a), and due to their advantages, they are widely employed. Long's group reported a 3D CP $(\text{NBu}_4)_2\text{Fe}_2^{\text{III}}(\text{dhbq})_3$ composed of Fe^{III} centres and a semiquinoid ligand. $(\text{NBu}_4)_2\text{Fe}_2^{\text{III}}(\text{dhbq})_3$ exhibited a conductivity value of $0.16 \pm 0.01 \text{ S cm}^{-1}$ at 298 K.¹⁵⁷ Many characterization techniques were employed to investigate the role of its component, which revealed that the mixed-valency ligand plays the key role in its electronic conductivity. The results of this work demonstrate that transition metal-semiquinoid systems may act as a promising platform for tunable electronic communication. Three years later, the same group further used dhbq and its derivatives to construct three CPs $(\text{H}_2\text{NMe}_2)_2\text{Ti}_2(\text{Cl}_2\text{dhbq})_3$ (**1-Ti**), $(\text{H}_2\text{NMe}_2)_2\text{V}_2(\text{Cl}_2\text{dhbq})_3$ (**2-V**) and $(\text{H}_2\text{NMe}_2)_{1.5}\text{Cr}_2(\text{dhbq})_3$ (**3-Cr**). The electronic conductivities of **1-Ti**, **2-V** and **3-Cr** were tested at room temperature and under an Ar atmosphere, which were calculated to be $2.7(2) \times 10^{-3}$, $0.45(3)$ and $1.2(1) \times 10^{-4} \text{ S cm}^{-1}$, respectively. The conductive behaviours of **1-Ti** and **3-Cr** were similar, but **2-V** displayed a different performance.¹⁵⁸ Experimental characterization and computational methods were combined to find the possible mechanism. The electronic behaviours of **1-Ti** and **3-Cr** may be ascribed to the redox-hopping between adjacent ligands with different valence states. While, the significant metal-ligand covalency of **2-V** results in its excellent performance (Fig. 47b).

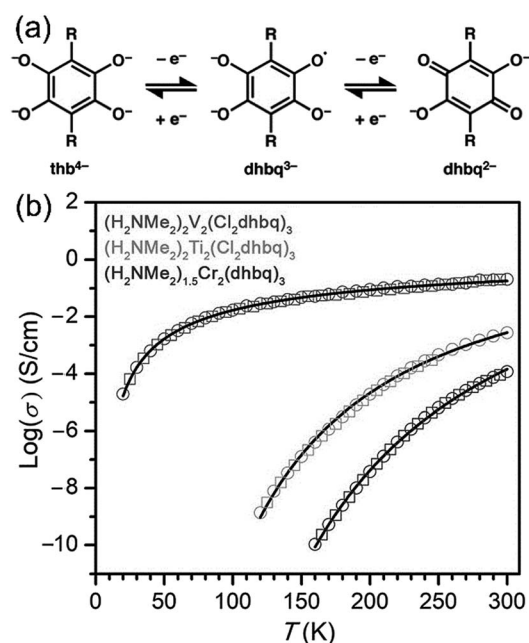


Fig. 47 (a) Different redox states of 2,5-dihydroxybenzoquinon. (b) Temperature-dependent conductivities of **1-Ti**, **2-V**, and **3-Cr**, respectively. Circles and squares represent cooling and warming data, respectively. (Reprinted with permission from ref. 157, Copyright 2015, American Chemical Society) and (Reprinted with permission from ref. 158, Copyright 2018, American Chemical Society.)

Four analogues of MOF-74 were synthesized by Dincă's group as follows: $\text{Fe}_2(\text{DSBDC})$, $\text{Fe}_2(\text{DOBDC})$, $\text{Mn}_2(\text{DSBDC})$ and $\text{Mn}_2(\text{DOBDC})$.¹⁵⁹ The electrical conductivity values of both $\text{Fe}_2(\text{DSBDC})$ and $\text{Fe}_2(\text{DOBDC})$ were $3.9 \times 10^{-6} \text{ S cm}^{-1}$ and $3.2 \times 10^{-7} \text{ S cm}^{-1}$, which were 6 orders of magnitude higher than that of $\text{Mn}_2(\text{DSBDC})$ and $\text{Mn}_2(\text{DOBDC})$ with values of $2.5 \times 10^{-12} \text{ S cm}^{-1}$ and $3.9 \times 10^{-13} \text{ S cm}^{-1}$, respectively. In addition, the better performance of $\text{Fe}_2(\text{DSBDC})$ may result from its loosely bound Fe^{2+} β -spin electrons and the low electronegativity of the S atoms, as supported by the differences in the electronic structures of $\text{M}_2(\text{DEBDC}) (\text{DMF})_2$ ($\text{E} = \text{O}$ or S) calculated from DFT calculations (Fig. 48).

In this contribution, a series of metal–organic gels (MOGs) based on $[\text{M}(\text{DTA})]_n$ (M^{II} : Ni, Cu and Pd) was reported.¹⁶⁰ After supercritical drying of these MOGs, metal–organic aerogels (MOAs) were generated and conductivity measurements were performed. The results showed that the MOAs possess semi-conducting behaviour (10^{-12} to $10^{-7} \text{ S cm}^{-1}$) at room temperature. When exposed to acetic acid vapour, the conductivity of MOAs increased, and reached up to $10^{-5} \text{ S cm}^{-1}$, demonstrating that the modification can improve their performance. Furthermore, cycling measurements of CuDTA and NiCuDTA were carried out at 4 h and 12 h intervals, respectively. The experimental results indicated that NiCuDTA needs a longer cycling time compared with that of CuDTA to gain comparable electrical conductivity.

3.4 CPs doped with a redox guest molecule

The poor overlap of orbitals between metal ions and organic linkers generally make CPs insulators. Thus, many redox-active guest molecules have been introduced into CPs to tune their poor state. Dhara *et al.* successfully intercalated pyrrole (Py) monomers into the channels of $[\text{Cd}(\text{NDC})_{0.5}(\text{PCA})] \cdot \text{Gx}$.¹⁶¹ With the help of I_2 , oxidative polymerization of the Py monomers in the channels occurred, giving birth to conducting polypyrrole (PPy) chains. Consequently, $[\text{Cd}(\text{NDC})_{0.5}(\text{PCA})] \cdot \text{Gx} \rightarrow \text{PPy}$ was generated. Both of them were evaluated for their electrical conductivity. For $[\text{Cd}(\text{NDC})_{0.5}(\text{PCA})] \cdot \text{Gx}$, the two-probe approach gave an electrical conductivity value of $\sim 10^{-12} \text{ S cm}^{-1}$, indicating it is an insulating material. For $[\text{Cd}(\text{NDC})_{0.5}(\text{PCA})] \cdot \text{Gx} \rightarrow \text{PPy}$, the two-probe, four-probe and Hall-effect measurements gave electrical conductivity values ranging from 10^{-1} to $10^{-3} \text{ S cm}^{-1}$. The sharp increase in conductivity may be attributed to the existence of highly oriented conducting PPy chains inside the 1D nanochannels and weak interactions between the host framework and guest molecules.

Moreover, a 2D $[\text{Cu}(\text{TPyP})\text{Cu}_2(\text{O}_2\text{CCH}_3)_4]$ (**Cu-CP**) film based on H_2TPyP was prepared.¹⁶² The 2D **Cu-CP** film doped with TCNQ exhibited an electrical conductivity value of $1 \times 10^{-4} \text{ S cm}^{-1}$, which was 3 orders of magnitude of that of the original **Cu-CP**. The charge transformation between TCNQ and the 2D **Cu-CP** plays an important role in the improvement of electrical conductivity. Recently, CP films have been widely studied and attracted attention from researchers for electrical conductivity. Here, Thürmer and co-workers reported that HKUST-1 (Cu_3BTC_2) became electrically conductive upon exposure to

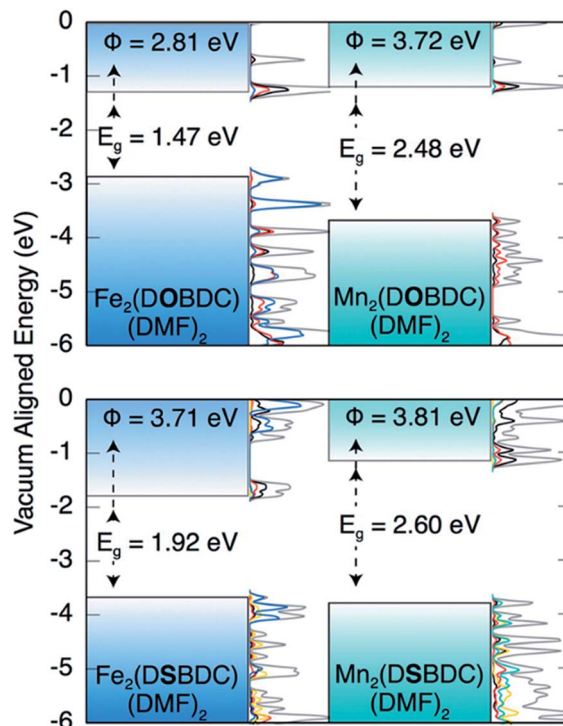


Fig. 48 Computed energy bands and calculated density of states (DOS) in $\text{M}_2(\text{DEBDC}) (\text{DMF})_2$ ($\text{M} = \text{Fe}, \text{Mn}$; $\text{E} = \text{S}, \text{O}$). Fe (Blue), Mn (teal), S (yellow), O (red), and C (black). (Reprinted with permission from ref. 159, Copyright 2015, American Chemical Society).

a TCNQ methanol solution, where a chemical reaction occurred when the HKUST-1 film was exposed to TCNQ methanol solution, and it was transformed into $\text{Cu}(\text{TCNQ})$ films completely.¹⁶³ This work is different from previous reported examples, where TCNQ is only loaded into the skeleton of the matrix. The surface morphology of the thin films changed from truncated octahedra to randomly ordered platelets (Fig. 49), indicating the occurrence of this chemical reaction. The generated $\text{Cu}(\text{TCNQ})$ film showed a conductivity value of $10^{-1} \text{ S cm}^{-1}$, 10 orders of magnitude higher than that of the parent HKUST-1 film.

The SC–SC transformation of $[\text{Co}_{1.5}(\text{bdc})_{1.5}(\text{H}_2\text{bpz})] \cdot \text{DMF} \cdot 4\text{H}_2\text{O}$ was induced by I_2 to give birth to $[\text{Co}_{1.5}(\text{bdc})_{1.5}(\text{H}_2\text{bpz})] \cdot 0.5\text{I}_2 \cdot \text{DMF}$.¹⁶⁴ The I_2 -loaded samples exhibited good electrical conductivities, which were three orders of magnitude higher than that of the pristine framework. I_2 inside the channels of the framework takes part in the $\text{C@H} \cdots \text{I}$ hydrogen

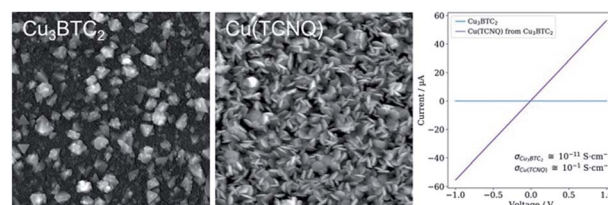


Fig. 49 Surface topography of Cu_3BTC_2 (left) and $\text{Cu}(\text{TCNQ})$ (middle) films on ITO substrate. Current–voltage plots of Cu_3BTC_2 and the generated $\text{Cu}(\text{TCNQ})$ films (right). (Reprinted with permission from ref. 163, Copyright 2018, American Chemical Society.)

bonds with phenyl units inside the framework, which play a vital role in improving electrical conductivity, and lead to $n-\sigma^*$ host-guest charge transfers to increase the electrical conductivity. Single-crystal X-ray diffraction determined the position of the I_2 guest molecules in the channels, confirming the existence of $C@H\cdots I$ hydrogen bonds. As is known, this is the first example that the mechanism of electrical conductivity is confirmed by single-crystal X-ray diffraction. Adopting the same strategy, Cao's group loaded I_2 into the framework of $[(Na_2I_2CB[6])\cdot 8H_2O]_n$, where the adsorbed I_2 molecules combined with isolated iodide ions, generating a polyiodide structure.¹⁶⁵ Owing to the existence of the polyiodide structure, the electrical conductivity value was $7.46 \times 10^{-7} \text{ S cm}^{-1}$ for the I_2 -loaded samples.

Porous zirconium-based CPs usually show excellent stability, which is favourable for their further modification. Hupp's group chose zirconium-based CPs with mesoporosity to construct a host-guest system.¹⁶⁶ A mesoporous zirconium-based CP, **NU-1000**, was chosen as the host to prepare a CP-polythiophene composite (Fig. 50). The pentathiophene derivative *p*-thio acid was firstly incorporated into the framework, which turned into a conductive composite *via* electrochemical polymerization. The prepared CP-polythiophene composite film could change from the insulating state to semiconducting state ($1.3 \times 10^{-7} \text{ S cm}^{-1}$) with an increase in the amount of polythiophene in the composite. Although polythiophene was immobilized into the channels, this composite still possessed large BET surface areas. One year later, **NU-901** constructed from zirconium clusters and similar linkers was employed as the container, and C_{60} was loaded into its diamond-shaped cavities, generating a composite with large available cavities.¹⁶⁷ In this composite, the linkers act as electron-donors, and fullerenes as electron-acceptors. The donor-acceptor interactions between the linkers and guests resulted in the observed electrical conductivity, which was supported by DFT calculations and the observation of visible-region charge-transfer band in the electronic absorption spectrum of the composite. The electrical conductivity of the thin film could reach up to $10^{-3} \text{ S cm}^{-1}$ after the incorporation of fullerene.

Through a two-step process, a composite material based on MIL-101(Cr) (**1**) and PEDOT was prepared *via* the oxidative effect of I_2 , which was defined as **1**⊃PEDOT.¹⁶⁸ The conductivity of **1**⊃PEDOT steadily improved following an increase of the

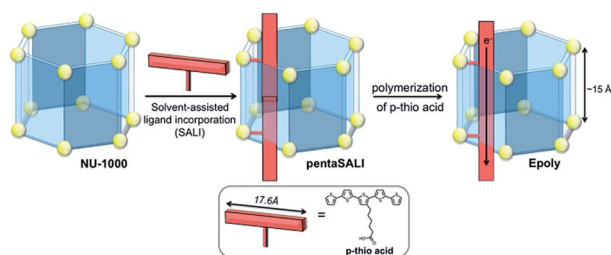


Fig. 50 Schematic diagram for the synthesis of the CP-polythiophene composite. (Reprinted with permission from ref. 166, Copyright 2017, American Chemical Society.)

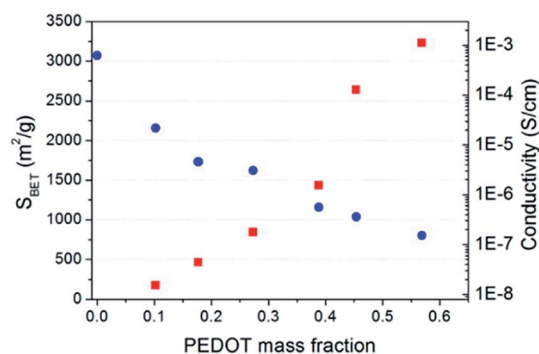


Fig. 51 Relation between conductivity (red squares) and specific surface area (blue circles) of **1**⊃PEDOT. (Reprinted with permission from ref. 168, Copyright 2016, American Chemical Society.)

amount of EDOT inside the framework; however, the porosity of the composite decreased (Fig. 51). The best electronic conductivity value was $1.1 \times 10^{-3} \text{ S cm}^{-1}$ with maintained high porosity. The Fermi level of PEDOT could be tuned by oxidizing analytes, leading to detectable signals of the conductivity. With the aid of this characteristic, **1**⊃PEDOT was explored as a chemiresistive sensor to detect the atmospheric pollutant NO_2 .

4. Summary and outlooks for ionic conductivity and electronic conductivity in CPs

In summary, herein, we summarized the latest research progress of CPs as ionic and electronic conductors. Diverse building units and design principles as well as various synthetic methods have enabled their great development in these fields. According to the outcomes, although many examples hold high promise for practical applications in electronic devices, such work is still in its infancy. To satisfy actual requirements, some remaining challenges need to be addressed. In the following sections, we present several perspectives and challenges.

4.1 CPs as ionic conductors

Intensive research has been continually conducted on solid electrolytes, focusing on their possible applications in energy storage and conversion devices. The crystalline and porous features of CPs provide excellent platforms in this field. The well-defined structure of CPs is favourable for establishing a clear relationship between their structure and property, which provides valuable suggestions and sheds light on the design parameters of solid electrolytes. Although most of the reported achievements about ion conductive CPs have focused on proton conduction, metal ion conduction for battery applications has also been extensively studied. However, some challenges still need to be addressed. In metal ion conductive CPs, the effect of loaded solvent molecules on ionic conductivity has not been assessed. Furthermore, if these materials are fabricated into electrode devices, risks caused by the solvent exist, which may

lead to serious safety problems. Thus, it is necessary for researchers to design and synthesize solvent-free solid electrolyte materials. Through investigating the reported literature, we propose two types of methods, one is introducing polymer chains into porous CPs to remove solvent molecules, and the other is to synthesize new nonporous CPs, which possess available space containing mobile metal ions, allowing their transport. However, the latter method is more challenging.

Of course, the stability of the emerging CP-based conductive materials is an important point, and must be considered in industrial applications. It should be mentioned that the stability required in electrochemical energy storage and conversion is different from that needed in gas storage, separation, *etc.* To the best of our knowledge, most electrical devices developed by scientists are operated at or near room temperature, and CPs can easily meet this requirement, even at a relatively high temperature. The stability of CPs in electrical devices can be evaluated prior to electrochemical tests, under simulated environment in electrochemical devices. From a practical point of view, promising materials must be measured many times to test and verify their durability in the long term. To date, chemists have made great efforts to improve the structural stability of CPs. Some principles have been proposed. For example, choosing metal ions in high valence states to construct nodes with high connectivity, as well as organic linkers with high pK_a values and steric hindrances yields CPs with high thermodynamic stability and kinetic stability.

4.2 CPs as electronic conductors

In the past years, numerous conductive CPs have been obtained, which provide more selections for new electronic components. The electronic properties of conductive CPs are mostly determined by their structural features. The electronic properties of inorganic materials, for example, graphene, are difficult to tune because they are not easily functionalized. Compared with inorganic materials, the electronic properties of CPs can be easily adjusted through various methods. Recently, planar, conjugated and redox active organic linkers and valence metal ions have been explored to synthesize new conducting 2D CPs, which may be a feasible choice for preparing new conductive materials for practical applications. It should be mentioned that introducing desirable guest molecules into the channels of 2D CPs may be a good approach for the synthesis of conductive materials with excellent properties. However, several scientific problems hinder their further applications. First, it is difficult to prepare ordered 2D CPs with desired structures in an ordered arrangement using available synthetic methods. Thus far, the single crystal structure of 2D CPs is hard to determine, and there is no method to solve this problem. Besides, their structure–property relationships are unclear due to the limited fundamental understanding of intrinsic CP structures and lack of knowledge about the host–guest interactions within CPs. This may need the help from computational modelling as well as spectroscopic characterizations. Furthermore, nowadays, the structures of designed and synthesized CPs have become increasingly complicated. Meanwhile, complicated structures

result in great challenges, and therefore, the fundamental relationship between their compositions/structures and conduction is hard to determine and well describe. Computer-aided theoretical calculation may be a useful tool, and has been extensively employed to predict the relationship between structures and conductions, which conversely promotes the synthesis of new materials. However, the complicated structures make it difficult for establishing theoretical models, and need higher requirements for computer simulations. Therefore, computer-aided theoretical calculation approaches will play more important roles in future studies.

Overall, the development of CP-based materials for electrochemical energy storage and conversion is still at the initial stage, and will become more and more active in the research field. Meanwhile, the industrial application of CP-based conductive materials still remains a huge challenge. Nevertheless, opportunities and challenges coexist. From the perspective of practical application, low cost and scalable synthesis may become two considerable points to be intensively investigated. After more than 20 years of development, many novel synthetic methods, such as electrochemical, microwave and mechanochemical syntheses have been used to prepare CPs, which provide a bright future for their low cost and scalable synthesis. To date, the scaled-up synthesis of CPs, for example, ZIF-8, has been realized. Thus, CP-based functional materials are slowly move from fundamental research to practical application, from laboratory synthesis to industrial production. As time develops, the wide applications of CP-based materials for practical applications will be realized.

Abbreviations

PEMFC	Proton exchange membrane fuel cells
IL	Ionic liquid
fdc	Furan dicarboxylate
btc	Benzene tri-carboxylate
btec	Benzene tetracarboxylate
TTFTB ^{4−}	Tetrathiafulvalenetetrabenzoate
L	1,2,4,5-Tetrakis(phosphonomethyl)benzene
H ₃ tzehp	<i>N</i> -[2-(1 <i>H</i> -Tetrazol-5-yl)ethyl]-L-hydroxyproline
1,4-BDMS	1,4-Benzene dimethanesulfonate
4,4'-bipy	4,4'-Bipyridine
H ₃ L	[1,1':3',1''-Terphenyl]-4,4'',5'-tricarboxylic acid
Dea	Diethylamine
NB	Nitrobenzene
DNB	1,4-Dinitrobenzene
py	Pyridine
tz	1 <i>H</i> -1,2,4-Triazole
H ₆ L	Benzene-1,3,5- <i>p</i> -phenylphosphonic acid
<i>m</i> -	2-(<i>m</i> -Chlorophenyl)imidazole-4,5-dicarboxylic acid
ClPhH ₃ IDC	
<i>p</i> -	2-(<i>p</i> -Chlorophenyl)imidazole-4,5-dicarboxylic acid
ClPhH ₃ IDC	
HSNDC ^{2−}	4-Sulfonaphthalene-2,6-dicarboxylate
H ₂ DCCPP	5,15-di(4-Carboxylphenyl)-10,20-di(4-pyridyl) porphyrin

<i>p</i> -IPhH ₃ IDC	2-(<i>p</i> - <i>N</i> -Imidazol-1-yl)-phenyl-1 <i>H</i> -imidazole-4,5-dicarboxylic acid	H ₂ NDC	2,6-Naphthalenedicarboxylic acid
H ₂ BDP	1,4-Bis(4-pyrazolyl)benzene	HPCA	4-Pyridinecarboxylic acid
bdc	Terephthalic acid	G	Guest molecules
STA	2-Sulfoterephthalic acid	TCNQ	7,7,8,8-Tetracyanoquinodimethane
EN	Ethylenediamine	H ₂ TPyP	5,10,15,20-Tetra-4-pyridyl-21 <i>H</i> ,23 <i>H</i> -porphine
DETA	Diethylenetriamine	H ₂ bpz	3,3',5,5'-Tetramethyl-4,4'-bipyrazole
TETA	Triethylenetetramine;	EDOT	3,4-Ethylenedioxythiophene
TEPA	Tetraethylenepentamine	H ₄ L ¹	Biphenyl-4,4'-diphosphonic acid
Pz	1 <i>H</i> -Pyrazole	H ₄ L	4,4',4'',4'''-(1,4-Phenylenebis(pyridine-4,2,6-triyl))-tetrabenzoic acid
SA	Sulfate acid	H ₃ MIDC	2-Methyl-1 <i>H</i> -imidazole-4,5-dicarboxylic acid
MSA	Methanesulfonate acid	H ₂ SNDC	4,8-Disulfonaphthalene-2,6-dicarboxylate
PTSA	<i>p</i> -Toluenesulfonate acid	POM	Polyoxometalate
EIMS	1-(1-Ethyl-3-imidazolium)propane-3-sulfonate;	2,6-PDC	2,6-NC ₅ H ₃ (CO ₂ H) ₂
F ₂ AzoBDC	(<i>E</i>)-2-((2,6-Difluorophenyl)diazanyl)terephthalic acid	BHT	Benzenehexathiol
dabco	1,4-Diazabicyclo[2.2.2]octane	dhbq ^{2-/3-}	2,5-Dioxidobenzoquinone/1,2-dioxi-do-4,5-semiquinone
PEEK	Poly(ether ether ketone)	Cl ₂ dhbq ⁿ⁻	2,5-Dichloro-3,6-dihydroxybenzoquinone
Tp	Terephthalate	CB[6]	Cucurbit[6]uril
PyOH	4-Pyridinol	MeIm	1-Methylimidazolium
Phytic acid	Inositol hexaphosphoric ligand	[EMIM]	(1-Ethyl-3-methylimidazolium
PVA	Poly(vinyl alcohol);	[TFSA]	bis(trifluoromethylsulfonyl)amide)
NMP	<i>N</i> -Methyl-2-pyrrolidone	TBA	Tetrabutylammonium
dobdc ⁴⁻	1,4-Dioxido-2,5-benzenedicarboxylate		
EC	Ethylene carbonate;		
DEC	Diethyl carbonate		
EMI-TFSA	1-Ethyl-3-methylimidazolium bis(trifluoromethylsulfonyl)-amide		
LiTFSA	(Lithium bis(trifluoromethylsulfonyl)amide)		
dobpdc	4,40-Dioxidobiphenyl-3,30-dicarboxylate		
PhO ⁻	Phenolate		
MePhO ⁻	4-Methylphenolate		
CF ₃ PhO ⁻	4-Trifluoromethylphenolate		
TFSI ⁻	Bis(trifluoromethanesulfonyl)imide		
BTDD ²⁻	Bis(1 <i>H</i> -1,2,3-triazolo[4,5- <i>b</i>],[4',5'- <i>i</i>])dibenzo-[1,4]dioxin		
TPB	1,3,5-Tri(4-aminophenyl)benzene		
DMTP	2,5-Dimethoxyterephthalaldehyde		
BMTP	2,5-Bis((2-methoxyethoxy)methoxy)terephthalaldehyde		
pmdc	Pyrimidine-4,6-Dicarboxylate		
HIN	Isonicotinic acid		
Cl-HIN	3-Chloroisonicotinic acid		
tri ⁻	1,2,3-Triazole		
HITP	2,3,6,7,10,11-Hexaiminotriphenylene		
dta	Dithioacetato		
TAP	4'-[10-[2-(4-Pyridinyl)ethynyl]-9-anthracenyl]-2,2':6',2''-terpyridine		
TTFTB ⁴⁻	Tetrathia-fulvalene tetrabenzoate;		
CuPcOH	Copper(II) 2,3,9,10,16,17,23,24-octahydroxy-29 <i>H</i> ,31 <i>H</i> -phthalocyanine		
H ₂ adc	Acetylenedicarboxylic acid		
4-nvp	4-(1-Naphthylvinyl)pyridine		
HITP	2,3,6,7,10,11-Hexaaminotriphenylene		
DSBDC ⁴⁻	2,5-Disulphydrylbenzene-1,4-dicarboxylic acid		
DOBDC ⁴⁻	2,5-Dihydroxybenzene-1,4-dicarboxylate		
THT	2,3,6,7,10,11-Triphenylenehexathiolate		
DTA	Dithiooxamidato		
HHTP	2,3,6,7,10,11-Hexahydroxytriphenylene		

Conflicts of interest

There are no conflicts to declare.

Acknowledgements

This work was financially supported by NSFC (No. 21601109, 21622104, 21701085, 21871141, 21871142 and 20901122); the NSF of Jiangsu Province of China (No. BK20171032); the Natural Science Research of Jiangsu Higher Education Institutions of China (No. 17KJB150025 and 19KJB150011); Priority Academic Program Development of Jiangsu Higher Education Institutions and the Foundation of Jiangsu Collaborative Innovation Center of Biomedical Functional Materials, the China Postdoctoral Science Foundation (No. 2018M632328 and 2019M651873).

Notes and references

- O. M. Yaghi, H. L. Li, C. Davis, D. Richardson and T. L. Groy, *Acc. Chem. Res.*, 1998, **31**, 474–484.
- B. Moulton and M. J. Zaworotko, *Chem. Rev.*, 2001, **101**, 1629–1658.
- D. J. Tranchemontagne, J. L. Mendoza-Cortés, M. O'Keeffe and O. M. Yaghi, *Chem. Soc. Rev.*, 2009, **38**, 1257–1283.
- X. H. Cao, C. L. Tan, M. Sindoro and H. Zhang, *Chem. Soc. Rev.*, 2017, **46**, 2660–2677.
- J. Liu and J. C. Wöll, *Chem. Soc. Rev.*, 2017, **46**, 5730–5770.
- J. Zhou and B. Wang, *Chem. Soc. Rev.*, 2017, **46**, 6927–6945.
- D. Y. Du, J. S. Qin, S. L. Li, Z. M. Su and Y. Q. Lan, *Chem. Soc. Rev.*, 2014, **43**, 4615–4632.

- 8 N. S. Bobbitt, M. L. Mendonca, A. J. Howarth, T. Islamoglu, J. T. Hupp, O. K. Farha and R. Q. Snurr, *Chem. Soc. Rev.*, 2017, **46**, 3357–3385.
- 9 X. Lian, Y. Fang, E. Joseph, Q. Wang, J. Li, S. Banerjee, C. Lollar, X. Wang and H. C. Zhou, *Chem. Soc. Rev.*, 2017, **46**, 3386–3401.
- 10 S. M. J. Rogge, A. Bavykina, J. Hajek, H. Garcia, A. I. Olivoso-Suarez, A. Sepúlveda-Escribano, A. Vimont, G. Clet, P. Bazin, F. Kapteijn, M. Daturi, E. V. Ramos-Fernandez, F. X. L. Xamena, V. V. Speybroeck and J. Gascon, *Chem. Soc. Rev.*, 2017, **46**, 3134–3184.
- 11 W. P. Lustig, W. S. Mukherjee, N. D. Rudd, A. V. Desai, J. Li and S. K. Ghosh, *Chem. Soc. Rev.*, 2017, **46**, 3242–3285.
- 12 K. Fujie and H. Kitagawa, *Coord. Chem. Rev.*, 2016, **370**, 382–390.
- 13 D. W. Lim, M. Sadakiyo and H. Kitagawa, *Chem. Sci.*, 2019, **10**, 16–23.
- 14 I. Stassen, N. Burtch, A. Talin, P. Falcaro, M. Allendorf and R. Ameloot, *Chem. Soc. Rev.*, 2017, **46**, 3185–3241.
- 15 L. Sun, M. G. Campbell and M. Dincă, *Angew. Chem., Int. Ed.*, 2016, **55**, 3566–3579.
- 16 M. Ko, L. Mendecki and K. A. Mirica, *Chem. Soc. Rev.*, 2012, **41**, 115–147.
- 17 C. F. Leong, P. M. Usov and D. M. D'Alessandro, *MRS Bull.*, 2016, **41**, 858–864.
- 18 X. Meng, H. N. Wang, S. Y. Song and H. J. Zhang, *Chem. Soc. Rev.*, 2017, **46**, 464–480.
- 19 M. Ko, L. Mendecki and K. A. Mirica, *Chem. Commun.*, 2018, **54**, 7873–7891.
- 20 A. L. Li, Q. Gao, J. Xu and X. H. Bu, *Coord. Chem. Rev.*, 2017, **344**, 54–82.
- 21 Y. Zhang, S. N. Riduan and J. Wang, *Chem.–Eur. J.*, 2017, **23**, 16419–16431.
- 22 L. Wang, Y. Han, X. Feng, J. Zhou, P. Qi and B. Wang, *Coord. Chem. Rev.*, 2016, **307**, 361–381.
- 23 W. Xia, A. Mahmood, R. Zou and Q. Xu, *Energy Environ. Sci.*, 2015, **8**, 1837–1866.
- 24 S. Chand, W. H. Deng, A. Pal and M. C. Das, *Angew. Chem., Int. Ed.*, 2018, **57**, 6662–6666.
- 25 S. S. Park, A. J. Rieth, C. H. Hendon and M. Dincă, *J. Am. Chem. Soc.*, 2018, **140**, 2016–2019.
- 26 N. E. Wong, P. Ramaswamy, A. S. Lee, B. S. Gelfand, K. J. Bladec, J. M. Taylor, D. M. Spasyuk and G. K. H. Shimizu, *J. Am. Chem. Soc.*, 2017, **139**, 14676–14683.
- 27 K. Zhang, X. J. Xie, H. Y. Li, J. X. Gao, L. Nie, Y. Pan, J. Xie, D. Tian, W. L. Liu, Q. L. Fan, H. Q. Su, L. Huang and W. Huang, *Adv. Mater.*, 2017, **29**, 1701804.
- 28 R. Li, S. H. Wang, X. X. Chen, J. Lu, Z. H. Fu, Y. Li, G. Xu, F. K. Zheng and G. C. Guo, *Chem. Mater.*, 2017, **29**, 2321–2331.
- 29 G. Y. Zhang and H. H. Fei, *Chem. Commun.*, 2017, **53**, 4156–4159.
- 30 X. Wang, Y. L. Wang, M. A. Silver, D. X. Gui, Z. L. Bai, Y. X. Wang, W. Liu, L. H. Chen, J. Diwu, Z. F. Chai and S. Wang, *Chem. Commun.*, 2018, **54**, 4429–4432.
- 31 P. G. M. Mileo, K. Adil, L. Davis, A. Cadiau, Y. Belmabkhout, H. Aggarwal, G. Maurin, M. Eddaoudi and S. Devautour-Vinot, *J. Am. Chem. Soc.*, 2018, **140**, 13156–13160.
- 32 L. Z. Liu, Z. Z. Yao, Y. X. Ye, Q. J. Lin, S. M. Chen, Z. J. Zhang and S. C. Xiang, *Cryst. Growth Des.*, 2018, **18**, 3724–3728.
- 33 S. Pili, S. P. Argent, C. G. Morris, P. Rought, V. García-Sakai, I. P. Silverwood, T. L. Easun, M. Li, M. R. Warren, C. A. Murray, C. C. Tang, S. H. Yang and M. Schröder, *J. Am. Chem. Soc.*, 2016, **138**, 6352–6355.
- 34 P. Rought, C. Marsh, S. Pili, I. P. Silverwood, V. G. Sakai, M. Li, M. S. Brown, S. P. Argent, I. Vitorica-Yrezabal and G. Whitehead, *Chem. Sci.*, 2019, **10**, 1492–1499.
- 35 S. Pili, P. Rought, D. I. Kolokolov, L. F. Lin, I. da Silva, Y. Q. Chen, C. Marsh, I. P. Silverwood, V. G. Sakai and M. Li, *Chem. Mater.*, 2018, **30**, 7593–7602.
- 36 F. M. Zhang, L. Z. Dong, J. S. Qin, W. Guan, J. Liu, S. L. Li, M. Lu, Y. Q. Lan, Z. M. Su and H. C. Zhou, *J. Am. Chem. Soc.*, 2017, **139**, 6183–6189.
- 37 Y. X. Ye, W. G. Guo, L. H. Wang, Z. Y. Li, Z. J. Song, J. Chen, Z. J. Zhang, S. C. Xiang and B. L. Chen, *J. Am. Chem. Soc.*, 2017, **139**, 15604–15607.
- 38 H. B. Luo, Q. Ren, P. Wang, J. Zhang, L. F. Wang and X. M. Ren, *ACS Appl. Mater. Interfaces*, 2019, **11**, 9164–9171.
- 39 Y. Guo, Z. Q. Jiang, W. Ying, L. P. Chen, Y. Z. Liu, X. B. Wang, Z. J. Jiang, B. L. Chen and X. S. Peng, *Adv. Mater.*, 2017, **29**, 1705155.
- 40 S. Khatua, A. K. Bar and S. Konar, *Chem.–Eur. J.*, 2016, **22**, 16277–16285.
- 41 S. Khatua, A. K. Bar, J. A. Sheikh, A. Clearfield and S. Konar, *Chem.–Eur. J.*, 2018, **24**, 872–880.
- 42 B. Joarder, J. B. Lin, Z. Romero and G. K. H. Shimizu, *J. Am. Chem. Soc.*, 2017, **139**, 7176–7179.
- 43 W. Y. Chen, J. Wang, L. L. Zhao, W. Dai, Z. F. Li and G. Li, *J. Alloys Compd.*, 2018, **750**, 895–901.
- 44 X. Liang, B. Li, M. H. Wang, J. Wang, R. L. Liu and G. Li, *ACS Appl. Mater. Interfaces*, 2017, **9**, 25082–25086.
- 45 Z. B. Sun, S. H. Yu, L. L. Zhao, J. F. Wang, Z. F. Li and G. Li, *Chem.–Eur. J.*, 2018, **24**, 10829–10839.
- 46 R. L. Liu, Y. R. Liu, S. H. Yu, C. L. Yang, Z. F. Li and G. Li, *ACS Appl. Mater. Interfaces*, 2019, **11**, 1713–1722.
- 47 X. M. Li, L. Z. Dong, S. L. Li, G. Xu, J. Liu, F. M. Zhang, L. S. Lu and Y. Q. Lan, *ACS Energy Lett.*, 2017, **2**, 2313–2318.
- 48 X. Y. Lai, Y. W. Liu, G. C. Yang, S. M. Liu, Z. Shi, Y. Lu, F. Luo and S. X. Liu, *J. Mater. Chem. A*, 2017, **5**, 9611–9617.
- 49 S. R. Kim, B. Joarder, J. A. Hurd, J. F. Zhang, K. W. Dawson, B. S. Gelfand, N. E. Wong and G. K. H. Shimizu, *J. Am. Chem. Soc.*, 2018, **140**, 1077–1082.
- 50 S. Shalini, V. M. Dhavale, K. M. Eldho, S. Kurungot and T. G. A. R. Vaidhyanathan, *Sci. Rep.*, 2016, **6**, 32489.
- 51 T. H. N. Lo, M. V. Nguyen and T. N. Tu, *Inorg. Chem. Front.*, 2017, **4**, 1509–1516.
- 52 M. V. Nguyen, T. H. N. Lo, L. C. Luu, H. T. T. Nguyen and T. N. Tu, *J. Mater. Chem. A*, 2018, **6**, 1816–1821.
- 53 S. Shalini, S. Aggarwal, S. K. Singh, M. Dutt, T. G. Ajithkumar and R. Vaidhyanathan, *Eur. J. Inorg. Chem.*, 2016, **27**, 4382–4386.

- 54 F. Yang, G. Xu, Y. B. Dou, B. Wang, H. Zhang, H. Wu, W. Zhou, J. R. Li and B. L. Chen, *Nat. Energy*, 2017, **2**, 877–883.
- 55 H. Wu, F. Yang, X. L. Lv, B. Wang, Y. Z. Zhang, M. J. Zhao and J. R. Li, *J. Mater. Chem. A*, 2017, **5**, 14525–14529.
- 56 T. He, Y. Z. Zhang, H. Wu, X. J. Kong, X. M. Liu, L. H. Xie, Y. B. Dou and J. R. Li, *ChemPhysChem*, 2017, **18**, 3245–3252.
- 57 D. D. Borges, S. Devautour-Vinot, H. Jobic, J. Ollivier, F. Nouar, R. Semino, T. Devic, C. Serre, F. Paesani and G. Maurin, *Angew. Chem., Int. Ed.*, 2016, **55**, 3919–3924.
- 58 H. Chen, S. Y. Han, R. H. Liu, T. F. Chen, K. L. Bi, J. B. Liang, Y. H. Deng and C. Q. Wan, *J. Power Sources*, 2018, **376**, 168–176.
- 59 K. Müller, J. Helfferich, F. L. Zhao, R. Verma, A. B. Kanj, V. Meded, D. Bléger, W. Wenzel and L. Heinke, *Adv. Mater.*, 2018, **30**, 1706551.
- 60 X. Y. Dong, J. J. Li, Z. Han, P. G. Duan, L. K. Li and S. Q. Zang, *J. Mater. Chem. A*, 2017, **5**, 3464–3474.
- 61 Z. Li, W. Y. Wang, Y. J. Chen, C. Y. Xiong, G. W. He, Y. Cao, H. Wu, M. D. Guiverac and Z. Y. Jiang, *J. Mater. Chem. A*, 2016, **4**, 2340–2348.
- 62 X. Y. He, M. Y. Gang, Z. Li, G. W. He, Y. H. Yin, L. Cao, B. Zhang, H. Wu and Z. Y. Jiang, *Sci. Bull.*, 2017, **62**, 266–276.
- 63 H. A. Patel, N. Mansor, S. Gadipelli, D. J. L. Brett and Z. X. Guo, *ACS Appl. Mater. Interfaces*, 2016, **8**, 30687–30691.
- 64 Z. Rao, B. B. Tang and P. Y. Wu, *ACS Appl. Mater. Interfaces*, 2017, **9**, 22597–22603.
- 65 Z. Rao, K. Feng, B. B. Tang and P. Y. Wu, *J. Membr. Sci.*, 2017, **533**, 160–170.
- 66 H. Z. Sun, B. B. Tang and P. Y. Wu, *ACS Appl. Mater. Interfaces*, 2017, **9**, 26077–26087.
- 67 H. Z. Sun, B. B. Tang and P. Y. Wu, *ACS Appl. Mater. Interfaces*, 2017, **9**, 35075–35085.
- 68 A. Donnadio, R. Narducci, M. Casciola, F. Marmottini, R. D'Amato, M. Jazestani, H. Chiniforoshan and F. Costantino, *ACS Appl. Mater. Interfaces*, 2017, **9**, 42239–42246.
- 69 J. Zhang, H. J. Bai, Q. Ren, H. B. Luo, X. M. Ren, Z. F. Tian and S. F. Lu, *ACS Appl. Mater. Interfaces*, 2018, **10**, 28656–28663.
- 70 K. Cai, F. Sun, X. Q. Liang, C. Liu, N. Zhao, X. Q. Zou and G. S. Zhu, *J. Mater. Chem. A*, 2017, **5**, 12943–12950.
- 71 X. Meng, M. J. Wei, H. N. Wang, H. Y. Zang and Z. Y. Zhou, *Dalton Trans.*, 2018, **47**, 1383–1387.
- 72 X. Meng, H. N. Wang, X. K. Wang, L. Z. Dong and Y. H. Zou, *New J. Chem.*, 2019, **43**, 24–27.
- 73 X. Meng, H. N. Wang, L. S. Wang, Y. H. Zou and Z. Y. Zhou, *CrystEngComm*, 2019, **21**, 3146–3150.
- 74 J. X. Wang, Y. D. Wang, M. J. Wei, H. Q. Tan, Y. H. Wang, H. Y. Zang and Y. G. Li, *Inorg. Chem. Front.*, 2018, **5**, 1213–1217.
- 75 Z. Li, L. D. Lin, H. Yu, X. X. Li and S. T. Zheng, *Angew. Chem., Int. Ed.*, 2018, **57**, 15777–15781.
- 76 P. Yang, M. Alsufyani, A. H. Emwas, C. Q. Chen and N. M. Khashab, *Angew. Chem., Int. Ed.*, 2018, **57**, 13046–13051.
- 77 W. J. Liu, L. Z. Dong, R. H. Li, Y. J. Chen, S. N. Sun, S. L. Li and Y. Q. Lan, *ACS Appl. Mater. Interfaces*, 2019, **11**, 7030–7036.
- 78 X. L. Cao, S. L. Xie, S. L. Li, L. Z. Dong, J. Liu, X. X. Liu, W. B. Wang, Z. M. Su, W. Guan and Y. Q. Lan, *Chem.–Eur. J.*, 2018, **24**, 2365–2369.
- 79 H. B. Luo, L. T. Ren, W. H. Ning, S. X. Liu, J. L. Liu and X. M. Ren, *Adv. Mater.*, 2016, **28**, 1663–1667.
- 80 H. B. Luo, M. Wang, J. Zhang, Z. F. Tian, Y. Zou and X. M. Ren, *ACS Appl. Mater. Interfaces*, 2018, **10**, 2619–2627.
- 81 S. Biswas, J. Chakraborty, V. S. Parmar, S. P. Bera, N. Ganguli and S. Konar, *Inorg. Chem.*, 2017, **56**, 4956–4965.
- 82 B. Q. Song, D. Q. Chen, Z. G. Ji, J. H. Tang, X. L. Wang, H. Y. Zang and Z. M. Su, *Chem. Commun.*, 2017, **53**, 1892–1895.
- 83 X. Q. Liang, K. Cai, F. Zhang, J. Liu and G. S. Zhu, *J. Mater. Chem. A*, 2017, **5**, 25350–25358.
- 84 W. H. Xing, H. Y. Li, X. Y. Dong and S. Q. Zang, *J. Mater. Chem. A*, 2018, **6**, 7724–7730.
- 85 D. W. Lim, M. Sadakiyo and H. Kitagawa, *Chem. Sci.*, 2019, **10**, 16–33.
- 86 X. Wang, T. Qin, S. S. Bao, Y. C. Zhang, X. Shen, L. M. Zheng and D. R. Zhu, *J. Mater. Chem. A*, 2016, **4**, 16484–16489.
- 87 J. Du, X. Y. Sun, Y. C. He, Y. Yu, X. F. Zheng, L. J. Tian and Z. Liu, *Appl. Organomet. Chem.*, 2018, **32**, e4517.
- 88 J. Y. Shi, J. Li, H. M. Zeng, G. H. Zou, Q. H. Zhang and Z. Lin, *Dalton Trans.*, 2018, **47**, 15288–15292.
- 89 S. P. Bera, A. Mondal, S. Roy, B. Dey, A. Santra and S. Konar, *Dalton Trans.*, 2018, **47**, 15405–15415.
- 90 Y. Y. Yuan, S. L. Yang, C. X. Zhang and Q. L. Wang, *CrystEngComm*, 2018, **20**, 6989–6994.
- 91 A. Alowasheer, S. Tominaka, Y. Ide, Y. Yamauchi and Y. Matsushita, *CrystEngComm*, 2018, **20**, 6713–6720.
- 92 Q. Tang, Y. L. Yang, N. Zhang, Z. Liu, S. H. Zhang, F. S. Tang, J. Y. Hu, Y. Z. Zheng and F. P. Liang, *Inorg. Chem.*, 2018, **57**, 9020–9027.
- 93 H. Yang, X. Y. Duan, J. J. Lai and M. L. Wei, *Inorg. Chem.*, 2019, **58**, 1020–1029.
- 94 H. Yang, X. Y. Duan, J. J. Lai, Y. Zhao, X. J. Wang and M. L. Wei, *Inorg. Chem.*, 2019, **58**, 446–455.
- 95 S. K. Konavarapu, A. Goswami, A. G. Kumar, S. Banerjee and K. Biradha, *Inorg. Chem. Front.*, 2019, **6**, 184–191.
- 96 C. F. Liu, N. Zhao, X. Q. Zou and G. S. Zhu, *CrystEngComm*, 2018, **20**, 3158–3161.
- 97 S. L. Yang, P. P. Sun, Y. Y. Yuan, C. X. Zhang and Q. L. Wang, *CrystEngComm*, 2018, **20**, 3066–3073.
- 98 J. P. Cao, F. C. Shen, X. M. Luo, C. H. Cui, Y. Q. Lan and Y. Xu, *RSC Adv.*, 2018, **8**, 18560–18566.
- 99 L. Z. Liu, Z. Z. Yao, Y. X. Ye, Q. J. Lin, S. M. Chen, Z. J. Zhang and S. C. Xiang, *Cryst. Growth Des.*, 2018, **18**, 3724–3728.
- 100 Y. H. Luo, L. Q. Yi, J. N. Lu, L. Z. Dong and Y. Q. Lan, *CrystEngComm*, 2018, **20**, 6077–6081.
- 101 L. Xu, Z. F. Wang, Y. Lu, T. T. Yan, H. R. Tian, X. H. Li, S. Wang, X. W. Sun, Z. Zhang and T. Y. Dang, *New J. Chem.*, 2018, **42**, 16516–16522.
- 102 P. Mondal, B. Dey, S. Roy, S. P. Bera, R. Nasani, A. Santra and S. Konar, *Cryst. Growth Des.*, 2018, **18**, 6211–6220.

- 103 H. L. Xu, L. Feng, W. T. Huang, Q. Y. Wang and H. Zhou, *New J. Chem.*, 2019, **43**, 807–812.
- 104 S. L. Yang, Y. Y. Yuan, F. Ren, C. X. Zhang and Q. L. Wang, *Dalton Trans.*, 2019, **48**, 2190–2196.
- 105 C. Montoro, D. Rodriguez-San-Miguel, E. Polo, R. Escudero-Cid, M. L. Ruiz-Gonzalez, J. A. R. Navarro, P. Ocon and F. Zamora, *J. Am. Chem. Soc.*, 2017, **139**, 10079–10086.
- 106 M. Vitadello, S. Suarez, S. H. Chung, K. Fujimoto, V. D. Noto, S. G. Greenbaum and T. Furukawa, *Electrochim. Acta*, 2003, **48**, 2227–2237.
- 107 J. Y. Xi, Y. X. Bai, X. P. Qiu, W. T. Zhu, L. Q. Chen and X. Z. Tang, *New J. Chem.*, 2005, **29**, 1454–1460.
- 108 B. M. Wiers, M. L. Foo, N. P. Balsara and J. R. Long, *J. Am. Chem. Soc.*, 2011, **133**, 14522–14525.
- 109 R. Ameloot, M. Aubrey, B. M. Wiers, A. P. Gómora-Figueroa, S. N. Patel, N. P. Balsara and J. R. Long, *Chem.–Eur. J.*, 2013, **19**, 5533–5536.
- 110 K. Fujie, R. Ikeda, K. Otsubo, T. Yamada and H. Kitagawa, *Chem. Mater.*, 2015, **27**, 7355–7361.
- 111 Z. Q. Wang, Z. J. Wang, L. Y. Yang, H. B. Wang, Y. L. Song, L. Han, K. Yang, J. T. Hu, H. B. Chen and F. Pan, *Nano Energy*, 2018, **49**, 580–587.
- 112 L. Shen, H. B. Wu, F. Liu, J. L. Brosmer, G. R. Shen, X. F. Wang, J. I. Zink, Q. F. Xiao, M. Cai, G. Wang, Y. F. Lu and B. Dunn, *Adv. Mater.*, 2018, **30**, 1707476.
- 113 J. Cepeda, S. Pérez-Yáñez, G. Beobide, O. Castillo, E. Goikolea, F. Aguesse, L. Garrido, A. Luque and P. A. Wright, *Chem. Mater.*, 2016, **28**, 2519–2528.
- 114 S. B. Kim, J. Y. Kim, N. C. Jeong and K. M. Ok, *Inorg. Chem. Front.*, 2017, **4**, 79–83.
- 115 A. P. Côté, A. I. Benin, N. W. Ockwig, A. J. Matzger, M. O'Keeffe and O. M. Yaghi, *Science*, 2005, **310**, 1166–1170.
- 116 S. Kandambeth, A. Mallick, B. Lukose, M. V. Mane, T. Heine and R. Banerjee, *J. Am. Chem. Soc.*, 2012, **134**, 19524–19527.
- 117 P. Kuhn, M. Antonietti and A. Thomas, *Angew. Chem., Int. Ed.*, 2008, **47**, 3450–3453.
- 118 J. W. Colson, J. A. Mann, C. R. DeBlase and W. R. Dichtel, *J. Polym. Sci., Part A: Polym. Chem.*, 2015, **53**, 378–384.
- 119 D. A. Vazquez-Molina, G. S. Mohammad-Pour, C. Lee, M. W. Logan, X. F. Duan, J. K. Harper and F. J. Uribe-Romo, *J. Am. Chem. Soc.*, 2016, **138**, 9767–9770.
- 120 H. W. Chen, H. Y. Tu, C. J. Hu, Y. Liu, D. Dong, Y. F. Sun, Y. F. Dai, S. L. Wang, H. Qian, Z. Y. Lin and L. W. Chen, *J. Am. Chem. Soc.*, 2018, **140**, 896–899.
- 121 Q. Xu, S. S. Tao, Q. H. Jiang and D. L. Jiang, *J. Am. Chem. Soc.*, 2018, **140**, 7429–7432.
- 122 A. Omote, S. Yotsuhashi, Y. Zenitani and Y. Yamada, *J. Am. Chem. Soc.*, 2011, **94**, 2285–2288.
- 123 J. C. McKeen and M. E. Davis, *J. Phys. Chem. C*, 2009, **113**, 9870–9877.
- 124 N. Yoshimoto, Y. Tomonaga, M. Ishikawa and M. Morita, *Electrochim. Acta*, 2001, **46**, 1195–1200.
- 125 S. Higashi, K. Miwa, M. Aoki and K. Takechi, *Chem. Commun.*, 2014, **50**, 1320–1322.
- 126 M. L. Aubrey, R. Ameloot, B. M. Wiers and J. R. Long, *Energy Environ. Sci.*, 2014, **7**, 667–671.
- 127 S. S. Park, Y. Tulchinsky and M. Dincă, *J. Am. Chem. Soc.*, 2017, **139**, 13260–13263.
- 128 E. M. Miner, S. S. Park and M. Dincă, *J. Am. Chem. Soc.*, 2019, **141**, 4422–4427.
- 129 F. P. Kinik, A. Uzun and S. Keskin, *ChemSusChem*, 2017, **10**, 2842–2863.
- 130 W. X. Chen, H. R. Xu, G. L. Zhuang, L. S. Long, R. B. Huang and L. S. Zheng, *Chem. Commun.*, 2011, **47**, 11933–11935.
- 131 K. Fujie, T. Yamada, R. Ikeda and H. Kitagawa, *Angew. Chem., Int. Ed.*, 2014, **53**, 11302–11305.
- 132 K. Fujie, K. Otsubo, R. Ikeda, T. Yamada and H. Kitagawa, *Chem. Sci.*, 2015, **6**, 4306–4310.
- 133 W. Chen, N. Ogiwara, K. Kadota, K. Panyarat, S. Kitagawa and S. Horike, *Dalton Trans.*, 2017, **46**, 10798–10801.
- 134 G. Givaja, O. Castillo, E. Mateo, A. Gallego, C. J. Gómez-García, A. Calzolari, R. Felice and F. Zamora, *Chem.–Eur. J.*, 2012, **18**, 15476–15484.
- 135 J. Conesa-Egea, C. D. Redondo, J. I. Martínez, C. J. Gómez-García, Ó. Castillo, F. Zamora and P. Amo-Ochoa, *Inorg. Chem.*, 2018, **57**, 7568–7577.
- 136 B. Dhara, V. Kumar, K. Gupta, P. K. Jha and N. Ballav, *ACS Omega*, 2017, **2**, 4488–4493.
- 137 L. Sun, C. H. Hendon, S. S. Park, Y. Tulchinsky, R. Wan, F. Wang, A. Walsh and M. Dincă, *Chem. Sci.*, 2017, **8**, 4450–4457.
- 138 L. S. Xie, L. Sun, R. Wan, S. S. Park, J. A. DeGayner, C. H. Hendon and M. Dincă, *J. Am. Chem. Soc.*, 2018, **140**, 7411–7417.
- 139 L. Sun, C. H. Hendon and M. Dincă, *Dalton Trans.*, 2018, **47**, 11739–11743.
- 140 J. G. Park, M. L. Aubrey, J. Oktawiec, K. Chakarawet, L. E. Darago, F. Grandjean, G. J. Long and J. R. Long, *J. Am. Chem. Soc.*, 2018, **140**, 8526–8534.
- 141 X. Huang, P. Sheng, Z. Y. Tu, F. J. Zhang, J. H. Wang, H. Geng, Y. Zou, C. A. Di, Y. P. Yi and Y. M. Sun, *Nat. Commun.*, 2015, **6**, 7408.
- 142 X. Huang, H. S. Li, Z. Y. Tu, L. Y. Liu, X. Y. Wu, J. Chen, Y. Y. Liang, Y. Zou, Y. P. Yi, J. L. Sun, W. Xu and D. B. Zhu, *J. Am. Chem. Soc.*, 2018, **140**, 15153–15156.
- 143 M. G. Campbell, D. Sheberla, S. F. Liu, T. M. Swager and M. Dincă, *Angew. Chem., Int. Ed.*, 2015, **54**, 4349–4352.
- 144 H. Nagatomi, N. Yanai, T. Yamada, K. Shiraishi and N. Kimizuka, *Chem.–Eur. J.*, 2018, **24**, 1806–1810.
- 145 L. Sun, S. S. Park, D. Sheberla and M. Dincă, *J. Am. Chem. Soc.*, 2016, **138**, 14772–14782.
- 146 S. S. Park, E. R. Hontz, L. Sun, C. H. Hendon, A. Walsh, T. V. Voorhis and M. Dincă, *J. Am. Chem. Soc.*, 2015, **137**, 1774–1777.
- 147 C. Hermosa, J. V. Álvarez, M. R. Azani, C. J. Gómez-García, M. Fritz, J. M. Soler, J. Gómez-Herrero, C. Gómez-Navarro and F. Zamora, *Nat. Commun.*, 2013, **4**, 1709.
- 148 P. Amo-Ochoa, J. M. Soler, J. J. Palacios, J. Gómez-Herrero and F. Zamora, *Adv. Mater.*, 2018, **30**, 1705645.
- 149 B. Dutta, A. Dey, C. Sinha, P. P. Ray and M. Hedayetullah, *Inorg. Chem.*, 2018, **57**, 8029–8032.
- 150 C. Musumeci, S. Osella, L. Ferlauto, D. Niedzialek, L. Grisanti, S. Bonacchi, A. Jouaiti, S. Milita, A. Ciesielski,

- D. Beljonne, W. Hosseini and P. Samorì, *Nanoscale*, 2016, **8**, 2386–2394.
- 151 N. Ogihara, N. Ohba and Y. Kishida, *Sci. Adv.*, 2017, **3**, 1603103.
- 152 D. Sheberla, L. Sun, M. A. Blood-Forsythe, S. Er, C. R. Wade, C. K. Brozek, A. Aspuru-Guzik and M. Dincă, *J. Am. Chem. Soc.*, 2014, **136**, 8859–8862.
- 153 A. J. Clough, J. M. Skelton, C. A. Downes, A. A. Rosa, J. W. Yoo, A. Walsh, B. C. Melot and S. C. Marinescu, *J. Am. Chem. Soc.*, 2017, **139**, 10863–10867.
- 154 M. G. Campbell, S. F. Liu, T. M. Swager and M. Dincă, *J. Am. Chem. Soc.*, 2015, **137**, 13780–13783.
- 155 M. K. Smith, K. E. Jensen, P. A. Pivak and K. A. Mirica, *Chem. Mater.*, 2016, **28**, 5264–5268.
- 156 M. K. Smith and K. A. Mirica, *J. Am. Chem. Soc.*, 2017, **139**, 16759–16767.
- 157 L. E. Darago, M. L. Aubrey, C. J. Yu, M. I. Gonzalez and J. R. Long, *J. Am. Chem. Soc.*, 2015, **137**, 15703–15711.
- 158 M. E. Ziebel, L. E. Darago and J. R. Long, *J. Am. Chem. Soc.*, 2018, **140**, 3040–3051.
- 159 L. Sun, C. H. Hendon, M. A. Minier, A. Walsh and M. Dincă, *J. Am. Chem. Soc.*, 2015, **137**, 6164–6167.
- 160 D. Vallejo-Sánchez, P. Amo-Ochoa, G. Beobide, O. Castillo, M. Fröba, F. Hoffmann, A. Luque, P. Ocón and S. Pérez-Yáñez, *Adv. Funct. Mater.*, 2017, **27**, 1605448.
- 161 B. Dhara, S. S. Nagarkar, J. Kumar, V. Kumar, P. K. Jha, S. K. Ghosh, S. Nair and N. Ballav, *J. Phys. Chem. Lett.*, 2016, **7**, 2945–2950.
- 162 A. Sengupta, S. Datta, C. Su, T. S. Herng, J. Ding, J. J. Vittal and K. P. Loh, *ACS Appl. Mater. Interfaces*, 2016, **8**, 16154–16159.
- 163 K. Thurmer, C. Schneider, V. Stavila, W. Friddle, F. Leonard, R. A. Fischer, M. D. Allendorf and A. A. Talin, *ACS Appl. Mater. Interfaces*, 2018, **10**, 39400–39410.
- 164 G. P. Li, K. Zhang, H. Y. Zhao, L. Hou and Y. Y. Wang, *ChemPlusChem*, 2017, **82**, 716–720.
- 165 J. X. Lin, J. Liang, J. F. Feng, B. Karadeniz, J. Lu and R. Cao, *Inorg. Chem. Front.*, 2016, **3**, 1393–1397.
- 166 T. C. Wang, I. Hod, C. O. Audu, N. A. Vermeulen, S. T. Nguyen, O. K. Farha and J. T. Hupp, *ACS Appl. Mater. Interfaces*, 2017, **9**, 12584–12591.
- 167 S. Goswami, D. Ray, K. Otake, C. W. Kung, S. J. Garibay, T. Islamoglu, A. Atilgan, Y. X. Cui, C. J. Cramer, O. K. Farha and J. T. Hupp, *Chem. Sci.*, 2018, **9**, 4477–4482.
- 168 B. L. Ouay, M. Boudot, T. Kitao, T. Yanagida, S. Kitagawa and T. Uemura, *J. Am. Chem. Soc.*, 2016, **138**, 10088–10091.
- 169 B. Dutta, A. Dey, K. Naskar, S. Maity, F. Ahmed, S. Islam, C. Sinha, P. Ghosh, P. P. Ray and M. H. Mir, *New J. Chem.*, 2018, **42**, 10309–10316.
- 170 F. Ahmed, J. Datta, B. Dutta, K. Naskar, C. Sinha, S. M. Alam, S. Kundu, P. P. Ray and M. H. Mir, *RSC Adv.*, 2017, **7**, 10369–10375.
- 171 K. Otsubo, T. Suto, A. Kobayashi, R. Ikeda, M. Hedo, Y. Uwatoko and H. Kitagawa, *Eur. J. Inorg. Chem.*, 2016, **27**, 4402–4407.
- 172 B. Bhattacharya, D. K. Maity, A. Layek, S. Jahiruddin, A. Halder, A. Dey, S. Ghosh, C. Chowdhury, A. Datta and P. P. Ray, *CrystEngComm*, 2016, **18**, 5754–5763.
- 173 S. A. Sahadevan, A. Abherve, N. Monni, C. S. Pipaon, J. R. Galan-Mascaros, J. C. Waerenborgh, B. J. C. Vieira, P. Auban-Senzier, S. Pillet, E. E. Bendeif, P. Alemany, E. Canadell, M. L. Mercuri and N. Avarvari, *J. Am. Chem. Soc.*, 2018, **140**, 2611–12621.
- 174 K. Hassanein, J. Conesa-Egea, S. Delgado, O. Castillo, S. Benmansour, J. I. Martinez, G. Abellan, C. J. Gomez-Garcia, F. Zamora and P. Arno-Ochoa, *Chem.-Eur. J.*, 2015, **21**, 17282–17292.